Dissertation zur Erlangung des Doktorgrades
der Fakultät für Chemie und Pharmazie
der Ludwig-Maximilians-Universität München

The kinase-coupled TRPM7 channel is the central gatekeeper of intestinal mineral absorption

Lorenz Mittermeier

aus

München, Deutschland

2019

Erklärung

Diese Dissertation wurde im Sinne von § 7 der Promotionsordnung vom 28. November 2011 von Herrn Prof. Dr. Thomas Gudermann betreut und von Herrn PD Dr. Dietmar Martin von der Fakultät für Chemie und Pharmazie vertreten.

Eidesstattliche Versicherung

Diese Dissertation wurde eigenständig und ohne unerlaubte Hilfe erarbeitet.

München, den 08.03.2019

.....

Lorenz Mittermeier

Dissertation eingereicht am 14.03.2019

1. Gutachter: Herr PD Dr. Dietmar Martin

2. Gutachter: Herr Prof. Dr. Thomas Gudermann

Mündliche Prüfung am 03.05.2019

1 Summary

Zn^{2+}, Mg^{2+} and Ca^{2+} are essential divalent cations, which are required for many signaling pathways and metabolic processes. Previously, different types of ion channels and transporters have been proposed as regulators of cytoplasmic concentrations of these cations in a cell-specific mode. However, it remains unclear how these proteins orchestrate the organismal balance of divalent cations. Here, we present evidence that the kinase-coupled TRPM7 channel plays a vital role in the organismal balance of Zn^{2+}, Mg^{2+} and Ca^{2+}. To understand the physiological role of TRPM7, we first examined TRPM7-deficient cells and found that the lack of TRPM7 results in a reduced cellular uptake of Zn^{2+} and Mg^{2+}. To elucidate the *in vivo* relevance of these findings, we studied several mouse lines carrying mutations in the *Trpm7* gene. Intestinal-specific inactivation of *Trpm7* triggered profound organismal deficiencies of Zn^{2+}, Mg^{2+} and Ca^{2+}, early postnatal growth delay and death. In contrast, the kidney-restricted inactivation of *Trpm7* caused no effect on the mineral homeostasis and physical appearance of mutant mice. Furthermore, global inactivation of TRPM7 kinase did not affect the organismal balance of divalent cations, highlighting the importance of the channel segment rather than the kinase domain of TRPM7 in mineral homeostasis. Importantly, dietary supplementation by Zn^{2+} and Mg^{2+} extended the survival rate of animals lacking intestinal TRPM7. Taken together, our results suggest that the intestinal TRPM7 channel functions as a central common gatekeeper of nutritional intake of divalent cations.

Table of contents

2 Introduction

2.1 The transient receptor potential (TRP) gene family

Transient receptor potential (TRP) proteins belong to a large gene family of cation channels. TRP channels were discovered during a search for new fruit fly *Drosophila melanogaster* strains with impaired vision. Photoreceptor cells of one mutant strain showed only a transient receptor potential triggered by light illumination [1]. Accordingly, the affected gene was identified and entitled as *transient receptor potential* channel [2].

Follow-up studies discovered 28 TRP proteins in mammals, which can be subdivided into six sub-families based on a primary amino acid sequence homology (Figure 1): TRPA (ankyrin repeats containing TRP channels), TRPC (canonical channels), TRPM (melastatin-related TRP channels), TRPML (mucolipin channels), TRPV (vanilloid receptor related channels) and TRPP (polycystin channels) [3].

With a few exceptions, the channel moiety of TRP proteins consists of 6 transmembrane helices and intracellular C- and N-termini. TRP channels form homo- and heterotetramers [4]. The majority of TRP channels are plasma membrane cation channels involved in a plethora of physiological processes such as temperature sensation, taste- or mechanotransduction and homeostatic control of cellular content of divalent cations [4]. Many TRP channels are ubiquitously expressed, while others display tissue-specific expression patterns [4, 5].

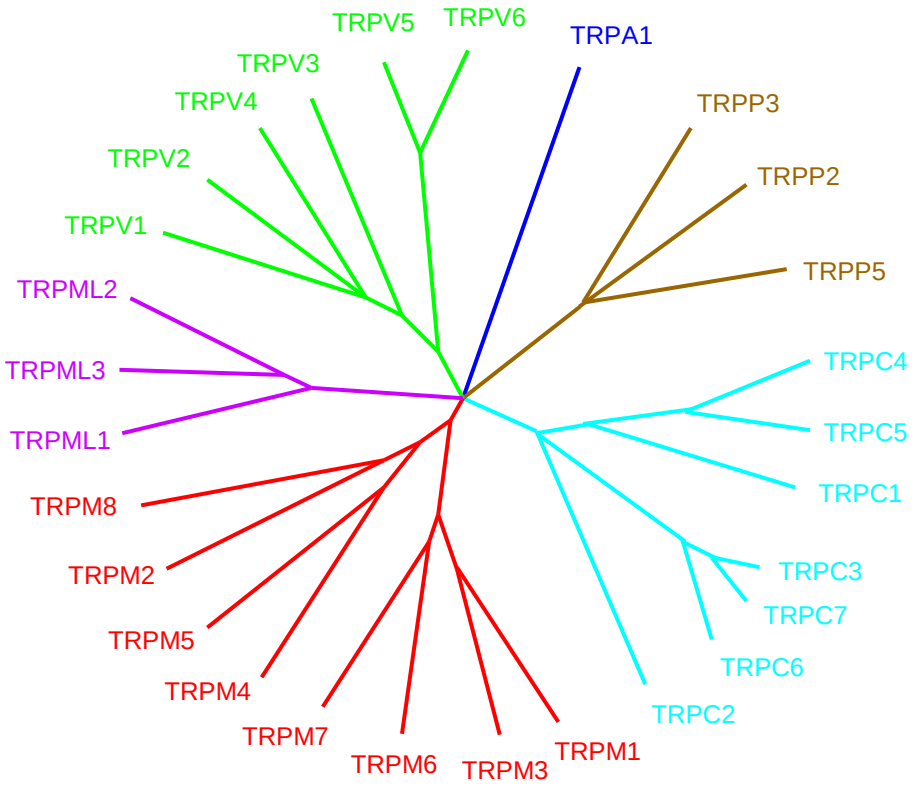

Figure 1: Phylogenetic tree of the mammalian TRP gene family (modified from Nilius et al., 2011 [4]).

2.2 The transient receptor potential cation channel, subfamily M, member 7 (TRPM7)

2.2.1 Structural organization and functional characteristics of TRPM7

TRPM7 and its closest homologue, TRPM6, are unique TRP channels since these proteins contain an ion channel covalently linked to a kinase domain [6-12]. TRPM7 functions as plasma membrane ion channel selective for divalent cations [6, 13, 14]. It regulates many cellular processes including Ca^{2+} and Mg^{2+} homeostasis, cell viability, cell proliferation, cell migration and exocytosis [6, 15-20]. TRPM7 is an ubiquitously expressed protein [6, 14, 21, 22] and functions as a plasma membrane tetrameric channel, i.e. four TRPM7 subunits build a common channel pore [23] similar to other TRP channels [24-27]. The channel domain of TRPM7 contains 6 transmembrane helices (Figure 2) [5].

The long N-terminus of TRPM7 is highly conserved among TRPM channels and displays no apparent homology to other proteins. The C-terminal segment of TRPM7 contains a transient receptor potential (TRP) domain, a coiled-coil (CC) domain and an α-kinase substrate domain (SD) linked to an α-kinase domain (KD) (Figure 2). The pore-forming region is located between the 5^{th} and the 6^{th} helix [6, 14] (Figure 2).

In some studies, it was suggested that the TRP domain plays a key role in gating of the channel [23, 28, 29] and that the CC domain regulates the tetrameric assembly of the TRPM7 channel [30]. However, a recent study with recombinant zebrafish TRPM7 (zTRPM7) showed that a truncation mutation prior to the CC domain did not impair a formation of the functional zTRPM7 channel [31], suggesting that the CC domain might not be crucial for the tetramerization of the TRPM7 channel. Other studies suggested that the N-terminus of TRPM7 may be involved in tetrameric assembly of the channel [10]. The SD domain of TRPM7 contains multiple autophosphorylation serine and threonine residues [32-34]. SD is located upstream of the kinase domain. Recently, a cryo-electron microscopy (cryo-EM) structure of TRPM7 was published [23]. The resolved structure confirmed the tetrameric assembly of TRPM7 and allowed to elucidate mechanisms of divalent cation selectivity of the TRPM7 channel. It was proposed that backbone carbonyls of Phe1045, Gly1046 and Glu1047 form a cation selectivity filter by replacing the water molecules of the second hydration shell of Mg^{2+} entering the channel pore.

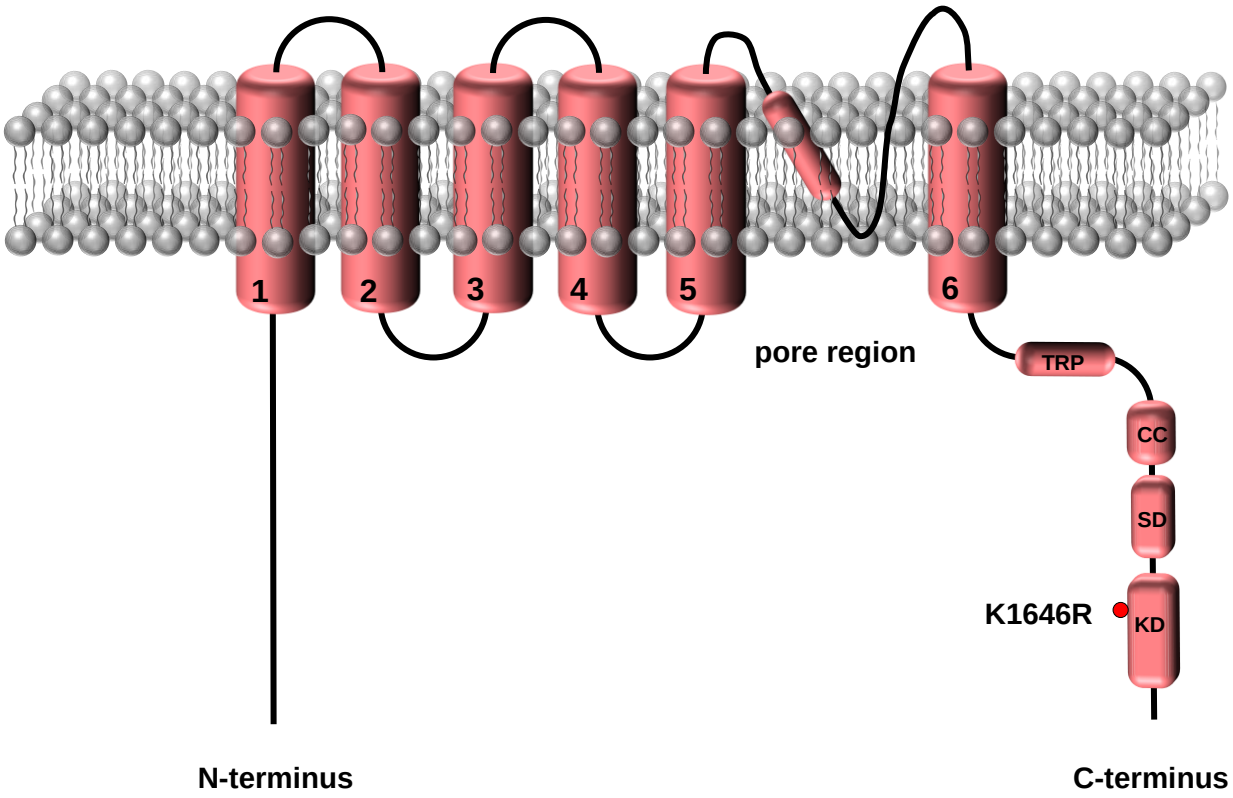

Figure 2: Topology of domains in the TRPM7 channel subunit. TRPM7 contains six transmembrane helices (1-6) and large cytosolic N- and C-termini. The C-terminus contains a highly conserved transient receptor potential (TRP) domain, a coiled-coil (CC) domain, a kinase substrate domain (SD) and a kinase domain (KD). The red dot indicates the location of the "kinase-dead" mutation K1646R.

Patch-clamp experiments showed that the TRPM7 channel is selective for divalent cations [6, 13] displaying the permeability sequence $Zn^{2+} \approx Ni^{2+} >> Ba^{2+} > Co^{2+} > Mg^{2+} \geq Mn^{2+} \geq Sr^{2+} \geq Cd^{2+} \geq Ca^{2+}$. However, TRPM7 is impermeable for trivalent ions like La^{3+} or Gd^{3+} [13]. TRPM7 is able to conduct monovalent cations if cells are exposed to a divalent cation-free external solution. In addition, acidic extracellular pH reduces TRPM7's pore permeability for Mg^{2+} and Ca^{2+} [35]. Intracellular Mg^{2+} and Mg·ATP are negative modulators of the TRPM7 channel. Consequently, it was suggested that metabolic processes linked to cytosolic levels of Mg^{2+} or Mg·ATP can regulate TRPM7 currents [6, 36, 37]. Moreover, opening of the TRPM7 channel is controlled by the plasma membrane phospholipid phosphatidylinositol 4,5-bisphosphate (PIP2) [38].

The kinase domain of TRPM7 belongs to a family of atypical α-kinases named after their ability to phosphorylate serine and threonine residues located in α-helixes. Six mammalian α-kinases are known [39] including TRPM6 and TRPM7. Catalytic domains of α-kinases have no significant amino-acid sequence homology to conventional protein kinases [40]. However, a catalytic segment of TRPM7 kinase displays 3D similarity to that in conventional protein kinases [23, 41].

2.2.2 A role of TRPM7 uncovered in cultured cells

Several independent groups proposed that TRPM7 is crucial for maintaining cellular Mg^{2+} levels (Figure 3). Mg^{2+} is the most abundant divalent cation in the cell. Total cellular levels of Mg^{2+} were found in the range of 10-30 mM. However, free Mg^{2+} was estimated in the range of 0.5-1.2 mM since most of Mg^{2+} is bound to ATP, polynucleotides or ribosomes [42]. Mg^{2+} is crucial for many cellular processes. Thus, Mg^{2+} is a co-factor of ~600 enzyme reactions and is essential for folding of DNA, mRNA, tRNA and many proteins [42]. Consequently, Mg^{2+} deficiency results in growth arrest of cells [42].

Cell lines with loss-of-function mutations in TRPM7 (TRPM7 KO) were extensively studied including chicken B lymphoma DT-40 cells [17], mouse embryonic stem cells [43], trophoblast stem cells [6, 44] and human haploid leukemia (HAP1) cells [44]. All these cell lines displayed a growth arrest when cultured in a regular cell culture medium [44]. However, addition of Mg^{2+} (10 mM $MgCl_2$) to the medium normalized proliferation of TRPM7-deficient cells arguing that TRPM7 is required for maintaining cellular Mg^{2+} levels [17, 43, 44].

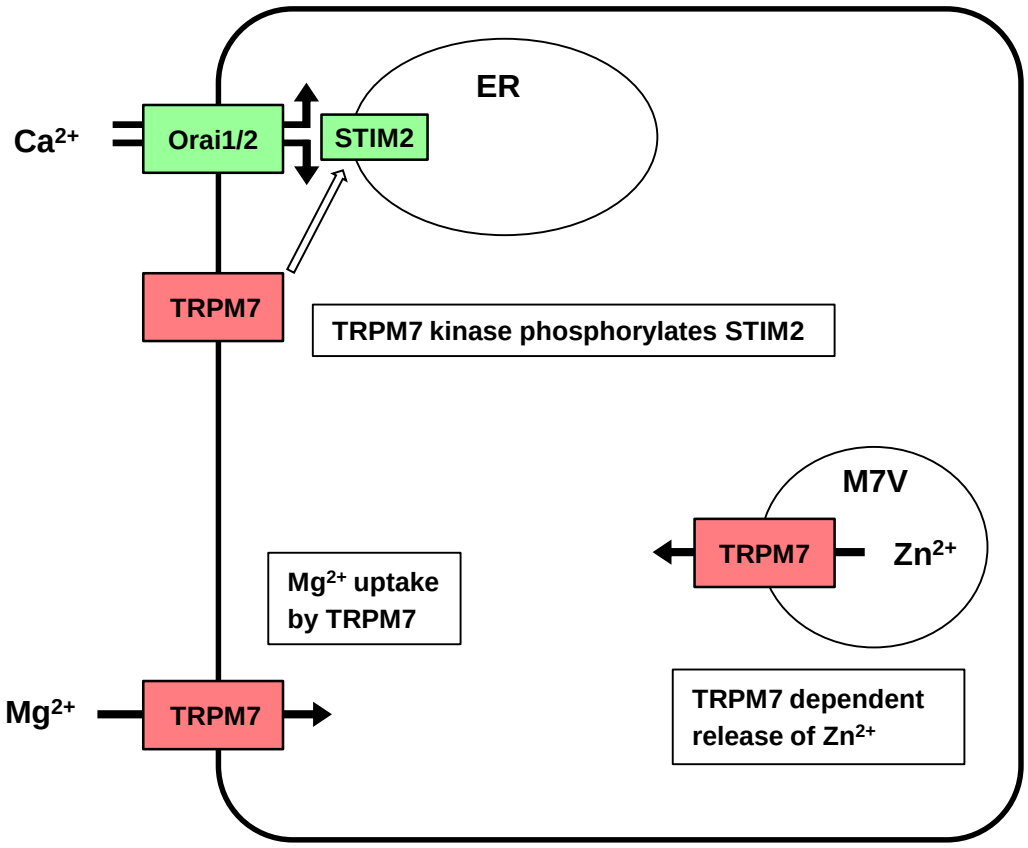

Figure 3: The suggested role of TRPM7 in regulation of cellular levels of Mg^{2+}, Ca^{2+} and Zn^{2+}. Cellular Mg^{2+} uptake is directly mediated by the TRPM7 channel. TRPM7 kinase regulates cytoplasmic Ca^{2+} levels indirectly due to phosphorylation of stromal interaction molecule (STIM2) located in the endoplasmic reticulum (ER) resulting in interaction of STIM2 with Orai1/2 channels followed by store-operated Ca^{2+} entry (SOCE). Intracellularly located TRPM7 modulates release of Zn^{2+} from glutathione-enriched vesicles (entitled as M7V).

Many investigators proposed that TRPM7 functions as a Ca^{2+} permeable channel involved in Ca^{2+}-signaling [6, 13, 14]. In addition, it was found that TRPM7 modulates store-operated Ca^{2+} entry (SOCE) by interaction with the endoplasmic reticulum (ER) Ca^{2+} sensor stromal interaction molecule 2 (STIM2) (Figure 3). In turn, STIM2 activates the plasma calcium release-activated calcium channel protein 1/2 (Orai1/2) [45, 46]. Moreover, TRPM7 was linked to cytoplasmic Ca^{2+} oscillations in eggs during the fertilization-induced early embryonic development [19, 20]. Finally, TRPM7 was linked to Ca^{2+} flicker activity in human embryonic lung fibroblasts [47]. It was proposed that TRPM7 can influence Ca^{2+} flickering due to its interaction with phospholipase C [38].

More recently, it was shown that TRPM7 can also regulate cellular Zn^{2+} levels. The group of David Clapham presented evidence that TRPM7 is localized in a new type of acidic glutathione (GSH)-enriched vesicles (referred to M7V). M7V contains high Zn^{2+} levels and may function as intracellular Zn^{2+} stores. It was suggested that TRPM7 regulates a release of Zn^{2+} from these organelles to control cytosolic Zn^{2+} concentrations (Figure 3) [48]. The same study suggested that TRPM7 activity is linked to reactive oxygen species (ROS). Specifically, ROS can trigger the TRPM7-dependent release of Zn^{2+} from M7V vesicles, whereas GSH blocks TRPM7-dependent cytosolic Zn^{2+} uptake in M7V vesicles. The authors concluded that TRPM7 can function as a sensor of oxidative stress and controls ROS-dependent release of Zn^{2+} from M7V vesicles [48]. In another study, it was reported that TRPM7 can regulate cytosolic Zn^{2+} concentrations in murine embryonic stem cells [49]. In addition, it was shown that stress hormones increase neurotoxicity of Zn^{2+} due to increased uptake of Zn^{2+} via TRPM7 in neuroblastoma SH-SY5Y cells [50].

TRPM7 kinase phosphorylates Ser and Thr residues in a Mg^{2+}-dependent mode [51]. Several substrates of TRPM7 kinase have been identified. Annexin1 is phosphorylated by TRPM7 [52]. Annexin1 regulates membrane fusion and its TRPM7-dependent modification may play a role in cell growth and apoptosis [52, 53]. Moreover, TRPM7 kinase was linked to cell motility and adhesion because of its ability to phosphorylate myosin IIA, IIB and IIC [54-56]. The group of David Clapham reported that the kinase domain of TRPM7 can be cleaved from the channel subunit and that the cleaved product can translocate to the cell nucleus where it interacts and phosphorylates the chromatin-remodeling proteins such as histone H3 [49]. Moreover, it was shown that TRPM7 can phosphorylate PLCγ2 and, consequently, modulate PLCγ2 signaling [57]. It was suggested that TRPM7 kinase is able to phosphorylate eukaryotic elongation factor 2 kinase (eEF2K) leading to changes in protein translation rate in cells challenged by Mg^{2+} starvation [58]. In addition, there are several TRPM7 autophosphorylation residues, which may modulate channel activity and trafficking of TRPM7 [34]. The functional relationship of the kinase and channel moieties of TRPM7 was extensively studied but it remains not well understood. To elucidate such interaction, different point mutations were introduced in TRPM7 diminishing its kinase activity referred to as ‘kinase-dead’ TRPM7 variants. The ‘kinase-dead’ mutation K148R was found to be able to negatively regulate TRPM7 currents [14, 17]. In contrary, other studies showed that activity of TRPM7 kinase did not modify the channel features of TRPM7 including its sensitivity to intracellular Mg^{2+} [33].

2.2.3 Assessment of TRPM7 in genetic animal models

To elucidate the *in vivo* role of TRPM7, several animal genetic models have been produced by independent groups. Thus, Jin et al. generated a mouse strain with a global deletion of TRPM7 [59]. First, a mouse line with two loxP sites flanking exon 17 of TRPM7 was produced. Next, these mice were crossed with transgenic mice ubiquitously expressing Cre recombinase from *Sox2-Cre* transgene. This cross resulted in a global null mutation in *Trpm7 (Trpm7* $^{null/null}$*)* because the deletion of exon 17 introduces a frame-shift mutation in the open reading frame (ORF) of *Trpm7*. *Trpm7* $^{null/null}$ individuals were not able to survive after embryonic day 6.5 (e6.5) [59] indicating that TRPM7 is essential for the early embryonal development (Table 1). The underlying mechanisms of this phenotype remain unknown.

In another study, Ryazanova et al. replaced exons 32-36 of *Trpm7* with a neomycin resistance sequence resulting in a truncation of TRPM7 upstream of the α-kinase domain [43]. Mice homozygous for *Trpm7* $^{\Delta kinase}$ *(Trpm7* $^{\Delta kinase/\Delta kinase}$*)* showed early embryonic lethality at e8.5 (Table 1) (similar to the phenotype of *Trpm7* $^{null/null}$ mice [59]) suggesting that *Trpm7* $^{\Delta kinase}$ is also a null mutation. In contrast to the *Trpm7* $^{\Delta kinase/\Delta kinase}$ animals, heterozygous mice *(Trpm7* $^{\Delta kinase/wt}$*)* were viable (Table 1). *Trpm7* $^{\Delta kinase/wt}$ mice developed no signs of Mg^{2+} deficiency if maintained on a regular diet containing 0.1% Mg^{2+}. However, mutant mice fed by a low Mg^{2+} diet (0.003%) displayed reduced Mg^{2+} levels in serum and bones, and increased mortality compared to wildtype mice placed on the same Mg^{2+}-deficient diet. Consistently, Mg^{2+} content in feces of *Trpm7* $^{\Delta kinase/wt}$ was increased. The authors suggested that *Trpm7* $^{\Delta kinase/wt}$ mice develop a defect in Mg^{2+} absorption in the intestine [43].

To define a role of TRPM7 in the morphogenesis of embryonic organs, a set of *Cre* transgenes were explored for a conditional tissue-specific inactivation of *Trpm7* (Table 1). Thus, deletion of *Trpm7* in T cell lineage led to impaired thymopoiesis [59]. Knock out of TRPM7 in the metanephric mesenchyme of the kidney resulted in abnormal kidney development [60] indicating that TRPM7 is required for nephrogenesis. Additionally, TRPM7 was found to be involved in cardiac development because a heart-specific deletion of TRPM7 at e9 resulted in heart failure and death [61]. A deletion of TRPM7 in the embryonic myocardium or the sinoatrial node revealed a key role of TRPM7 in cardiac automaticity [62]. Inactivation of TRPM7 in megakaryocytes resulted in reduced Mg^{2+} in platelets, macrothrombocytopenia and thrombocytopenia [63].

While a global disruption of TRPM7 using tamoxifen-inducible Cre transgene at e7-9 caused prenatal death, a loss of TRPM7 at e14.5 or in 4-6 weeks old mice did not impact viability and physical appearance of the mutants [60]. However, it is well documented that a tamoxifen-inducible deletion of floxed alleles may be incomplete especially in differentiated cells or in tissues with a high cellular renewal rate. Hence, additional mice strains with a well-controlled tissue-specific ablation of TRPM7 may provide new information about the role of TRPM7 in the adult organism.

Table 1: Published mice strains carrying mutations in *Trpm7*

Name of strain	Effect on *Trpm7*	Phenotype
Trpm7 $^{\Delta kinase/\Delta kinase}$ [43]	Global null mutation	Mortality at e8.5
Trpm7 $^{\Delta kinase/wt}$ [43]	Heterozygote for global null mutation	Systemic Mg^{2+} deficiency induced by a low Mg^{2+} diet
Trpm7 $^{null/null}$ [59]	Global null mutation	Mortality at e6.5
Trpm7 $^{ki/ki}$ [64-66]	Global kinase-dead mutation	Normal overall appearance and behavior; slightly affected Mg^{2+} homeostasis; altered immune system homoeostasis
Trpm7 $^{fl/fl}$; Lck-Cre [59]	Deletion of TRPM7 in developing thymocytes	Impaired thymopoiesis
Trpm7 $^{fl/fl}$; Mb1-Cre [67]	Deletion of TRPM7 in B cells	Blocked development of mature peripheral B cells
Trpm7 $^{fl/fl}$; Pf4-Cre [63]	Deletion of TRPM7 in megakaryocytes	Reduced Mg^{2+} in platelets, macrothrombocytopenia, thrombocytopenia
Trpm7 $^{fl/fl}$; Pax3-Cre [60]	Deletion of TRPM7 in the metanephric mesenchyme of the embryonic kidney at e11.5	Abnormal kidney development
Trpm7 $^{fl/fl}$; TnT-Cre [61]	Deletion of TRPM7 in the heart at <e9	Heart failure and death at e11.5
Trpm7 $^{fl/fl}$; αMHC-Cre [61, 62]	Deletion of TRPM7 in the heart at e13	Impaired cardiac automaticity in adult mice
Trpm7 $^{fl/fl}$; HCN4-CreERT2 [62]	Tamoxifen-inducible deletion of TRPM7 the sinoatrial node at e9	Affected cardiac automaticity in adult mice
Trpm7 $^{fl/fl}$; Cre-ER [60]	Tamoxifen-inducible deletion at e14.5 or in 4-6 weeks old mice	No obvious effect

More recently, two groups [65, 66] generated mice with the kinase-dead K1646R point mutation in the *Trpm7* gene *(Trpm7 $^{ki/ki}$)* (Figure 2). The kinase-dead mice developed normally and showed no noticeable changes in physical appearance and behavior [65]. However, challenged *Trpm7 $^{ki/ki}$* mice developed an altered immune system homeostasis limiting the differentiation of T cells along the T_H17 functional program (Table 1) [64]. Serum Mg^{2+} and Ca^{2+} concentrations were not altered in *Trpm7 $^{ki/ki}$* mice [65]. In another study [66], an independent kinase-dead mouse line was produced using the same point mutation. These mutants were also viable and showed no pathophysiological changes. However, the authors found that bone Mg^{2+} content was ~15% reduced in 6 months old animals whereas serum Mg^{2+} concentrations were normal.

To summarize, TRPM7 plays a key role in early embryonic development and morphogenesis of internal organs of mice. Moreover, TRPM7 is likely involved in regulation of systemic homeostasis of Mg^{2+}. Mechanistically, the *in vivo* role of TRPM7 remains not fully understood.

2.2.4 A role of TRPM7 in macrothrombocytopenia

Recently, a genome sequencing of 702 patients with platelet disorders was performed [63] resulting in a discovery of patients carrying point mutations in the *TRPM7* gene. Specifically, families harboring C721G and R902C mutations in TRPM7 were identified. Both mutations are located in the channel segment of TRPM7. *In vitro* studies of recombinant C721G and R902C TRPM7 variants revealed a reduction of TRPM7 currents (85% and 39%, respectively). The affected patients were heterozygous for C721G and R902C and exhibited low platelet counts and macrothrombocytopenia associated with alterations in cytoskeletal architecture. Follow-up studies with the patients carrying a C721G mutation revealed that Mg^{2+} levels were low in the platelets. In addition, the affected subject developed atrial fibrillation. Platelets from all C721G patients displayed an increased cell size, exhibited a spherical shape and contained multiple vacuoles as well as an abnormal cytoskeletal organization. The authors suggested that abnormal Mg^{2+} balance in platelets underlies macrothrombocytopenia, similarly to Mg^{2+} deficient platelets of *Trpm7* $^{fl/fl}$*; Pf4* mice (Table 1).

2.3 A role of ion channels and transporters in organismal balance of Ca^{2+}, Mg^{2+} and Zn^{2+}

2.3.1 Maintenance of systemic Mg^{2+} homeostasis

Mg^{2+} is the most abundant divalent cation in the cell and is required for a wide range of cellular processes. Mg^{2+} is a cofactor of over 600 enzymatic reactions [42, 68-70]. Inadequate cellular Mg^{2+} uptake negatively impacts the synthesis and stability of proteins, impairs energy metabolism and, consequently, blocks cell proliferation [17, 71-73]. The major storage depots of Mg^{2+} are bones (containing 50-60% of body Mg^{2+}) and skeletal muscles (comprising 25-30% of total Mg^{2+}) [42]. The concentration of Mg^{2+} in the serum is tightly controlled in the range of 0.7-1.1 mM [74]. Hormones or metabolites, which specifically regulate systemic Mg^{2+} homeostasis, are not known.

Organismal balance of Mg^{2+} is maintained by intestinal absorption and renal excretion [75]. In the kidney, more than 95% of Mg^{2+} is reabsorbed from the primary urine [75]. In general, epithelial transport of divalent cations occurs by an active (transcellular) and a passive (paracellular) process (Figure 4). In the paracellular pathway, cations are passed through an epithelial layer via the tight junctions. The active transcellular transport consists of three steps: (1) apical uptake of cations by

channels or transporters; (2) cytosolic transport of cations by carrier proteins; (3) basolateral excretion of cations by transporters or exchangers (Figure 4).

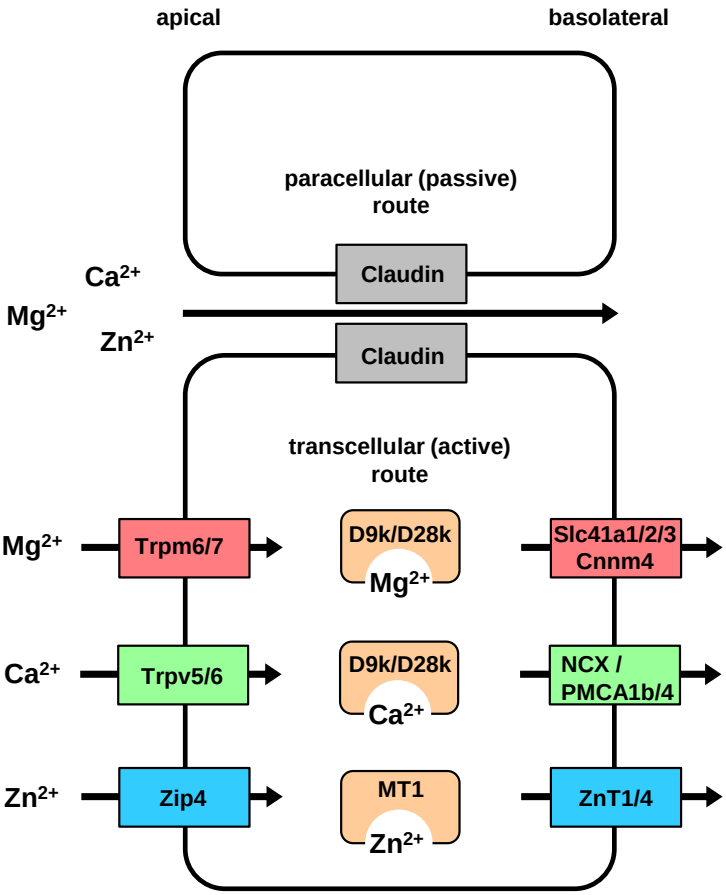

Figure 4: Key players involved in the transport of divalent cations in the kidney and the intestine. The paracellular pathway occurs via tight junctions formed by claudins (claudin-16 and 19 for Mg^{2+} and claudin-2, 12, 14, 15, 16 and 19 for Ca^{2+}). The transcellular pathway is driven by apical uptake of divalent cations mediated by channels and transporters such as Trpm6/7 (for Mg^{2+}), Trpv5/6 (for Ca^{2+}) and Zip4 (for Zn^{2+}). Several carrier proteins such as calbindin-D9k/D28k (for Ca^{2+} and Mg^{2+}) and MT1 (for Zn^{2+}) deliver divalent cations to the basolateral cell surface. Slc41a1, Slc41a2, Slc41a3 and Cnnm4 (for Mg^{2+}), NCX and PMCA1b/ PMCA4 (for Ca^{2+}) and ZnT1/4 (for Zn^{2+}) are responsible for extrusion of divalent cations.

In the kidney, 90% of Mg^{2+} reabsorption occurs in the thick ascending limb via the paracellular pathway. Only 10% of Mg^{2+} is reabsorbed in the distal convoluted tubule (DCT) by the transcellular route. Mg^{2+} reuptake was undetectable in nephron segments distal to DCT [76, 77]. Therefore, it was suggested that DCT controls the final urinary Mg^{2+} content and thereby regulates the whole body balance of Mg^{2+} [76, 77]. The transcellular transport of Mg^{2+} occurs via tight junction proteins formed by claudin-16 and claudin-19 and is driven by the positive electrical potential of the lumen [75, 78-83].

In the transcellular pathway, the apically located Mg^{2+} channel TRPM6 was proposed to drive an apical Mg^{2+} entry in DCT [8, 84]. However, a recent study of our group demonstrated that genetic

inactivation of *Trpm6* in the kidney has a rather minor impact in this process [44]. A role of TRPM7 in renal reabsorption was extensively discussed in the literature [10, 44], but this concept has not been addressed yet in animal genetic models. Calbindin-D9k and -D28k were discussed as possible intracellular carriers; however, the *in vivo* evidence in favor of this concept is missing [85, 86]. *Slc41a3* may be involved in the basolateral extrusion step [87]. In accordance, *Slc41a3 KO* mice had decreased Mg^{2+} serum levels.

In the intestine, both para- and transcellular mechanisms operate to control the nutritional intake of Mg^{2+}. Both TRPM6 and TRPM7 were identified in intestinal enterocytes [44, 88] (Figure 4) and were suggested as prime players in the uptake of luminal Mg^{2+}. A recent study of our laboratory has shown that global or intestine-specific ablation of *Trpm6* causes a systemic Mg^{2+} deficit in mice. However, a particular *in vivo* role of *Trpm7* and other genes remains to be established. Several proteins were suggested to play a role in the basolateral extrusion of Mg^{2+} in the intestine including *Slc41a1*, *Slc41a2, Slc41a3* and *Cnnm4* (Figure 4) [87, 89-94]. Consistently, *Slc41a3* and *Cnnm4 KO* mice displayed reduced serum Mg^{2+} concentrations [87, 94].

2.3.2 Regulation of Ca^{2+} balance *in vivo*

Ca^{2+} is an essential divalent cation, which is required for many fundamental physiological processes [95]. Apart from the intestine and the kidney, bones play an important role in organismal Ca^{2+} balance since this tissue stores 99% of body Ca^{2+} [96, 97]. The concentration of Ca^{2+} in the serum is maintained in the range of 2.2–2.7 mM. Parathyroid hormone (PTH) and an active form of vitamin D (1,25-$(OH)_2D_3$) are well-known factors regulating circulating Ca^{2+} concentrations [97, 98]. When serum Ca^{2+} is reduced, PTH is released from parathyroid gland to the circulation system, what leads to enhanced production of 1,25-$(OH)_2D_3$ by the kidney [99]. 1,25-$(OH)_2D_3$ regulates Ca^{2+} uptake in the intestinal and renal epithelial cells acting as a transcriptional regulator of Ca^{2+} channels and transporters.

In the kidney, reabsorption of Ca^{2+} takes place primarily in the proximal tubule and in the thin ascending loop via the paracellular pathway build up by claudins-14, 16 and 19 (Figure 4) [98, 100, 101]. DCT maintains the transcellular transport of Ca^{2+}. Similar to Mg^{2+}, it was suggested that this process in DCT determines the urinary excretion rate of Ca^{2+}. In DCT, apical entry of Ca^{2+} is mediated by the TRPV5 channel (Figure 4). *Trpv5* KO mice displayed an increased renal excretion rate of Ca^{2+} [102]. Surprisingly, Ca^{2+} serum levels were not altered in *Trpv5* KO mice. Cytosolic Ca^{2+} was proposed to be carried out by calbindin-D28k and extruded by basolateral Na^+/Ca^{2+} exchanger (NCX) or plasma membrane Ca^{2+} ATPase 4 (PMCA4) (Figure 4) [103-106].

The Ca^{2+} selective TRPV6 channel was suggested as the main contributor for intestinal uptake of Ca^{2+} (Figure 4) [107]. TRPV6 was found to be located at the apical surface of intestinal enterocytes [108]. In addition, transcription of *Trpv6* is positively regulated by 1,25-$(OH)_2D_3$ or low dietary Ca^{2+}

treatment [102, 109] and is stimulated by 1,25-$(OH)_2D_3$ [110-112]. However, *Trpv6 KO* mice were viable, had normal Ca^{2+} serum levels and showed only a weak increase in serum PTH and 1,25-$(OH)_2D_3$. Moreover, further experiments with mouse models could not confirm a concept that TRPV6 is the gatekeeper of nutritional uptake of Ca^{2+} [113, 114].

Taken together, several ion channels and transporters have been suggested to play a critical role in 1,25-$(OH)_2D_3$ sensitive transport of Ca^{2+} in the kidney and intestine. However, the main route for apical uptake remains elusive.

2.3.3 Systemic Zn^{2+} homeostasis

Zn^{2+} is a vital trace element required for many cellular pathways [115, 116]. The World Health Organization (WHO) estimates that 800.000 deaths per year worldwide were due to insufficient nutritional intake of Zn^{2+} [116]. In the body, Zn^{2+} is mainly stored in skeletal muscles (60% of total body Zn^{2+}) and bones (30% of all Zn^{2+}) [115]. The concentration of Zn^{2+} in the serum is maintained in the range of 17-19 µM [115]. Hormones involved in organismal homeostasis of Zn^{2+} remain to be established. The kidney appears to play a minor role in body balance of Zn^{2+} [117, 118]. The small intestine (particularly duodenum) primarily controls both absorption and excretion of Zn^{2+} [119-121]. Zn^{2+} absorption takes place through trans- and paracellular routes [121].

The cellular balance of Zn^{2+} is thought to be regulated by Zn^{2+} transporters of two gene families [115]. Zinc transporter (ZnT, SLC30 family, ZnT1-10) reduce cytosolic Zn^{2+} levels by promoting Zn^{2+} efflux to extracellular space or entry of Zn^{2+} in intracellular vesicles, ER or mitochondria. Zip transporters (SLC39 family, Zip1-14) increase cytosolic Zn^{2+} concentrations by facilitating uptake of extracellular Zn^{2+} or by release of Zn^{2+} from intracellular membrane compartments [115]. Several of these ZnT and Zip genes are highly expressed in the small intestine [115]. However, the genetic evidence is available only for Zip4, ZnT1 and ZnT4. Thus, it was proposed that Zip4 mediates uptake of luminal Zn^{2+} [122, 123]. Cytosolic Zn^{2+} is likely bound to the carrier protein metallothionein 1 (MT1) [124, 125] and extruded at the basolateral side by ZnT1 and/or ZnT4 [126, 127] (Figure 4).

Mutations in the human Zip4 gene result in the disease “acrodermatitis enteropathica” (AE) characterized by a defective intestinal Zn^{2+} absorption [122, 128, 129]. The breastfed human infants lacking Zip4 are asymptomatic, but soon after weaning the affected subjects develop signs of Zn^{2+} deficiency including alopecia, dermatitis, diarrhea, growth retardation and many other symptoms. AE can be fatal unless the patients are not supplemented by Zn^{2+} [129]. Consistently, only weaned mice with conditional intestine-specific inactivation of *Zip4* start to develop an imbalance in Zn^{2+} homeostasis [130, 131], likely due to increased bioavailability of Zn^{2+} in breast milk [132]. Therefore it was suggested that additional transporters are capable to mediate Zn^{2+} uptake in the absence of Zip4 [133].

3 Aims

Currently, the physiological role of the kinase-coupled channel TRPM7 is surrounded by considerable controversy. In a previous study of our laboratory, the kidney- and intestine-specific mutagenesis of a genetically related channel-kinase, TRPM6, in mice enabled to define the physiological role of TRPM6 [44]. Thus, it was demonstrated that TRPM6 operates in the placenta and intestine to maintain organismal Mg^{2+} balance.

Accordingly, the present project aims to provide answers to key questions about the *in vivo* roles of kinase-coupled TRPM7 channels using cells deficient in TRPM7 and mice strains with a tissue-specific ablation of TRPM7. Specifically, the project aimed to address the following pertinent questions:

(1) What is the role of TRPM7 in cellular uptake of divalent cations?

(2) What is the role of TRPM7 for the reabsorption of divalent cations in the kidney?

(3) What is the role of TRPM7 for the absorption of divalent cations in the intestine?

(4) What is the role of TRPM7 kinase in pre- and postnatal growth and survival as well as the maintenance of mineral and tissue homeostasis?

4 Materials

4.1 Chemicals

Table 2: List of reagents used in the present study

Chemicals	Source
10mM dNTP Mix PCR Grade	Astral-Scientific, Taren Point, Australia
10x DIG RNA Labeling Mix	Roche, Rotkreuz, Switzerland
4-(2-hydroxyethyl)-1-piperazineethanesulfonic acid (HEPES)	Sigma-Aldrich, St. Louis, USA
5x Transcription buffer	Roche, Penzberg, Germany
$^{65}ZnCl_2$ (0.5 M HCl)	Perkin Elmer, Waltham, USA
Acetic acid 99%	Merck, Darmstadt, Germany
Acetic anhydride	Sigma-Aldrich, St. Louis, USA
Agarose (NEEO ultra quality)	Carl Roth, Karlsruhe, Germany
Agarose (Standard)	Sigma-Aldrich, St. Louis, USA
Anti-DIG-AP antibody	Roche, Rotkreuz, Switzerland
BCIP (5-bromo-4-chloro-3-indolyl-phosphate)	Promega, Madison, USA
Bovine serum albumin (BSA) >96%	Sigma-Aldrich, St. Louis, USA
Calcium chloride dihydrate ($CaCl_2$ * 2 H_2O)	Sigma-Aldrich, St. Louis, USA
Dako fluorescent mounting medium	Agilent Dako, California, USA
Diethylpyrocarbonate (DEPC)	Sigma-Aldrich, St. Louis, USA
Dithiothreitol (DTT)	Roth, Karlsruhe, Germany
DNA Gel Loading Dye (6X)	Sigma-Aldrich, St. Louis, USA
DPX mounting medium	Sigma-Aldrich, St. Louis, USA
Eosin G solution	Diapath, Martinengo, Italy
Ethanol 100% (EtOH)	Sigma-Aldrich, St. Louis, USA
Ethylenediaminetetraacetic acid (EDTA)	Sigma-Aldrich, St. Louis, USA
Ethylenediaminetetraacetic acid disodium salt dihydrate (Na_2EDTA * 2 H_2O)	Roth, Karlsruhe, Germany
Fetal bovine serum (FBS)	Thermo Fisher Scientific Inc., Schwerte, Germany
Ficoll 400	Sigma-Aldrich, St. Louis, USA
Formamide (100%)	Sigma-Aldrich, St. Louis, USA
Formamide (50%, hybridization cocktail)	Amresco, Solon, USA
GeneRuler 100 bp DNA Ladder	Thermo Fisher Scientific Inc., Schwerte, Germany

Glucose	Sigma-Aldrich, St. Louis, USA
Glycerol (steril)	Sigma-Aldrich, St. Louis, USA
Goat anti-rabbit antibody Alexa Fluor 488	Life Technologies, Carlsbad, USA
Goat serum (heat inactivated)	Sigma-Aldrich, St. Louis, USA
Hoechst 33342	Life Technologies, Carlsbad, USA
Hydrochloric acid (HCl) (37%)	Merck, Darmstadt, Germany
Isoflurane (100%)	Ecuphar GmbH, Greifswald, Germany
Jung tissue freezing medium	Leica Microystems GmbH, Nussloch, Germany
Lambda-Carrageenan	Sigma-Aldrich, St. Louis, USA
Levamisole	Sigma-Aldrich, St. Louis, USA
Lithium chloride (LiCl)	Sigma-Aldrich, St. Louis, USA
Magnesium chloride hexahydrate ($MgCl_2$ * 6 H_2O)	Sigma-Aldrich, St. Louis, USA
Maleic acid (100%)	Sigma-Aldrich, St. Louis, USA
Mayer’s hematoxylin solution	Diapath, Martinengo, Italy
NBT (nitro blue tetrazolium) Color Substrate (50 mg/ml)	Promega, Madison, USA
Nuclear Fast Red	Sigma-Aldrich, St. Louis, USA
Nuclease-free water	Thermo Fisher Scientific Inc., Schwerte, Germany
O’GeneRuler Low Range DNA Ladder	Thermo Fisher Scientific Inc., Schwerte, Germany
Paraffin	Sigma-Aldrich, St. Louis, USA
Paraformaldehyde (PFA)	Sigma-Aldrich, St. Louis, USA
Paraformaldehyde 16% in 1x PBS (16% PFA)	Electron Microscopy Sciences, Hatfield, United Kingdom
Penicillin-Streptomycin (10.000 units penicillin, 10 mg streptomycin/ml)	Thermo Fisher Scientific Inc., Schwerte, Germany
Phosphate-buffered saline (PBS, Dulbecco’s Phosphate Buffered Saline)	Sigma-Aldrich, St. Louis, USA
Polyvinylpyrrolidone (PVP)	Sigma-Aldrich, St. Louis, USA
Potassium chloride (KCl)	Sigma-Aldrich, St. Louis, USA
Potassium dihydrogen phosphate (KH_2PO_4)	Roth, Karlsruhe, Germany
Potassium hydroxide (KOH)	Roth, Karlsruhe, Germany
Rabbit anti-TRPM7 antibody AB15562	Millipore, Billerica, USA
RNAlater RNA Stabilization Reagent	Qiagen, Hilden, Germany
Roche Blocking Reagent	Roche, Penzberg, Germany

Roti GelStain	Roth, Karlsruhe, Germany
Rotiszint	Roth, Karlsruhe, Germany
Sodium acetate ($C_2H_3NaO_2$)	Sigma-Aldrich, St. Louis, USA
Sodium acid (NaN_3)	Sigma-Aldrich, St. Louis, USA
Sodium chloride (NaCl)	Roth, Karlsruhe, Germany
Sodium citrate dihydrate ($Na_3C_6H_5O_7$ * 2 H_2O)	Merck, Darmstadt, Germany
Sodium dextran sulfate	Sigma-Aldrich, St. Louis, USA
Sodium dihydrogen phosphate dihydrate (NaH_2PO_4 * 2 H_2O)	Roth, Karlsruhe, Germany
Sodium hydrogen phosphate dihydrate (Na_2HPO_4 * 2 H_2O)	Roth, Karlsruhe, Germany
Sodium hydroxide (NaOH)	Merck, Darmstadt, Germany
Sucrose	Sigma-Aldrich, St. Louis, USA
TMAC (Tetramethyl ammonium chloride)	Sigma-Aldrich, St. Louis, USA
Triethanolamine	Sigma-Aldrich, St. Louis, USA
Tris (2-Amino-2-hydroxymethyl-propane-1,3-diol)	Roth, Karlsruhe, Germany
Tris HCl (2-Amino-2-hydroxymethyl-propane-1,3-diol hydrochloride)	Sigma-Aldrich, St. Louis, USA
Triton X-100	Sigma-Aldrich, St. Louis, USA
tRNA from baker’s yeast	Roche, Penzberg, Germany
Trypsin-EDTA solution	Sigma-Aldrich, St. Louis, USA
Tween 20	Sigma-Aldrich, St. Louis, USA
Xylene	Sigma-Aldrich, St. Louis, USA
Zinc sulfate heptahydrate ($ZnSO_4$ * 7 H_2O)	Sigma-Aldrich, St. Louis, USA

4.2 PCR primers

All primers were acquired at Metabion, Planegg-Martinsried, Germany.

Table 3: Primers used for genotyping of mouse strains

Name	Sequence	Amplicon
Ksp1.3-Cre for	5`-GCA GAT CTG GCT CTC CAA AG-3`	420 bp
Ksp1.3-Cre rev	5`-AGG CAA ATT TTG GTG TAC GG-3`	
Trpm7 ki for	5`-AAT GGG AGG TGG TTT ACG-3`	195 bp
Trpm7 ki rev	5`-CTC AGA TCA CAG CTT ACA GTC A-3`	
Trpm7 wt for	5`-TCT GAG CTA AAA GTA TGA AGT C-3`	336 bp (wt); 446 bp (fl)
Trpm7 wt rev	5`-ATA CCA CAA AAT CTC TGC CCT CTA A-3`	
Villin1-Cre for	5`-CAT GTC CAT CAG GTT CTT GC-3`	205 bp
Villin1-Cre rev	5`-TTC TCC TCT AGG CTC GTC CA-3`	

Table 4: Primers used for qRT-PCR analyses

Name	Sequence	Amplicon
Abcc1 for	5`-GGA CAA GGT GGA GGG ACA T-3`	84 bp
Abcc1 rev	5`-CGG AGA GAG TCA TTC TGA ATC C-3`	
Abcc2 for	5`-TTT CCT GGA TTA CCT CCA ACC-3`	76 bp
Abcc2 rev	5`-GCC GAG CAG AAG ACA ATC A-3`	
Calbindin-D9k for	5`-CCT GCA GAA ATG AAG AGC ATT TT-3`	175 bp
Calbindin-D9k rev	5`-CTC CAT CGC CAT TCT TAT CCA-3`	
Claudin-16 for	5`-GGT TGC TTT TTG GCA GGA-3`	74 bp
Claudin-16 rev	5`-TAG TTC CTC TCA GGC CCA AC-3`	
Cyp27b1 for	5`-AGT GGG GAA TGT GAC AGA GC-3`	61 bp
Cyp27b1 rev	5`-GGA GAG CGT ATT GGA TAC CG-3`	
Dclk1 for	5`-TCT GTG GCA CCC CAA CAT A-3`	66 bp
Dclk1 rev	5`-CCA CCT TGA GGC CAT ATC C-3`	
Gclc for	5`-AGA TGA TAG AAC ACG GGA GGA G-3`	62 bp
Gclc rev	5`-TGA TCC TAA AGC GAT TGT TCT TC-3`	
Gpx2 for	5`-GTT CTC GGC TTC CCT TGC-3`	64 bp
Gpx2 rev	5`-TCA GGA TCT CCT CGT TCT GAC-3`	
Gss for	5`-TGT CCA ATA ACC CCA GCA AG-3`	87 bp
Gss rev	5`-TCA GTA GCA CCA CCG CAT T-3`	

Gsr for	5`-ACT ATG ACA ACA TCC CTA CTG TGG-3`	89 bp
Gsr rev	5`-CCC ATA CTT ATG AAC AGC TTC GT-3`	
Gsta1 for	5`-CTT CTG ACC CCT TTC CCT CT-3`	87 bp
Gsta1 rev	5`-GCT GCC AGG CTG TAG GAA C-3`	
Gsta2 for	5`-TCT GAC CCC TTT CCC TCT G-3`	85 bp
Gsta2 rev	5`-GCT GCC AGG ATG TAG GAA CT-3`	
Gsta3 for	5`-TGG ACA ACT TCC CTC TCC TG-3`	107 bp
Gsta3 rev	5`-TGC GTC ATC AAA AGG CTT C-3`	
Gstm1 for	5`-GCA GCT CAT CAT GCT CTG TTA-3`	76 bp
Gstm1 rev	5`-TTT CTC AGG GAT GGT CTT CAA-3`	
Gstm3 for	5`-TTA TGG ACA CCC GCA TAC AG-3`	75 bp
Gstm3 rev	5`-TCA AGA ACT CTG GCT TCT GCT-3`	
Gstp1 for	5`-TGT CAC CCT CAT CTA CAC CAA C-3`	94 bp
Gstp1 rev	5`-GGA CAG CAG GGT CTC AAA AG-3`	
Hprt for	5`-CTC ATG GAC TGA TTA TGG ACA GG-3`	135 bp
Hprt rev	5`-TTA ATG TAA TCC AGC AGG TCA GC-3`	
Lgr5 for	5`-CTG CCC ATC ACA CTG TCA CT-3`	172 bp
Lgr5 rev	5`-GCA GAG GCG ATG TAG GAG AC-3`	
Lrg for	5`-GGA GCA GCT ATG GTC TCT TG-3`	125 bp
Lrg rev	5`-AGT ATC AGG CAT TCC TTG AG-3`	
Lyz1 for	5`-GGC AAA ACC CCA AGA TCT AA-3`	104 bp
Lyz1 rev	5`-TCT CTC ACC ACC CTC TTT GC-3`	
Mgst2 for	5`-CGG ACG AGC AAG ACT AAA ACA-3`	113 bp
Mgst2 rev	5`-TGA ATA CAG GAT AAA ACT CCA AAG AG-3`	
MT1 for	5`-TGG ACC CCA ACT GCT CCT G-3`	185 bp
MT1 rev	5`-TCA GGC ACA GCA CGT GCA C-3`	
Muc2 for	5`-GAC CTG ACA ATG TGC CCA GA-3`	66 bp
Muc2 rev	5`-GGC AAA CAC AGT CCT TGC AG-3`	
Slc41a1 for	5`-CAT GGT GCT GGA CAT TGT G-3`	109 bp
Slc41a1 rev	5`-CAG GGT CAT TTC CAA GTT CC-3`	
Slc41a2 for	5`-GTT TAC ACG CCA GTT ATC AAC G-3`	77 bp
Slc41a2 rev	5`-TGG AGG TAG GTA GAA ATC CTG CT-3`	
Tff3 for	5`-GTA ACA ACC GTG GCT GCT G-3`	103 bp
Tff3 rev	5`-GAG CCT GGA CAG CTT CAA AA-3`	

Trpm6 for	5`-CAC CGC TTC CTC ACC ATC-3`	74 bp
Trpm6 rev	5`-CGC AAA AAT TTA TTA GTT GGT CCT-3`	
Trpm7 ex. 17 for	5`-AGT AAT TCA ACC TGC CTC AA-3`	287 bp
Trpm7 ex. 17 rev	5`-ATG GGT ATC TCT TCT GTT ATG TT-3`	
Trpv5 for	5`-ATT GAC GGA CCT GCC AAT TAC AGA G-3`	285 bp
Trpv5 rev	5`-GTG TTC AAC CCG TAA GAA CCA ACG-3`	
Trpv6 for	5`-ATC GAT GGC CCT GCG AAC T-3`	358 bp
Trpv6 rev	5`-CAG AGT AGA GGC CAT CTT GTT GCT G-3`	
Villin1 for	5`-ATC TCC CTG AGG GTG TGG A-3`	62 bp
Villin1 rev	5`-AGT GAA GTC TTC GGT GGA CAG-3`	
Ywhaz for	5`-TAA AAG GTC TAA GGC CGC TTC-3`	60 bp
Ywhaz rev	5`-CAC CAC ACG CAC GAT GAC-3`	
Zip4 for	5`-ACT TTG TGG ACT TTG TGT TCA GG-3`	193 bp
Zip4 rev	5`-GAG TAT GGA GCT CAG AGT CTT GG-3`	
Zip5 for	5`-AGG ACC TAG TGA GCA ATC AGA GG-3`	155 bp
Zip5 rev	5`-TTC TCC AAG ATC CCT TTT GTT CC-3`	
ZnT1 for	5`-TGG ATG TAC AAG TAA ATG GGA ATC T-3`	62 bp
ZnT1 rev	5`-GTC TTC AGT ACA ACC CTT CCA GTT A-3`	
ZnT2 for	5`-CAG AAG GAT TCT GGA AGT CAC C-3`	211 bp
ZnT2 rev	5`-CGG GAA GAC ACC CAG AGG-3`	
ZnT4 for	5`-TAG GTG GAT ACA TGG CAA ATA GC-3`	243 bp
ZnT4 rev	5`-AGT TCA TAT GGA TGG TTC TCT GC-3`	

Table 5: Primers used to generate ISH probe

Name	Sequence
Trpm7 ex17 for	5’-aattaaccctcactaaagggTGGCAGTTGAATTACTGGAACA-3’
Trpm7 ex17 rev	5’-taatacgactcactatagggTCATATTCAGCCGTCCCATC-3’

4.3 Enyzmes

Table 6: Enzymes with corresponding buffers used in the present study

Enzyme	Buffer	Source
Proteinase K	Proteinase K buffer	Roche, Rotkreuz, Switzerland
RNA polymerase T3	Transcription buffer	Roche, Rotkreuz, Switzerland
RNA polymerase T7	Transcription buffer	Roche, Rotkreuz, Switzerland
RNase A	RNA wash buffer	Roche, Rotkreuz, Switzerland
Taq DNA polymerase	Standard Taq buffer	Roche, Rotkreuz, Switzerland
Tru1I DNA polymerase	Buffer R	Thermo Fisher Scientific Inc., Schwerte, Germany

4.4 Buffers and solutions

Table 7: 50x Tris-acetate-EDTA (pH 8.5, TAE buffer)

Name	Composition	
50x TAE	242 g	Tris
	57 ml	Acetic acid (99%)
	100 ml	0.5 M EDTA (pH 8.0)
		pH to 8.5 with 5 M KOH
		ad 1000 ml dH_2O

Table 8: 0.5 M EDTA (pH 8.0)

Name	Composition	
0.5 M EDTA	186 g	$Na_2EDTA * 2 H_2O$
		pH to 8.0 with 10 M NaOH
		ad 1000 ml dH_2O

Table 9: Villi isolation buffer A (pH 7.4)

Name	Composition	
Villi isolation buffer A	1.12 g	NaCl
	1.59 g	$Na_3C_6H_5O_7$ * 2 H_2O
	22.4 mg	KCl
	218 mg	KH_2PO4
	401 mg	Na_2HPO_4 * 2 H_2O
		pH to 7.4 with HCl
		ad 200 ml dH_2O

Table 10: Villi isolation buffer B

Name	Composition	
Villi isolation buffer B	87.7 mg	EDTA
	15.4 mg	DTT (freshly added before use)
	200 mg	BSA (freshly added before use)
		ad 200 ml phosphate-buffered saline (PBS)

Table 11: HEPES buffered saline (HBS) (pH 7.4)

Name	Composition	
HBS	30 ml	5 M NaCl
	5.4 ml	1 M KCl
	5 ml	1 M HEPES
	10 ml	1 M Glucose
	1 ml	1 M $MgCl_2$
	2 ml	1 M $CaCl_2$
		pH to 7.4 with HCl
		ad 1000 ml dH_2O

Table 12: 4% PFA in PBS (used for histological examination of the intestine)

Name	Composition	
4% PFA	10 ml	16% PFA
	30 ml	PBS

Table 13: 0.4% PFA in PBS (used for histological examination of the intestine)

Name	Composition	
0.4% PFA	10 ml	4% PFA
	90 ml	PBS

4.5 Reagents used for *in situ* hybridization (ISH) of mouse kidney sections

Table 14: DEPC-treated water (RNase free water)

Name	Composition	
DEPC-treated water	2 l	dH_2O
	1 ml	100% DEPC
		Stir for 2 h and incubate overnight at room temperature (RT), autoclave for 15 min at 121 °C

Table 15: 20x Phosphate-buffered saline (PBS) (pH 7.5)

Name	Composition	
20x PBS	163.6 g	NaCl
	3.7 g	KCl
	28.8 g	Na_2HPO_4 * 2 H_2O
	4.05 g	KH_2PO_4
		pH to 7.5 with HCl
		ad 1000 ml dH_2O
		Stir for 5 h and incubate overnight at room temperature (RT), autoclave for 15 min at 121 °C

Table 16: 1x PBS (pH 7.5)

Name	Composition	
1x PBS	50 ml	20x PBS
	950 ml	DEPC-treated water

Table 17: 20% PFA (pH 7.5)

Name	Composition	
20% PFA	50 ml	20x PBS
	700 ml	DEPC-treated water
	200 g	PFA
		Heat for 1 h at 65 °C, pH to 7.5 using NaOH
		ad 1000 ml DEPC-treated water

Table 18: 4% PFA

Name	Composition	
4% PFA	160 ml	1x PBS
	80 µl	100% DEPC
		Stir for 5 h and incubate overnight at room temperature (RT), autoclave for 15 min at 121 °C
		ad 160 ml DEPC-treated water
	40 ml	20% PFA
		Heat (~65 °C) till everything is dissolved

Table 19: 0.4% PFA

Name	Composition	
0.4% PFA	196 ml	1x PBS
	98 µl	100% DEPC
		Stir for 5 h and incubate overnight at room temperature (RT), autoclave for 15 min at 121 °C
		ad 196 ml DEPC-treated water
	4 ml	20% PFA
		Heat (~65 °C) till everything is dissolved

Table 20: 1 M Tris (pH 8.0)

Name	Composition	
1 M Tris pH 8.0	60.57 g	Tris
		pH to 8.0 with HCl
		ad 500 ml DEPC-treated water

Table 21: 0.5 M EDTA (pH 8.0)

Name	Composition	
0.5 M EDTA (pH 8.0)	93.05 g	$Na_2EDTA * 2 H_2O$
		pH to 8.0 with NaOH
		ad 500 ml DEPC-treated dH_2O
	250 µl	100% DEPC
		Stir for 5 h and incubate overnight at room temperature (RT), autoclave for 15 min at 121 °C

Table 22: Proteinase K stock solution (10 mg/ml)

Name	Composition	
Proteinase K stock	100 mg	Proteinase K
	5 ml	1 M Tris (pH 8.0)
	30 µl	1 M $CaCl_2$
	5 ml	100% Glycerol (sterile)
		Aliquot and store at -20 °C

Table 23: Proteinase K working solution

Name	Composition	
Proteinase K buffer	10 ml	1 M Tris (pH 8.0)
	2.5 ml	0.5 M EDTA (pH 8.0)
	187.5 ml	DEPC-treated water
	600 µl	Proteinase K stock solution (10 mg/ml); added just before use

Table 24: Acetylation buffer

Name	Composition	
Acetylation buffer	3.72 g	Triethanolamine
	200 ml	DEPC-treated water
	500 µl or 1000 µl	Acetic anhydride – added just before use

Table 25: 10x salts buffer (pH 8.0)

Name	Composition	
10x Salts	11.40 g	NaCl
	1.404 g	Tris HCl
	0.134 g	Tris
	0.78 g	NaH_2PO_4 * 2 H_20
	0.71 g	Na_2HPO_4 * 2 H_20
	10 ml	0.5 M EDTA (pH 8.0)
		ad 100 ml DEPC-treated water

Table 26: Yeast tRNA solution

Name	Composition	
Yeast tRNA	500 mg	tRNA from baker's yeast
		ad 50 ml DEPC-treated water
		Make 1 ml aliquots and freeze (-20 °C)

Table 27: 50x Denhardt's solution

Name	Composition	
50x Denhardt's	1 g	BSA
	1 g	Ficoll 400
	1 g	PVP
		ad 100 ml DEPC-treated water

Table 28: Hybridization buffer (pH 8.0)

Name	Composition	
Hybridization buffer	100 µl	10x Salts solution
	500 µl	Formamide (50%)
	200 µl	Dextran sulfate (10%)
	100 µl	Yeast tRNA
	20 µl	50x Denhardt's solution
	80 µl	DEPC-treated water

Table 29: 5x maleic acid buffer (5x MAB) (pH 7.5)

Name	Composition	
5x MAB	21.91 g	NaCl
	29.02 g	Maleic acid (100%)
	18 g	NaOH
	450 ml	dH_20
		pH to 7.5 with HCl
		ad 500 ml dH_2O and filtrate

Table 30: 1x MAB containing Tween 20 (MABT)

Name	Composition	
1x MABT	2 ml	5x MAB
	8 ml	dH_2O
	50 µl	10% Tween-20

Table 31: 20x saline-sodium citrate (SSC) (pH 7.0)

Name	Composition	
20x SSC	175.3 g	NaCl
	88.2 g	Sodium citrate dihydrate
		pH to 7.0 with HCl
		ad 1000 ml dH_2O and autoclave

Table 32: Post-hybridization washing solution (Post-Hyb Solution)

Name	Composition	
Post-Hyb Solution	25 ml	20x SSC
	250 ml	Formamide (100%)
	5 ml	10% Tween-20
	220 ml	dH_2O

Table 33: 1 M Tris (pH 7.5, 8.0 or 9.5)

Name	Composition	
1 M Tris (pH 7.5, 8.0 or 9.5)	121.14 g	Tris
		pH to 7.5 with HCl (for 10x RNase wash buffer)
		pH to 8.0 with HCl (for RNase A stock solution)
		pH to 9.5 with HCl (for NTMT buffer)
		ad 1000 ml dH_2O, respectively

Table 34: 1 M $MgCl_2$

Name	Composition	
1 M $MgCl_2$	101.5 g	$MgCl_2$ * 6 H_2O
		ad 500 ml dH_2O

Table 35: 5 M NaCl

Name	Composition	
5 M NaCl	292.2 g	NaCl
		ad 1000 ml dH_2O and autoclave

Table 36: Preparation of stock solution of RNase A

Name	Composition	
RNase A Stock Solution	100 mg	RNase A
		Dissolve in 9 ml 0.01 M sodium acetat (pH 5.2)
		Heat to 100 °C for 15 min
		Cool to RT and add 1 ml 1 M Tris (pH 8.0)
		Aliquot in 400 µl in aliquots and freeze at -20 °C

Table 37: RNA wash buffer (10x)

Name	Composition	
RNA Wash Buffer (10x) *	400 ml	5 M NaCl
	50 ml	1 M Tris (pH 7.5)
	50 ml	0.5 M EDTA (pH 8.0)

*diluted 1:10 with DEPC-treated water for 1x RNA Wash Buffer

Table 38: 10x Blocking reagent

Name	Composition	
Blocking Reagent	10 g	Roche Blocking Reagent
	100 ml	1x maleic acid buffer (MAB)
		Heat to dissolve, autoclave, aliquot (5-10 ml) and freeze at -20 °C

Table 39: Alkaline phosphatase buffer (NaCl, Tris, $MgCl_2$, Tween-20, NTMT) (pH 9.5)

Name	Composition	
NTMT	4 ml	5 M NaCl
	10 ml	1 M $MgCl_2$
	20 ml	1 M Tris (pH 9.5)
	2 ml	10% Tween-20
	100 mg	Levamisole (add only to second wash and color reaction)

(prepare freshly on day of use)

Table 40: Staining solution

Name	Composition	
Staining Solution	4.5 µl	NBT Color Substrate
	2.5 µl	BCIP Color Substrate

4.6 Kits

Table 41: Kits used in the present study

Name	Source
1,25-Dihydroxy Vitamin D enzyme immunoassay (EIA)	Immunodiagnosticsystems, Boldon, United Kingdom
2x Absolute qPCR SYBR Green Mix	Thermo Fisher Scientific Inc., Schwerte, Germany
GeneChip WT Terminal Labeling Kit	Applied Biosystems, Foster City, USA
GenElute Mammalian Total RNA Miniprep Kit	Sigma-Aldrich, St. Louis, USA
Mouse Direkt PCR Kit	Biotool, South Loop West, USA
Mouse PTH 1-84 ELISA Kit	Immunotopics, San Clemente, USA
Mouse/Rat IGF-I Quantikine ELISA Kit	R&D Systems, Minneapolis, USA
QIAshredder	Qiagen, Hilden, Germany
Q-Plex™ Mouse Cytokine Inflammation Kit	Quansys Biosciences, Logan, USA
RevertAid H Minus First Strand cDNA Synthesis Kit	Thermo Fisher Scientific Inc., Schwerte, Germany
Thyroxine (T4) (Mouse/Rat) ELISA Kit	BioVision, Milpitas, USA
Zymoclean Gel DNA Recovery Kit	Zymo Research, Irvine, USA

4.7 Consumables

Table 42: List of consumables used in the study

Consumables	Source
15 ml and 50 ml falcons	Sarstedt, Nümbrecht, Germany
Biosphere tips with filters (10 µl, 100 µl, 200 µl and 1000 µl)	Sarstedt, Nümbrecht, Germany
Cell scrapers 25 cm	Sarstedt, Nümbrecht, Germany
Cover slips (24 x 60 mm)	Thermo Fisher Scientific Inc., Schwerte, Germany
GeneChip Mouse Gene 1.0 ST Array	Affymetrix, Santa Clara, USA
Hypodermic needle, Gauge 14	Braun, Melsungen, Germany
LightCycler 480 Multiwell Plate 96	Roche, Penzberg, Germany
LightCycler 480 Sealing Foil	Roche, Penzberg, Germany
Multi Channel Pipettes 200 µl	PeqLab, Crableck Lane, United Kingdom
Multiply-µStrip Pro 8-strips	Sarstedt, Nümbrecht, Germany
Neubauer chamber	Paul Marienfeld GmbH, Lauda-Königshofen, Germany
Omnifix U-40 syringes	Braun, Melsungen, Germany
Pasteur pipettes	Roth, Karlsruhe, Germany
Plastic pestles	Sigma-Aldrich, St. Louis, USA
Precision wipes	Kimtech Science, Surrey, United Kingdom
Ritter riplates (2 ml, 96 well)	Ritter, Schwabmünchen, Deutschland
Rotilabo disposable weighing tray	Roth, Karlsruhe, Germany
Serological pipettes (10 µl, 100 µl, 200 µl, 1000 µl)	PeqLab, Crableck Lane, United Kingdom
Serological pipettes (2 ml, 5 ml, 10 ml, 25 ml)	Sarstedt, Nümbrecht, Germany
Super polyethylene vials, 20 ml	Perkin Elmer, Waltham, USA
Superfrost Plus slides	Thermo Fisher Scientific Inc., Schwerte, Germany
T175 flasks	Greiner bio-one, Kremsmünster, Austria
T25 flasks	Sarstedt, Nümbrecht, Germany
TC dishes	Sarstedt, Nümbrecht, Germany
Tips (10 µl, 100 µl, 200 µl, 1000 µl)	Sarstedt, Nümbrecht, Germany
Tubes (0.5 ml, 1.5 ml, 2.0 ml)	Eppendorf, Hamburg, Germany
Vasco Sensitive L (gloves)	Braun, Melsungen, Germany
Whatman filters (liquid Scintillation Grade GF/B)	Whatman International Ltd, Maidstone, United Kingdom

4.8 Technical devices

Table 43: Equipment used in the present study

Device	Source
Analytical balance KERN ALT220	Kern & Sohn GmbH, Balingen, Germany
Aperio slide scanner AT2	Leica Biosystems, Wetzlar, Germany
Axiovert 40 CFL microscope	Carl Zeiss AG, Oberkochen, Germany
Balancer PCB	Kern & Sohn GmbH, Balingen, Germany
Biometra Professional Trio PCR cycler	Biometra, Göttingen, Germany
BioPhotometer Plus	Eppendorf, Hamburg, Germany
Brandel cell harvester 9600-X	Brandel, Gaithersburg, USA
CM 3050S Cryotom	Leica Biosystems, Wetzlar, Germany
Compact M DNA electrophoresis chamber	Biometra, Göttingen, Germany
Easypet 3 pipette	Eppendorf, Hamburg, Germany
Electrophoresis power supply	PeqLab, Crableck Lane, United Kingdom
GeneChip scanner 3000	Affymetrix, Santa Clara, USA
HERA 240 CO_2 cell culture incubator	Thermo Fisher Scientific Inc., Schwerte, Germany
Heraeus Pico 17 (bench centrifuge)	Thermo Fisher Scientific Inc., Schwerte, Germany
Heraeus T6060 drying chamber	Heraeus, Hanau, Germany
Infinity-3026 WL/26MX gel documentation system	PeqLab, Crableck Lane, United Kingdom
Liebherr MEDline (4°C) refrigerator	Liebherr, Bulle, Switzerland
LightCycler 480 II	Roche, Penzberg, Germany
MAXQ 6000 shaker	Thermo Fisher Scientific Inc., Schwerte, Germany
Metabolic cages	Acme Metal Products, Statesville, USA
Mettler Toledo XS 205	Mettler-Toledo, Columbus, USA
Micropipettes (10, 100, 200, 1000 µl)	PeqLab, Crableck Lane, United Kingdom
Microwave oven	Severin, Sundern, Germany
Multiplate reader FLUOstar Omega	Labtech, Offenburg, Germany
NanoDrop Spectrophotometer	Thermo Fisher Scientific Inc., Schwerte, Germany
Olympus CX41 microscope	Olympus, Tokyo, Japan
Thermo Scientific Forma 900 freezer (-80°C)	Thermo Fisher Scientific Inc., Schwerte, Germany
Thermomixer	Eppendorf, Hamburg, Germany

Vortex IKA MS3 basic	Ika, Staufen, Germany
Wallac 1414 Win Spectral Liquid Scintillation Counter	Perkin Elmer, Waltham, USA
WTW series pH 720 pH meter	inoLab, Weilheim, Germany
ZEISS LSM 880 Confocal Laser Scanning Microscope	Carl Zeiss AG, Oberkochen, Germany
Ziegra ice machine	ZIEGRA Eismaschinen, Isernhage, Deutschland

4.9 Software

Table 44: Software used in this study

Software	Source
CellSens 1.7.1 cell Imaging software	Olympus, Tokyo, Japan
ELISA Analyse	www.elisaanalysis.com
Environment R (version 3.1.2)	www.R-project.org
Expression Console (version 1.4.0)	Affymetrix, Santa Clara, USA
GraphPad Prism 7	GraphPad Software, La Jolla, USA
ImageScope	Leica Biosystems, Wetzlar, Germany
Ingenuity pathway analysis (IPA)	Qiagen, Hilden, Germany
IrfanView	Irfan Skiljan, Wien, Austria
LightCycler 480 Software	Roche, Penzberg, Germany
Microsoft 2007 Professional	Microsoft, Redmond, USA
Microsoft Office 2010	Microsoft, Redmond, USA
Universal ProbeLibrary System Assay Design	Roche, Penzberg, Germany
ZEN2.3 software	Carl Zeiss AG, Oberkochen, Germany

5 Methods

5.1 Mice strains used in the present study

For a tissue-specific introduction of a loss-of-function mutation in *Trpm7*, we used the *LoxP/Cre* approach and a recently generated mouse strain with a conditional *Trpm7* ^{fl} allele [59]. *Cre* recombinase recognizes 34 bp DNA sequence (*LoxP* sites) and enables to delete a genomic sequence located between two LoxP sites (often referred to as a 'floxed' sequence). *Cre*-induced deletion of exon 17 in *Trpm7* ^{fl} allele (Table 45) results in a frame-shift mutation (*Trpm7* $^{\Delta 17}$ allele) i.e. in null mutation of *Trpm7* [59]. For tissue-specific inactivation of *Trpm7*, transgenic mouse strains expressing Cre in a tissue-specific mode were used (Table 45).

Table 45: Mutant mouse lines used in this study

Mutant allele	Description	Genetic background	Source
Trpm7 ^{fl}	Conditional (floxed) mutation in *Trpm7*	129S6/SvEvTac	David Clapham's laboratory, Harvard Medical School, Boston, USA [59]
Trpm7 ^{ki}	Point mutation K1646R in *Trpm7*	129S6/SvEvTac	Masayuki Matsushita's laboratory, Mitsubishi Kagaku Institute of Life Science, Machida, Tokyo, Japan [65]
Villin1-Cre	*Villin1-Cre* transgene	C57BL/6J	Jackson Laboratory, Bar Harbor, Maine, USA (stock #004586) [134]
Ksp1.3-Cre	*Ksp1.3-Cre* transgene	C57BL/6J	Jackson Laboratory, Bar Harbor, Maine, USA (stock #012237) [135]

For inactivation of *Trpm7* in the epithelial cells of the whole intestine, *Villin1-Cre* [134] and for the ablation of *Trpm7* in renal epithelial cells of collecting duct, distal convoluted tubule *(*DCT) and thick ascending limb of Henle, *Ksp1.3-Cre* [135] was used (Table 45). To investigate a role of TRPM7 kinase, we used a mouse line with a 'kinase-dead' knock-in point mutation K1646R (*Trpm7* ^{ki} allele (Table 45)) resulting in a complete block of TRPM7 kinase catalytic activity in the whole body [65].

5.2 Breeding of gene-modified mice

To maintain the *Trpm7* $^{fl/fl}$ strain, we bred females with males homozygous for *Trpm7* ^{fl}. F1 *Trpm7* $^{fl/fl}$ females (8-10 weeks old) were used to generate animals carrying organ-specific mutations in *Trpm7* (Table 46). To generate mice lacking TRPM7 in the intestinal enterocytes, we crossed

Trpm7 $^{fl/fl}$ females with *Villin1-Cre*-positive *Trpm7* $^{fl/wt}$ males. F1 *Trpm7* $^{fl/fl}$*; Villin1-Cre* (Intestine KO) and *Trpm7* $^{fl/fl}$ (Control) male littermates were examined. To produce mice lacking TRPM7 in the renal epithelial cells, we crossed *Trpm7* $^{fl/fl}$ females with *Ksp1.3-Cre*-positive *Trpm7* $^{fl/fl}$ males. F1 *Trpm7* $^{fl/fl}$*; Ksp1.3-Cre* (Kidney KO) and *Trpm7* $^{fl/fl}$ (Control) male littermates were examined.
To produce mice with a global TRPM7 'kinase-dead' mutation, males and females heterozygous for the *Trpm7* ^{ki} allele were crossed. F1 *Trpm7* $^{ki/ki}$ (kinase-dead) and *Trpm7* $^{wt/wt}$ (Control) littermates were used for experiments.

Table 46: Generation of mice with global and tissue-restricted mutations of *Trpm7*

Targeted tissue	Breeding strategy	Expected F1 outcome [a]
Intestine	♂*Trpm7* $^{fl/wt}$*; Villin1-Cre x* ♀*Trpm7* $^{fl/fl}$	25% *Trpm7* $^{fl/fl}$*; Villin1-Cre* [b] 25% *Trpm7* $^{fl/fl}$ 25% *Trpm7* $^{fl/wt}$*; Villin1-Cre* 25% *Trpm7* $^{fl/wt}$
Kidney	♂*Trpm7* $^{fl/fl}$*; Ksp1.3-Cre x* ♀*Trpm7* $^{fl/fl}$	50% *Trpm7* $^{fl/fl}$*; Ksp1.3-Cre* [b] 50% *Trpm7* $^{fl/fl}$
Global	♂*Trpm7* $^{ki/wt}$ *x* ♀*Trpm7* $^{ki/wt}$	25% *Trpm7* $^{ki/ki}$ 50% *Trpm7* $^{ki/wt}$ 25% *Trpm7* $^{wt/wt}$

[a] Genotypes were determined using genomic DNA extracted from tail fragments.

[b] Mice were assumed to be homozygous for *Trpm7* $^{\Delta 17}$ allele in the cells expressing Cre.

Phenotypic assessments of *Trpm7* $^{ki/ki}$ and *Trpm7* $^{fl/fl}$*; Ksp1.3-Cre* mice were performed with 8-weeks old male littermates. Because of a high postnatal mortality rate, *Trpm7* $^{fl/fl}$*; Villin1*-Cre mice (both males and females) were investigated at 1, 3 or 5 days after birth.

5.3 Genotyping of mice

The genomic DNA was extracted from tail segments using Mouse Direct PCR Kit according to the manufacturer's protocol. DNA extracts were analyzed by allele-specific PCRs using the Biometra Professional Trio PCR Cycler. 0.5 µl DNA extract was added to the master mix as outlined in Table 47. PCR primers and expected PCR amplicons are described in Table 48. Settings of PCRs are shown in Table 49-Table 52.

Table 47: Composition of the PCR master mix

Reagent	Volume
2 x M-PCR OPTI™ Mix*	10 µl
Forward Primer	0.1 µl (100 pmol/µl)
Reverse Primer	0.1 µl (100 pmol/µl)
dH_20	9.3 µl

* from Mouse Direkt PCR Kit

Table 48: Primer pairs for specific alleles and length of the amplicon

Allele	Primer	Amplicon
Trpm7 ^{wt}	Forward primer: mTrpm7 wt for Reverse primer: mTrpm7 wt rev	336 bp
Trpm7 ^{fl}	Forward primer: mTrpm7 wt for Reverse primer: mTrpm7 wt rev	446 bp
Villin1-Cre	Forward primer: mVillin1-Cre for Reverse primer: mVillin1-Cre rev	195 bp
Ksp1.3-Cre	Forward primer: mKsp1.3-Cre for Reverse primer: mKsp1.3-Cre rev	420 bp
Trpm7 ^{ki}	Forward primer: mTrpm7 ki for Reverse primer: mTrpm7 ki rev	205 bp

Table 49: PCR settings for *Trpm7 ^{wt}* / *Trpm7 ^{fl}*

Step	Temperature	Time	Number of cycles
Initialization step	95 °C	05:00 min	1
Denaturation Annealing Elongation	95 °C 58 °C (-1 °C per cycle) 72 °C	00:30 min 00:30 min 01:00 min	10
Denaturation Annealing Elongation	95 °C 48 °C 72 °C	00:30 min 00:30 min 01:00 min	35
Final extension	72 °C	05:00 min	1
Cooling	16 °C	∞	1

Table 50: PCR conditions for *Villin1-Cre*

Step	Temperature	Time	Number of cycles
Initialization step	95 °C	02:00 min	1
Denaturation Annealing Elongation	95 °C 65 °C (-1.5 °C per cycle) 72 °C	00:20 min 00:15 min 00:10 min	10
Denaturation Annealing Elongation	95 °C 50 °C 72 °C	00:15 min 00:15 min 00:10 min	30
Final extension	72 °C	02:00 min	1
Cooling	16 °C	∞	1

Table 51: PCR settings for *Ksp1.3-Cre*

Step	Temperature	Time	Number of cycles
Initialization step	95 °C	02:00 min	1
Denaturation Annealing Elongation	95 °C 65 °C (-0.5 °C per cycle) 72 °C	00:20 min 00:15 min 00:10 min	10
Denaturation Annealing Elongation	95 °C 60 °C 72 °C	00:15 min 00:15 min 00:20 min	30
Final extension	72 °C	02:00 min	1
Cooling	16 °C	∞	1

Table 52: PCR conditions for *Trpm7* ^{ki}

Step	Temperature	Time	Number of cycles
Initialization step	95 °C	05:00 min	1
Denaturation Annealing Elongation	95 °C 65 °C (-1 °C per cycle) 72 °C	00:30 min 00:30 min 01:00 min	10
Denaturation Annealing Elongation	95 °C 55 °C 72 °C	00:30 min 00:30 min 01:00 min	40
Final extension	72 °C	05:00 min	1
Cooling	16 °C	∞	1

For genotyping of *Trpm7* ^{ki} and *Trpm7* ^{wt} alleles, PCR products were further exposed to *Tru1I* endonuclease for 16 h at 65 °C (Table 53). *Tru1I* digests the PCR product from *Trpm7* ^{wt} allele producing 120 and 85 bp fragments, whereas *Trpm7* ^{ki} amplicon (205 bp) remains unchanged.

Table 53: Conditions used for *Tru1I* digestion of *Trpm7* ^{ki} *and Trpm7* ^{wt} PCR amplicons

Reactant	Volume
PCR product	20 µl
Buffer R	2.5 µl
dH_2O	2.0 µl
Tru1I endonuclease	0.5 µl

PCR products were analyzed using agarose gel electrophoresis. Gels were prepared using agarose (1–3% m/v) and 15 µl Roti-GelStain dissolved in hot 1x TAE buffer. Either O'GeneRuler Low Range DNA Ladder or GeneRuler 100 bp DNA Ladder was used to estimate the size of PCR products. Gels were run for 25 min at 150 V and imaged using the Infinity-3026 WL/26MX gel documentation system. The obtained images were analyzed using IrfanView software.

5.4 Housing conditions of mice

5.4.1 Normal housing conditions

All experiments involving animals were in accordance with the EU Animal Welfare Act and were approved by the local councils on animal care (permit Nr. 55.2-1-54-2532-180-2016 and permit Nr. 55.2-1-54-2532-134-13 from the Government of Upper Bavaria). Mice were bred in the animal facility of the Walther Straub Institute of Pharmacology and Toxicology. Mice were kept in individually ventilated polycarbonate cages. Cages were changed weekly and were on a 12 h light/dark cycle with artificial lighting. Temperature and relative humidity were 22+/-1 °C and 50+/-5 %, respectively. For enrichment, animals received wood wool and bedding material. Breeding animals were maintained on multigrain chow Ssniff M-Z (Table 54) and regular drinking water from tap containing 20.4 mg/l Mg^{2+}, 79.6 mg/l Ca^{2+} and <0.2 mg/l Zn^{2+} (*ad libitum*). Litters were weaned at three weeks of age. Littermates were housed in cages as described above but that 'maintenance' chow Ssniff R/M-H was used (Table 54). All chows were purchased from Ssniff GmbH (Soest, Germany).

Table 54: Chows used for housing of mice

Chow	Composition	Total content of divalent cations		
		Mg^{2+} (%)	Ca^{2+} (%)	Zn^{2+} (%)
Regular for breeding	Ssniff M-Z (Zucht)	0.22	1.00	0.089
Regular for maintenance	Ssniff R/M-H (Haltung)	0.22	1.00	0.089
High Mg^{2+} chow	Ssniff M-Z + 0.53% Mg^{2+} *	0.75	1.00	0.089
High Ca^{2+} chow	Ssniff M-Z + 1.00% Ca^{2+}; + 0.55% P **	0.22	2.00	0.089
High Ca^{2+}/Mg^{2+} chow	Ssniff M-Z + 0.53% Mg^{2+} *; + 1.00% Ca^{2+}; + 0.55% P **	0.75	2.00	0.089

* Content of Mg^{2+} was increased using MgO;

** Content of Ca^{2+} was increased using $CaCO_3$ and $Ca(H_2PO_4)_2$ to avoid P deficiency.

5.4.2 Dietary Mg^{2+}, Ca^{2+} and Zn^{2+} fortifications of mice

For supplementation experiments with *Trpm7* $^{fl/fl}$*; Villin1-Cre* mice, breeding couples and their weaned offspring were maintained *ad libitum* on different dietary regimes as outlined in Table 55. The control diet was based on a regular Ssniff M-Z chow and deionized drinking water (dH_2O). For Mg^{2+} and Ca^{2+} supplementation, a regular Ssniff M-Z contained additional Mg^{2+} and Ca^{2+} salts as explained in Table 54. For Zn^{2+} supplementation, animals were fed by the standard Ssniff M-Z chow and dH_2O containing 0.1% Zn^{2+}. Finally, a 'triple diet' contained high levels of all three cations Mg^{2+}, Ca^{2+} and Zn^{2+} (Table 55). For determination of mortality rates, the breeding pairs and pups were examined twice per day. Dead pups and animals, which were expected to die within the next 24 h, were euthanized for ethical reasons, collected and genotyped. Kaplan-Meier distributions and statistical analysis were computed by the log-rank test using GraphPad Prism.

Table 55: Dietary treatments used for survival experiments

Diet	Chow	Drinking water
Control diet	Ssniff M-Z	dH_20
High Mg diet	High Mg^{2+} chow	dH_20
High Ca diet	High Ca^{2+} chow	dH_20
High Zn diet	Ssniff M-Z	dH_20 + 0.1% Zn^{2+}
Triple diet (high Mg^{2+}, Ca^{2+} and Zn^{2+})	High Ca^{2+}/Mg^{2+} chow	dH_20 + 0.1% Zn^{2+}

5.5 Collection of murine specimen

5.5.1 Collection of serum and bones

8 weeks old mutant and control mice were weighed (Balance PCB), anesthetized by isoflurane and euthanatized by cervical dislocation. Blood samples were collected by a cardiac puncture technique (using Omnifix U-40 syringe and hypodermic needle). In experiments with 1, 3 or 5 days old *Trpm7* $^{fl/fl}$; *Villin1*-Cre and *Trpm7* $^{fl/fl}$ pups, animals were euthanatized by beheading and released blood was collected by a 100 µl pipette. To isolate serum, the blood samples were incubated 20-40 min at RT and clots were removed by centrifugation (Heraeus Pico 17 centrifuge, 30 min, 3.500 rpm, RT). The clear serum fraction was removed and stored at -80 °C. Right tibias were dissected, cleaned from muscle tissue, dried overnight at 70 °C in a Heraeus drying chamber and kept at RT.

5.5.2 Collection of urine

To determine the urinary excretion rates of divalent cations, individual *Trpm7* $^{fl/fl}$; *Ksp1.3* and *Trpm7* $^{fl/fl}$ mice were maintained for 20 h in individual metabolic cages. Animals were supplied *ad libitum* with a regular chow and regular drinking water. The produced urine was collected and stored at -80 °C.

5.5.3 Isolation of villi for RNA isolation and microscopically examination

The whole intestine of 5 days old *Trpm7* $^{fl/fl}$; *Villin1-Cre* and *Trpm7* $^{fl/fl}$ mice was removed and cut longitudinally. The tissues were flushed 1 x with ice-cold PBS and 3 x with ice-cold PBS containing 1 mM DTT. Next, the tissues were incubated in 4 ml Villi isolation buffer A for 15 min on ice. Intestine was transferred to 1.5 ml buffer B and rotated (250 rpm) for 15 min at 10 °C (MAXQ 6000 shaker). After that, the samples were vortexed (Vortexer IKA MS3 basic) 5 x for 10 s (3.000 rpm). The intestine was removed and supernatants were centrifuged for 30 s at 13.000 g and 4 °C (Heraeus Pico 17). The pellets were flash frozen at -80 °C and used later for RNA isolation. The isolated villi were examined using an Olympus CX41 microscope and Cell Imaging software.

5.5.4 Isolation of villi from the small intestine for microarray analysis

The small intestine was removed from 5 days old *Trpm7* $^{fl/fl}$; *Villin1-Cre* and *Trpm7* $^{fl/fl}$ mice and cut longitudinally. After washing with 1 ml ice-cold PBS, the tissue was transferred in 1 ml RNAlater RNA Stabilization Reagent (RT). The samples were vortexed 20 x (3.000 rpm) for 10 s at RT. After removal of the remaining gut, the obtained villi fraction was examined visually using the Axiovert 40 CFL microscope. The villi were stored at 4 °C. Prior RNA isolation (5.7.1), the villi were collected by centrifugation for 1 min at 17.000 g (Heraeus Pico 17) at RT.

5.5.5 Isolation of kidney and duodenum for RNA isolation

To isolate RNA from the kidneys of *Trpm7* $^{fl/fl}$; *Ksp1.3-Cre* and *Trpm7* $^{fl/fl}$ animals, the left kidney was cut transversally. The whole upper part was quickly placed in 500 µl RNAlater RNA Stabilization Reagent. To prepare RNA from the duodenum, the proximal part (1 cm) of the intestine was removed and placed in 500 µl RNAlater RNA Stabilization Reagent (RT). The samples were incubated for 24 h at 4 °C and afterwards used for RNA isolation (5.7.1). For long-time storage, the tissue samples were kept frozen at -20 °C.

5.5.6 Isolation of mouse tissues for histological analysis

For the histological analysis of the intestine of P1 *Trpm7* $^{fl/fl}$; *Villin1-Cre* and *Trpm7* $^{fl/fl}$ mice, 1 cm segments of duodenum, jejunum, ileum and colon were dissected. For examination of lymphoid organs, the whole thymus and spleen were dissected and balanced. The tissues were incubated in 4% PFA in PBS for 24 h at 4 °C. Afterwards, the tissues were stored in 0.4% PFA in PBS at 4 °C.

5.5.7 Preparation of kidneys for *in situ* hybridization (ISH)

Kidneys of *Trpm7* $^{fl/fl}$; *Ksp1.3-Cre* and *Trpm7* $^{fl/fl}$ animals were removed and incubated in DEPC-treated 4% PFA in PBS and stored for 24 h at 4 °C. Afterwards, the tissues were incubated in DEPC-treated 0.4% PFA in PBS at 4 °C.

5.6 Cell culture

5.6.1 Culturing of HAP1 cells

Wildtype (parental) HAP1 clone (C631) and *TRPM7*-deficient clones (10940–01 and 10940–04) were reported previously [44] (Horizon Genomics, Vienna, Austria). Cells were cultured in Iscove's Modified Dulbecco's Medium (IMDM) supplemented with 10% FBS, 100 µg/ml streptomycin, 100 U/ml penicillin and 10 mM $MgCl_2$. Cells were cultivated in HERA 240 incubator at 37 °C and 5% CO_2. For maintaining of the lines, cells were grown until 80-90% confluency in T25 flasks, washed 1 x with PBS and treated with 3 ml trypsin-EDTA solution for 3 min at 37 °C. Trypsin treatment was stopped by adding 9 ml of IMDM. Cells were centrifuged for 2 min at RT and 1.200 rpm (Heraeus Pico 17). The cell pellets were resuspended (1:10 or 1:20) in IMDM in a new T25 flask.

5.6.2 Preparation of HAP1 cells for ICP-MS analysis

Wildtype HAP1 clone C631 and *TRPM7*-deficient clones 10940–01 and 10940–04 were grown in T175 cm^2 flasks as described above (section 5.6.1). At ~50% confluence, the medium was replaced by fresh IMDM medium without additional 10 mM $MgCl_2$. In some experiments, 50 µM $ZnSO_4$ was added to IMDM. Next, cells were cultured for additional 24 h, washed 1 x with PBS (RT), trypsinized and collected in 50 ml falcons. After centrifugation (3 min, 1.200 rpm, RT) and removal of the supernatant, the obtained cell pellets were resuspended in 1 ml PBS and passed to fresh 1.5 ml Eppendorf tubes. The cell suspension was centrifuged (3 min, 3.500 rpm, RT) and supernatants were removed. The cell pellets were dried overnight at 70 °C in a Heraeus drying chamber. The dried cell pellets were analyzed using ICP-MS at ALS Scandinavia (Sweden), as described in 5.8.

5.6.3 ^{65}Zn uptake assay

Wildtype HAP1 cells (clone C631) and a *TRPM7*-deficient cell line (clone 10940–04) were grown to ~ 90% confluency in T175 flasks and washed 1 x with PBS (RT). Afterwards, 10 ml PBS were added and cells were disaggregated using a cell scraper. After centrifugation (1.200 g, 3 min, RT), the cell pellets were resuspended in 10 ml HBS (RT). Cells were counted using the Neubauer chamber and cell densities were adjusted to a similar level (~$5*10^6$ cells/ml) using HBS. 600 µl of the cell suspension (~3 x 10^6 cells, quadruplicates) were pipetted to a 96 well Ritter Riplate. HBS was used to estimate a blank value. Next, 300 µl HBS containing 6 mM $^{65}ZnCl_2$ (2 mM final concentration) were added at 37 °C for different time intervals. Cells were harvested using

Whatman filter papers (for Liquid Scintillation Grade GF/B) and a Brandel cell harvester 9600-X. The filters were washed 4 x with 2 ml dH_20. The filters were placed in the Super polyethylene vials containing 5 ml Rotiszint lysis/scinctilation solution. After 24 h, radioactivity was detected with the Wallac 1414 Win Spectral Liquid Scintillation Counter. The obtained datasets were fitted using a nonlinear (least-squares) regression analysis (GraphPad Prism 7.3) and one-phase exponential association equation:

$$B = B_{max}(1 - e^{-K t})$$

with B - cellular content of $^{65}Zn^{2+}$ (dpm / µg protein), t - time (min), B_{max} - maximum $^{65}Zn^{2+}$ level at equilibrium (dmp / µg protein), K - a rate constant (min^{-1}). Statistical analysis was performed using the extra sum-of-squares F test (GraphPad Prism 7.3) with a threshold of $P \leq 0.05$.

5.7 Biochemical and molecular biology methods

5.7.1 RNA isolation and first strand cDNA synthesis

For RNA isolation, the GenElute Mammalian Total RNA Miniprep Kit was used. Tissue samples were removed from RNAlater RNA Stabilization Reagent and placed in a 1.5 ml plastic tube containing 500 µl lysis solution and 1% β-mercaptoethanol (both from GenElute Mammalian Total RNA Miniprep Kit). Tissues were homogenized by QIAshredder and RNA isolation was performed according to the manufacturer's protocol. The obtained RNA samples were diluted in 50 µl nuclease-free water. The concentration of RNA was determined spectroscopically at 260 nm with BioPhotometer plus. For the synthesis of cDNA, the RevertAid H Minus First Strand cDNA Synthesis Kit was used according to the manufacturer's protocol as outlined in Table 56 and Table 57. The produced cDNA samples were stored at -20 °C.

Table 56: Reaction mixture for cDNA synthesis

Reagents	Volume
mRNA	x µL (1 µg)
Random Hexamer Primer (100 µM)	1 µl
Nuclease-free water	x µl, to make up 12 µl
5x Reaction Buffer	4 µl
RiboLock RNase Inhibitor (20 u/µl)	1 µl
10 mM dNTP Mix	2 µl
RevertAid H Minus M-MuLV Reverse Transcriptase	1 µl

Table 57: Reaction conditions for cDNA synthesis

Temperature	Time
25 °C	5 min
42 °C	60 min
70 °C	5 min

5.7.2 Quantitative real-time polymerase chain reaction (qRT-PCR)

qRT-PCR was performed using a master mix (Table 58) pipetted in the LightCycler 480 Multiwell Plate (20 µl per well). Then, 5 µl/well diluted cDNA (1:5) were added. All pipetting steps were performed on ice. The plates were sealed using the LightCycler 480 sealing foil. Expression levels of target genes were normalized to expression levels of reference genes. For intestine samples, hypoxanthin-phosphoribosyl-transferase *(Hprt)* was used; for kidney samples, 14-3-3 protein zeta/delta (*Ywhaz*) was employed. PCR primers (Table 4) were designed using the Roche Assay Design Center software. qRT-PCR was performed using LightCycler 480 II and conditions shown in Table 59. Analysis of the data was performed with the LightCycler 480 software. The relative mRNA expression levels were calculated using the $2^{-\Delta\Delta Ct}$ approach. Statistical analysis was performed using an unpaired Student's t-test with Excel (Microsoft Office 2010).

Table 58: qRT-PCR master mix

Reagents	Volume
2x Absolute qPCR SYBR Green Mix	12.5 µl
Primer forward (100 µM)	0.1 µl
Primer reverse (100 µM)	0.1 µl
Nuclease-free water	7.3 µl

Table 59: qRT-PCR settings

Step	Temperature	Time	Cycles
Initialization step	95 °C	15:00 min	1
Denaturation Annealing Elongation	95 °C 60 °C 72 °C	00:15 min 00:15 min 00:30 min	40
Melting curve analysis	95 °C 60 °C	00:10 min 01:00 min	1
Cooling	40 °C	∞	1

5.7.3 *In situ* hybridization (ISH)

To examine the efficiency of the *Trpm7* gene deletion via *Ksp1.3-Cre* recombinase in *Trpm7* $^{fl/fl}$; *Ksp1.3-Cre* mice in the kidney, we used *in situ* hybridization (ISH). ISH was performed in collaboration with the laboratory of Dr. David Simmons, Brisbane, Australia. cDNA templates for the generation of cRNA *Trpm7* probes were produced using PCR as outlined in Table 60 and Table 61. The primers contained either T7 or T3 promoter RNA polymerase sites.

Table 60: Composition of PCR mix to produce ISH probes

Reagent	Concentration	Volume
Taq DNA polymerase	5 U/ml	0.1 µl
Standard Taq buffer	1x	2 µl
dNTPs	10mM	0.4 µl
cDNA	1x	2 µl
Primer mix (Trpm7 ex17 for/rev)	10mM	2 µl
TMAC	1x	2 µl
RNase free water	1x	11.5 µl

Table 61: PCR settings used for generation of ISH probes

Step	Temperature	Time	Cycles
Initialization step	94 °C	03:00 min	1
Denaturation Annealing Elongation	94 °C 62 °C 72 °C	00:30 min 00:30 min 00:45 min	35
Final Extension	72 °C	05:00 min	1
Cooling	4 °C	∞	1

The PCR products were separated using agarose gel electrophoresis. The corresponding PCR products were cut from the gel, purified using the Zymoclean Gel DNA Recovery Kit according to the manufacturer's protocol and quantified by the NanoDrop spectrophotometer. To produce Digoxigenin (DIG)-labelled sense and antisense ISH probes, the purified PCR products were incubated either with T3 RNA or T7 RNA polymerase at 37 °C for 90 min as shown in Table 62.

Table 62: Components for production of sense and antisense RNA probes

Reagent	Volume
Reagent	x µl (100 ng)
Purified PCR product	1 µl
5x Transcription buffer	1 µl
10x DIG RNA Labeling mix	2 µl
RNA polymerase T3/T7	1 µl
RNase free water	*ad* 20 µl

The synthesis was stopped by addition of 1 µl 0.2 M EDTA, 1.25 µl 4 M LiCl and 37.5 µl EtOH (100%). The reaction mixtures were incubated overnight at -20 °C. ISH probes were precipitated by centrifugation at 13.000 rpm for 20 min at 4 °C. The pellets were washed with 500 µl EtOH (70%) and centrifuged for 10 min at 13.000 rpm at 4 °C. Supernatants were removed and the pellets were resuspended in 11 µl RNase free water. The generated ISH probes were diluted 1:10 in hybridization buffer and stored at -80 °C.

For paraffin embedding of fixed kidneys isolated from *Trpm7* $^{fl/fl}$; *Ksp1.3-Cre* and *Trpm7* $^{fl/fl}$ mice (5.5.7), the tissues were washed 3 x in PBS, incubated for 1 h in 70% EtOH and 1 h in 100% EtOH. Afterwards, the tissues were incubated in 100% xylene for 1 h and in 3 paraffin baths (2x 30 min and 1x 1 h). The tissues were embedded in paraffin wax blocks. The blocks were used to produce 7 µm sections (Cryotom CM 3050S) and transferred onto the Superfrost plus slides. Slides were dewaxed 2x in 100% xylene for 10 min. After rehydration with decreasing concentrations of EtOH (2x 100% for 10 min and 95%, 70%, 50% as well as 30% for 5 min) and following a 5 min wash in PBS, the slides were fixed in 4% PFA in PBS for 10 min and washed 2x in PBS for 5 min. The slides were placed into proteinase K buffer for 20 min and washed 1x with PBS, 1x in 4% PFA in 1x PBS and 1x in PBS for 5 min, respectively.

The ISH probes were further diluted (1:2.000) in a hybridization buffer and heated at 70 °C for 10 min. Next, the probes were added to the kidney sections (150-200 µl per section) and hybridized overnight in a sealed humidified box at 65 °C. The slides were washed 2x in pre-heated post-hybridization wash solution at 65 °C for 30 min, followed by 2 washes in 1x MABT at RT for 30 min. Next, the slides were washed in 1x RNA wash buffer 3x at 37 °C (1st wash 10 min, 2nd wash 30 min, 3rd wash 5 min), whereupon RNase A (400 µl RNase A Stock Solution per 200 ml) was added into the 2nd wash. After that, the slides were washed 5 min at RT in 1x MABT. For blocking, the slides were covered with 300 µl 1x MABT with 2% blocking reagent stock and 20% heat-inactivated goat serum for 1 h (blocking solution). Afterwards, anti-DIG-AP antibody was diluted in blocking solution (1:2.500). 300 µl of the solution were added on each slide, covered by a cover slip and incubated at 4 °C overnight in a humidified chamber.

All further steps were performed at RT. First, slides were washed 4x in 1x MABT for 15 min.

Afterwards, the slides were washed with NTMT and NTMT with added levamisole for 10 min, respectively. Slides were covered with cover slips after addition of 300 µl staining solution. The color reaction was developed for 3 days. When purple staining was detectable, the reaction was stopped with PBS wash. Slides were rinsed for 1 min with dH_2O. Afterwards, the slides were immersed in Nuclear Fast Red (30 s) and rinsed again for 1–2 min in tap water. Next, slides were dehydrated through alcohol washes in increasing concentrations followed by xylene (30%, 50%, 70%, 95%, 2x 100% EtOH for 1 min, respectively; 2x xylene for 2 min, respectively). Finally, slides were mounted in DPX mounting medium, covered by cover slips and air dried. Slides were imaged by the Aperio slide scanner and examined using the ImageScope software.

5.7.4 Whole-genome profiling of the villi transcriptome

Isolation of intestinal villi and RNA is described under 5.5.4 and 5.7.1, respectively. Whole genome profiling was conducted using the Affymetrix GeneChip Mouse Gene 1.0 ST Array at Source Bioscience (Berlin, Germany) as described previously [44]. Processing of the array data, including background correction, quality assessment and normalization was performed with the Affymetrix Expression Console (version 1.4.0). Differential expression analysis was performed with the DNASTAR ArrayStrar 11.0 software. P-values (Student's t-test) were adjusted for multiple testing by the Benjamini-Hochberg method for controlling the false discovery rate (FDR). Analysis of the affected gene networks was performed by the Ingenuity pathway analysis (IPA) computer environment using a set of 455 transcripts with ≥ 2.0-fold change at $P \leq 0.05$. Microarray data were deposited in NCBI Gene Expression Omnibus (GEO) (GSE110613).

5.7.5 Enzyme-linked immunosorbent assays (ELISA)

For analysis of serum IGF-1, we used the Mouse/Rat IGF-1 Quantikine ELISA Kit. The content of thyroxine (T4) was determined by the Thyroxine (T4) (Mouse/Rat) ELISA Kit. Levels of parathyroid hormone (PTH) were measured using the Mouse PTH 1-84 ELISA Kit. Analysis of cytokines was performed by Quansys Biosciences using the Q-Plex™ Mouse Cytokine Inflammation Kit. For determination of 1,25-dihydroxy vitamin D we used the 1,25-Dihydroxy Vitamin D EIA. For the 1,25-Dihydroxy Vitamin D assay, samples from 3-7 animals were combined since 100 µl was the minimum sample volume. Procedures were performed according to the manufacturer`s protocols. Color reactions were analyzed using the plate reader FLUOstar Omega. Data were analyzed using Excel 2010 (Microsoft 2007 Professional) and ELISA Analysis.

5.8 Inductively coupled plasma mass spectrometry (ICP-MS)

The content of main elements in HAP1 cells, serum, bones and urine samples was determined by inductively coupled plasma mass spectrometry (ICP-MS). The measurements were performed at ALS Scandinavia (Sweden) as reported earlier [44, 66, 136, 137].

5.9 Histological examination of the intestine

The experiments were performed in collaboration with Dr. Camilla Recordati (Mouse and Animal Pathology Laboratory, Filarete Foundation, Milan, Italy). Tissues (5.5.6) were dehydrated through a series of ethanol washes and cleared in three changes of xylene. Afterwards, the samples were embedded in paraffin. Tissue sections (4 µm) were mounted on Superfrost Plus slides and dried at 70 °C for 1 h. Tissue sections were dewaxed in xylene and rehydrated through a series of ethanol washes to dH_2O. Slides were incubated in Mayer's hematoxylin solution for 10 min at RT followed by incubation in 0.5% Eosin G solution for 10 min at RT. The color reaction was stopped by deionized water. Slides were dehydrated in ethanol, cleared in xylene and mounted in mounting medium. Slides were examined using the DM2500 light microscope.

5.10 Immunohistochemistry of the intestine

Dissected duodenal samples from 8-week old control mice or P5 *Trpm7* $^{fl/fl}$; *Villin1-Cre* and *Trpm7* $^{fl/fl}$ mice were fixed in 4% (w/v) PFA in 1x PBS for 2 h (RT). After incubation in 1x PBS for 1 h (RT), tissues were incubated for 24 h (4 °C) in 18% sucrose in 1x PBS. Next, tissues were embedded in Jung tissue freezing medium. Cryosections (16 µm) were produced by CM 3050S cryotome, mounted on Superfrost Plus slides and air-dried for 20 min (RT). Sections were washed in 1x PBS (3x 5 min, RT) and blocked in 1x PBS supplemented with 10% goat serum, 3% BSA and 0.3% Triton X-100 (blocking solution) for 1 h (RT). The rabbit anti-TRPM7 antibody AB15562 was incubated overnight in blocking solution (4 °C). Sections were washed in 1x PBS containing 0.05% Tween 20 (TBST, 3x 5 min, RT) and 1 µg/ml of Alexa Fluor 488 goat anti-rabbit antibody was applied in 1x PBS containing 0.02 % sodium acid (m/v) and 0.5 % lambda-Carrageenan (m/v) for 2h (RT). After washing in PBST (3x 5 min, RT), slides were stained with Hoechst 33342 in PBST (10 µg/ml) and embedded in Dako Fluorescent Mounting Medium. Confocal images and differential interference contrast (DIC) were obtained by a confocal laser scanning microscope (LSM 880 AxioObserver). A C-Apochromat 63x/1.2 W objective, 410–501 nm and 493–630 nm filters and 405 nm and 488 nm excitation wavelengths were used. Images were analyzed by the ZEN2.3 software.

5.11 Statistical analysis

Otherwise indicated differently, data were analyzed using Excel 2010 (Microsoft 2007 Professional) and presented as mean value ± standard error of the mean (SEM). Statistical analysis was conducted using Student's t-test (two-tailed distribution, two-sample equal variance).

6 Results

6.1. Assessment of the TRPM7 function in cultured cells

One of the main goals of this thesis was to investigate whether the TRPM7 channel is capable to regulate cellular levels of divalent cations. To avoid pitfalls often caused by overexpression of the recombinant ion channels, we studied a human haploid leukemia (HAP1) cell line carrying a loss-of-function mutation in the *TRPM7* gene. HAP1 cells are haploid and well accessible to CRISPR/Cas9-mediated mutagenesis [138, 139]. As reported previously [44], the *TRPM7*-deficient HAP1 cells lack endogenous TRPM7 currents. In addition, the *TRPM7*-deficient HAP1 cells displayed a proliferation defect when cultured in a regular cell culture medium, recapitulating the phenotype of other *Trpm7* gene-deficient cell lines, such as the chicken B lymphoma cell line DT-40 [17], mouse embryonic stem cells [43] and trophoblast stem cells [6, 44] derived from *Trpm7*-deficient embryos. In line with other TRPM7-deficient cell lines, the proliferation arrest of HAP1 cells could be rescued by addition of 10 mM Mg^{2+} in the culture medium [6, 17, 44], supporting the idea that the TRPM7 channel is required for the cellular balance of Mg^{2+}.

In the present study, we asked whether TRPM7 is required to maintain the cellular content of other divalent cations including Ca^{2+} and Zn^{2+}. Total cellular levels of Mg^{2+} are in the range of 5–10 mM, while cytosolic free Mg^{2+} only amounts to 0.5–1 mM, since ~90% of Mg^{2+} is bound to ATP and other metabolites [42]. Cytosolic levels of free Ca^{2+} are in the range of 50–100 nM, whereas the total content of Ca^{2+} is ~1 mM [140]. Zn^{2+} content in cells was estimated to be in the range of 10–100 µM, whereas the cytosolic concentration of free Zn^{2+} is in the pico- to low nano-molar range because most Zn^{2+} is bound to proteins [115]. Hence, free cytosolic concentrations of a particular divalent cation may not be reliably used to score changes in the cellular balance of this cation. To address a role of TRPM7, we opted for inductively coupled plasma mass spectrometry (ICP-MS), an analytical method well suitable to study total cellular levels of divalent and monovalent cations [136, 137].

In our experimental settings, TRPM7 KO and WT (parental) cells were cultured in a medium containing additional Mg^{2+} (10 mM Mg^{2+}). 24 h prior ICP-MS analysis, the medium was replaced by a fresh regular medium (without additional Mg^{2+}). After 24 h, we collected the cells, obtained dried cell pellets and conducted ICP-MS analysis. We found that *TRPM7* HAP1 KO cells were depleted in Mg (12%) and Zn (7%). Cellular Ca showed a tendency to reduction (11%), but this difference was not statistically significant (Figure 5).

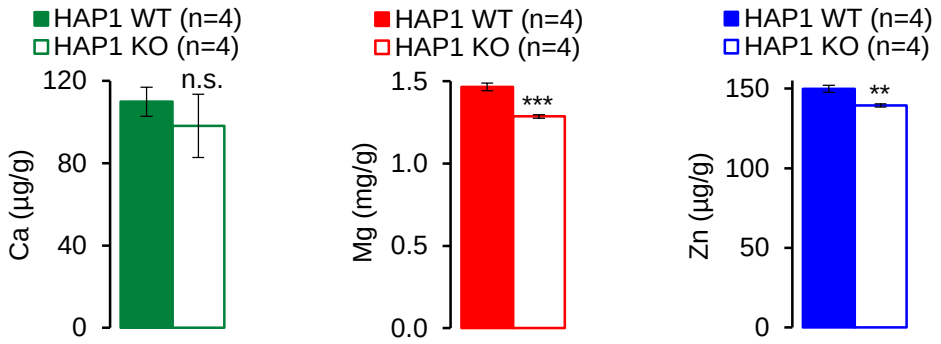

Figure 5: Determination of elementary levels of divalent cations in WT and TRPM7 KO HAP1 cells. Total contents of Ca *(left panel)*, Mg *(middle panel)* and Zn *(right panel)* were determined using ICP-MS and normalized to dry cell pellet weight (mean ± SEM); *** - P≤0.001; ** - P≤0.01; n.s. - not significantly different (Student's t-test). n - number of independent measurements.

To further verify the impact of the loss-of-function mutation in *TRPM7* on the cellular balance of divalent cations, we determined ratios of individual divalent cations to total content of sulfur (Figure 6 A, as a proxy for total content of proteins and amino acids), rubidium (Figure 6 B, as a proxy for K with less prone to environmental contamination) and phosphorus (Figure 6 C, as a proxy for total contents of DNA, RNA and nucleotides). This analysis was in line with our previous conclusions that TRPM7-deficient cells contained less Mg and Zn (Figure 5). Taken together, our results suggest that *TRPM7* HAP1 KO cells are deficient in Mg and Zn.

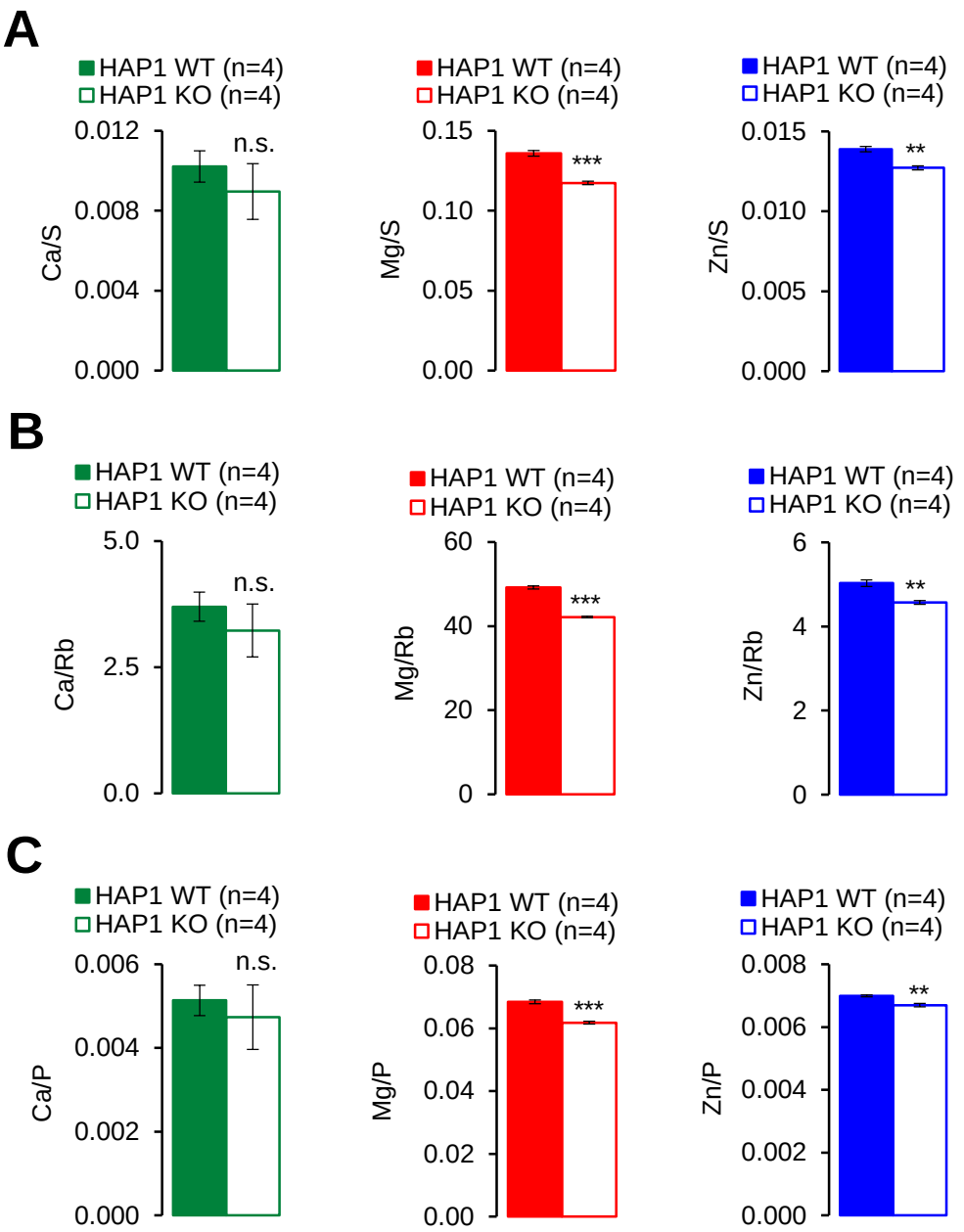

Figure 6: Relative levels of Ca, Mg and Zn in WT and TRPM7 KO HAP1 cells. Total elementary contents of divalent metals shown in Figure 5 were normalized to total elementary contents of **(A)** sulfur (S), **(B)** rubidium (Rb) and **(C)** phosphorus (P). Results are represented as mean ± SEM. *** - P≤0.001; ** - P≤0.01; n.s. - not significantly different (Student's t-test). n - number of independent measurements.

While a role of TRPM7 in maintaining the cellular Mg^{2+} homeostasis is well documented in the literature [6, 17, 43, 44], our finding that TRPM7-deficient cells display reduced Zn^{2+} levels was rather unexpected. Therefore, we asked whether, similar to the situation with Mg^{2+} deprivation in TRPM7 KO cell lines [17, 44], Zn^{2+} deficiency in *TRPM7* KO HAP1 cells can be ameliorated by the addition of exogenous Zn^{2+} to the cell culture medium. We added 50 µM Zn^{2+} to the regular medium (containing ~3 µM Zn^{2+}), incubated the cells for 24 h in this medium, and analyzed the dried cell pellets using ICP-MS. We found that Zn contents were increased in both WT and *TRPM7* KO HAP1

cells maintained in the Zn^{2+}-supplemented medium (Figure 7), suggesting that additional Zn^{2+} uptake mechanisms exist in HAP1 cells. Furthermore, we observed that total Zn levels in control and TRPM7-deficent cells treated with Zn^{2+}-enriched medium were equal.

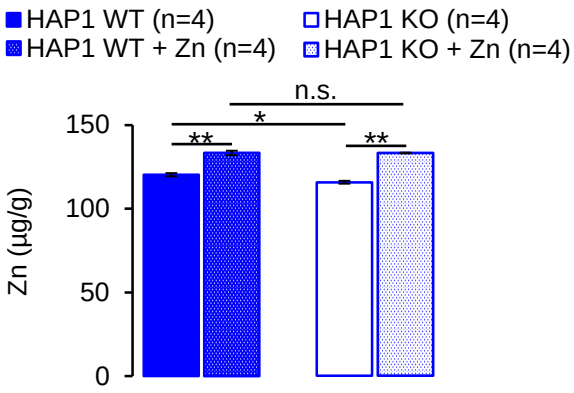

Figure 7: Determination of elementary Zn levels in WT and TRPM7 KO HAP1 cells grown in Zn enriched medium. Dried cell pellets were obtained from WT and KO HAP1 cells cultured in a standard cell culture medium or in a medium containing additional 50 µM $ZnSO_4$ for 24 h and analyzed by ICP-MS. Total elementary Zn contents were normalized to dry pellet weight and represented as mean ± SEM; ** - P≤0.01; * - P≤0.05; n.s. - not significantly different (One-Way ANOVA); n - number of independent measurements.

Next, we investigated whether inactivation of TRPM7 in HAP1 cells will reduce the uptake of radioactive $^{65}Zn^{2+}$ in resting cells kept in saline containing physiological levels of divalent cations. We incubated *TRPM7* HAP1 KO and WT cells in a buffer containing Mg^{2+} (1 mM), Ca^{2+} (2 mM) and $^{65}Zn^{2+}$ (2 µM) and determined the time-dependent $^{65}Zn^{2+}$ accumulation. The datasets were fitted by a one-phase exponential association equation. *TRPM7*-deficient HAP1 cells were characterized by a downward shift of $^{65}Zn^{2+}$ uptake rate when compared to WT cells (P=0.0005, F-test) (Figure 8). The rate constant (K) was not altered (P=0.72, F-test), but the maximum $^{65}Zn^{2+}$ uptake at equilibrium (B_{max}) was significantly decreased in *TRPM7* HAP1 KO cells (P=0.0017, F-test). These data suggest that native TRPM7 regulates Zn^{2+} uptake in resting cells in the presence of physiological concentrations of Ca^{2+} and Mg^{2+}.

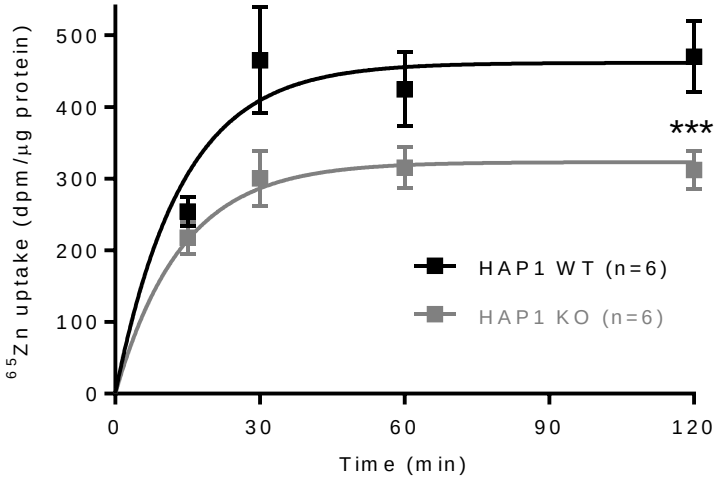

Figure 8: Assessment of $^{65}Zn^{2+}$ uptake in HAP1 WT and TRPM7 KO cells. HAP1 WT and *TRPM7*-deficient HAP1 KO cells were incubated in the presence of 2 µM $^{65}Zn^{2+}$, 1 mM Mg^{2+} and 2 mM Ca^{2+}. The time-dependent accumulation of $^{65}Zn^{2+}$ was determined. The results (mean ± SEM) were fitted by one-phase exponential association equation; *** - P≤0.001 (One-Way ANOVA); n - number of independent measurements.

Collectively, our results support the notion that TRPM7 regulates the uptake of Zn^{2+} and Mg^{2+} on a cellular level.

6.2 Strategy for the evaluation of TRPM7's function on organismal mineral homeostasis

As TRPM7 plays a critical role in cellular homeostasis of divalent cations, we asked whether TRPM7 regulates the transport of divalent metals in epithelial cells of the kidney and the intestine. To address this question, we generated new mouse strains with mutations resulting in organ-specific deletion of TRPM7. We used a mouse strain carrying two intronic LoxP sites flanking exon 17 of the *Trpm7* gene *(Trpm7 ^{fl})* (Figure 9 A) [59]. Deletion of exon 17 by a *Cre* recombinase results in a frame-shift mutation (*Trpm7 $^{\Delta 17}$* allele) (Figure 9 A) disrupting the TRPM7 channel and the kinase activity [59]. For inactivation of *Trpm7* specifically in the intestinal and renal epithelium, *Trpm7 $^{fl/fl}$* mice were crossed with *Villin1-Cre* and *Ksp1.3-Cre* transgenic mice. *Villin1-Cre* is expressed in the enterocytes of the whole intestine starting from embryonic day 12.5 [134] and is frequently used for a constitutive deletion of floxed alleles in this organ. Pioneering studies proposed the concept that the final urinary content of Ca^{2+} and Mg^{2+} is determined by the distal convoluted tubule (DCT) of the kidney. Accordingly, DCT may play a critical role in the whole-body balance of divalent cations [76, 141]. Since there is no *Cre* transgene available only active in DCT cells, *Ksp1.3-Cre* transgenic mice are used for deletion of floxed alleles in this field [135], because *Ksp1.3-Cre* drives expression of Cre in the epithelial cells of collecting duct, DCT and thick ascending limb of Henle. Consequently, our breeding of *Trpm7 $^{fl/fl}$* with *Villin1-Cre* and *Ksp.1.3-Cre* transgenic mice resulted in offspring, which presumably lacked TRPM7 protein specifically in the intestinal and the renal epithelium referred to *Trpm7 $^{Intestine\ KO}$* (Figure 9 B) and *Trpm7 $^{Kidney\ KO}$* (Figure 9 C), respectively.

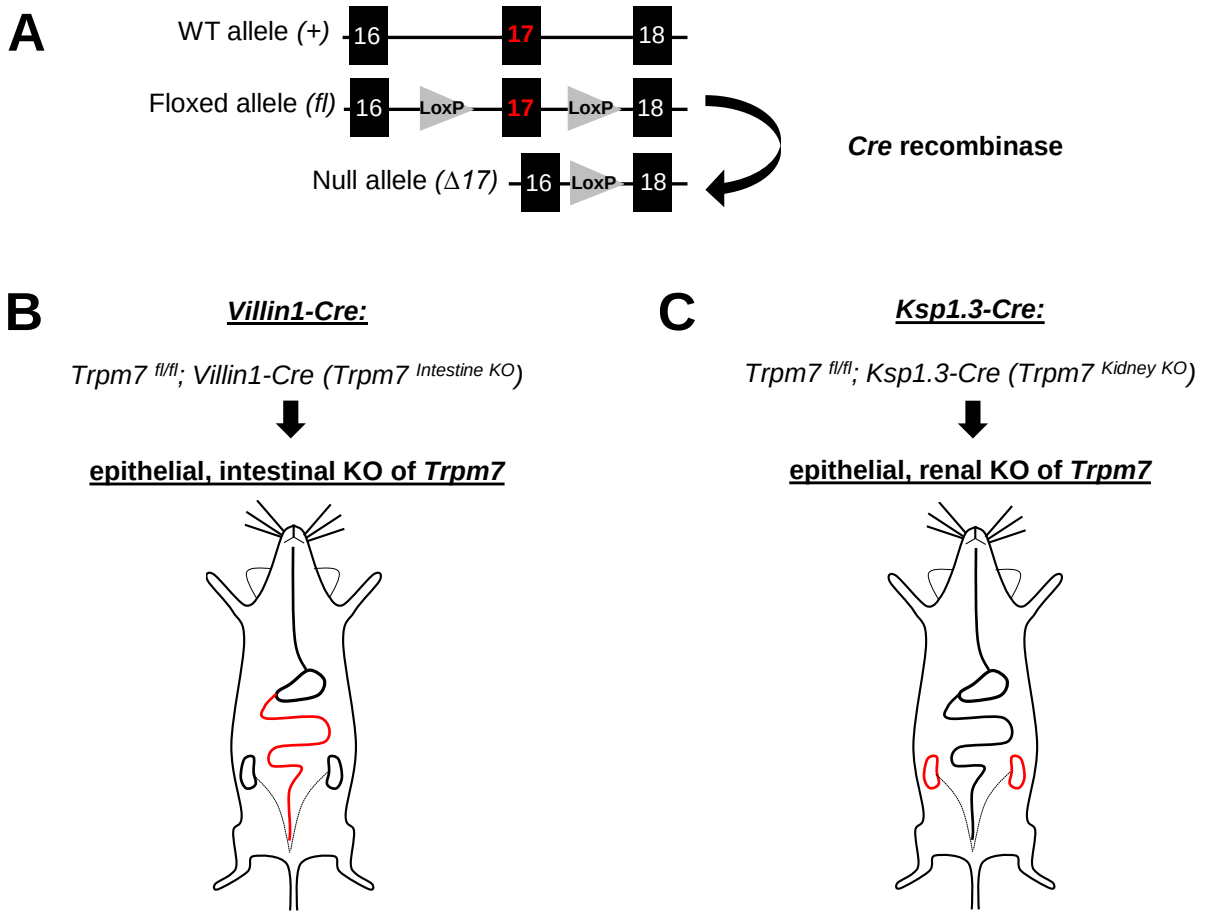

Figure 9: Genetic strategy used for a conditional inactivation of *Trpm7* in mice. (A) Exon 17 of *Trpm7* was flanked by two intronic LoxP sites. Deletion of exon 17 by a Cre recombinase results in a null allele [59]. **(B)** *Villin1-Cre* and **(C)** *Ksp1.3-Cre* transgenes enable to delete exon 17 in *Trpm7*, respectively, in epithelial cells of the intestine (B) and kidney (C).

To investigate the impact of TRPM7 kinase, we used a previously-established mouse strain carrying a 'kinase-dead' point mutation in the *Trpm7* gene resulting in complete inactivation of the kinase activity in the whole body (*Trpm7* $^{ki/ki}$ mice) [65]. Specifically, thymine (T) was replaced by cytosine (C) in exon 33 of *Trpm7* [65] (Figure 10). As a consequence, the mutant locus expresses TRPM7 containing the point mutation K1646R (Figure 10). K1646 is required for binding of ATP in a catalytic site of TRPM7 kinase domain. K1646R mutation does not interfere with the TRPM7 channel function but blocks completely phosphotransferase activity of the kinase domain [65].

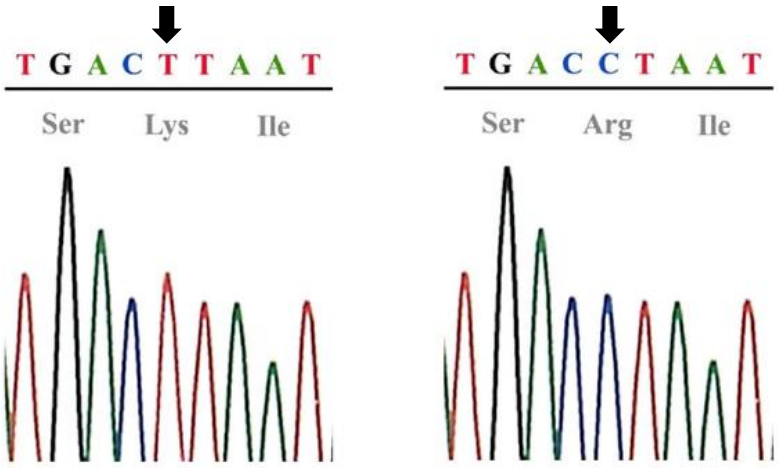

Figure 10: Sequencing of WT and 'kinase-dead' KI locus in *Trpm7*. A point mutation in the *Trpm7* gene exchanges thymine (T) to cytosine (C). Consequently, arginin (Arg) is introduced instead of lysin (Lys) in mouse TRPM7 (K1646R) (modified from Ryazanova et al., 2014 [66]).

6.3 Assessment of mice lacking TRPM7 in the kidney

To produce kidney-specific inactivation of TRPM7, we crossed *Trpm7* $^{fl/fl}$ and *Ksp1.3-Cre* transgenic mice. To verify genotypes of the offspring, we performed a PCR specific for the *Ksp1.3-Cre* transgene (Figure 11). To confirm that mice are homozygous for the *Trpm7* ^{fl} allele (Table 46), a PCR specific for the *Trpm7* ^{wt} allele was performed as outlined below (Figure 16).

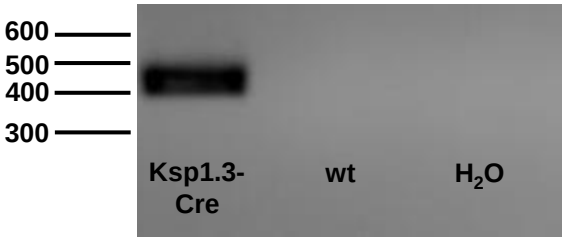

Figure 11: Genotyping of mice carrying the *Ksp1.3-Cre* transgene. Genomic DNA obtained from tail fragments of *Ksp1.3-Cre* transgenic mice was analyzed by PCR approach using primers specific for *Ksp1.3-Cre* sequence. The PCR amplicon (420 bp) was examined using agarose gel electrophoresis. H_2O and genomic DNA from wt mice were used to verify the specificity of the PCR.

Trpm7 $^{Kidney\ KO}$ mice were born in the expected Mendelian ratio (Table 46) and showed no obvious changes in growth, survival, fertility and physical appearance during 18 months of life (Figure 12).

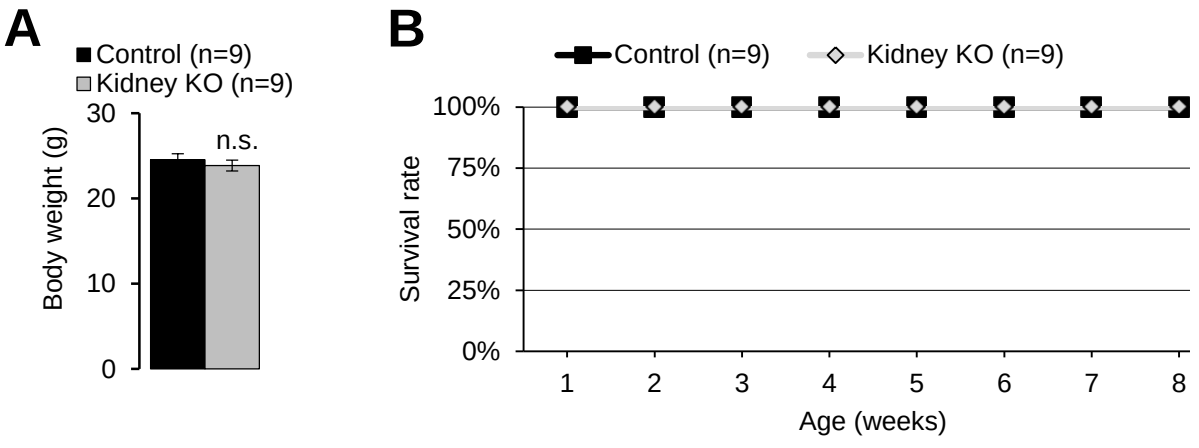

Figure 12: Body weight and survival rate of control and *Trpm7* $^{Kidney\ KO}$ mice. (A) Body weight of 8 weeks old control and *Trpm7* $^{Kidney\ KO}$ mice. **(B)** *Trpm7* $^{Kidney\ KO}$ mutation did not induce mortality in the mutant mice during 8 weeks of postnatal life. Values are mean ± SEM; n.s. - not significantly different (Student's t-test); n - number of mice.

To examine the expression of *Trpm7* in the kidney and to verify the deletion of the floxed sequence in *Trpm7* $^{Kidney\ KO}$ animals, we first tested a set of commercial and custom-made anti-TRPM7 antibodies. However, all reagents failed to detect TRPM7 protein in the kidney. Therefore, we used *in situ* hybridization. In line with previous studies [10, 142, 143], we could observe that *Trpm7* was abundantly expressed in tubule segments of control kidneys, characterized by apically located cell nuclei, a characteristic feature of DCT cells (Figure 13). Furthermore, *Trpm7* mRNA was not detectable in these epithelial cells in *Trpm7* $^{Kidney\ KO}$ animals indicating that deletion of *Trpm7* was efficient. Importantly, we did not observe morphological alterations in mutant kidneys, suggesting that morphogenesis was not affected in *Trpm7* $^{Kidney\ KO}$ mice (Figure 13).

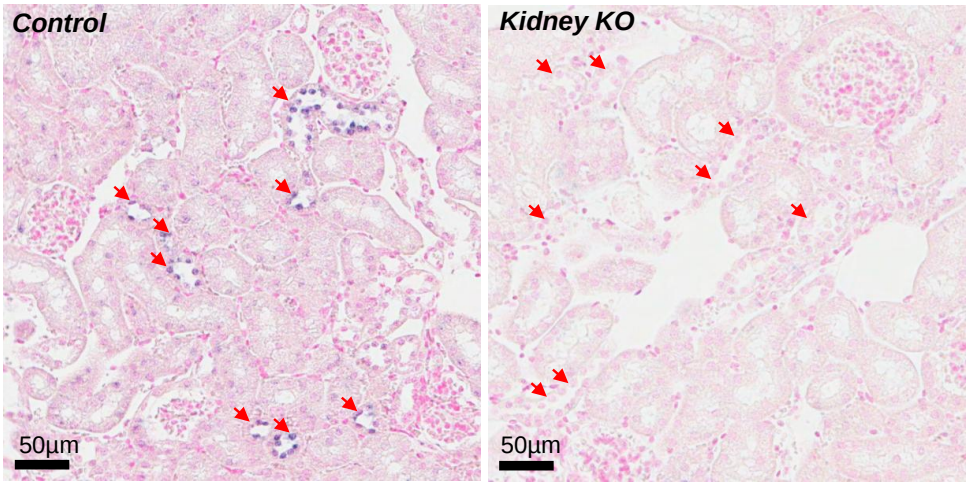

Figure 13: Detection of *Trpm7* transcripts in the kidney of control and *Trpm7* $^{Kidney\ KO}$ mice. Expression of *Trpm7* was examined using *in situ* hybridization (ISH) in kidney sections of 8 weeks old control and *Trpm7* $^{Kidney\ KO}$ mice. Expression of *Trpm7* was detected in nephron segments resembling distal convoluted tubule (DCT) in control mice (Control, red arrows). This *Trpm7* signal was absent in DCT in tissues of *Trpm7* $^{Kidney\ KO}$ mice (Kidney KO, red arrows). Representative images are shown (n=2 tissues per genotype).

Next, we asked whether the kidney-specific inactivation of TRPM7 can impact renal reabsorption of divalent cations. We collected urine and serum samples from 8 weeks old mice and examined these samples using ICP-MS. However, we found no changes in Ca^{2+}, Mg^{2+} and Zn^{2+} levels in urine or serum (Figure 14), suggesting that homeostasis of divalent cations was normal in *Trpm7* $^{Kidney\ KO}$ mice.

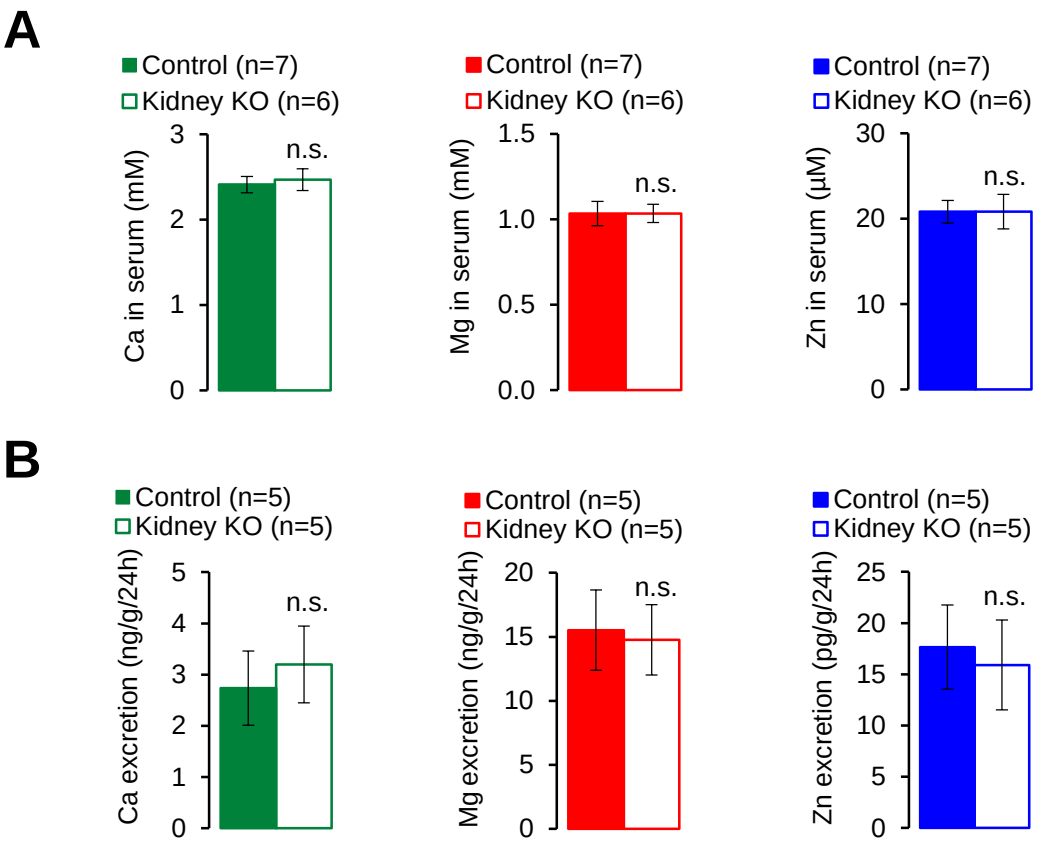

Figure 14: Assessment of elementary levels of divalent cations in serum and urine of control and *Trpm7* $^{Kidney\ KO}$ mice. Levels of Ca *(left panels)*, Mg *(middle panels)* and Zn *(right panels)* were examined in serum **(A)** and urine **(B)** in 8 weeks old control and *Trpm7* $^{Kidney\ KO}$ mice using ICP-MS. Values are shown as mean ± SEM; n.s. - not significantly different (Student's t-test); n - number of mice.

To elucidate whether TRPM7 function was compensated by other proteins, we analyzed genes which are thought to be involved in renal reabsorption of Mg^{2+} *(Claudin-16* and *Trpm6)* [144, 145], Ca^{2+} *(Trpv5)* [146] and Zn^{2+} *(ZnT1* and *ZnT2)* [147] using qRT-PCR. However, we did not observe differences in mRNA levels of these genes (Figure 15).

To summarize, *Trpm7* is highly expressed in the DCT segment of the kidney but the *Ksp1.3-Cre*-mediated inactivation of TRPM7 has no impact on the organismal balance of divalent cations.

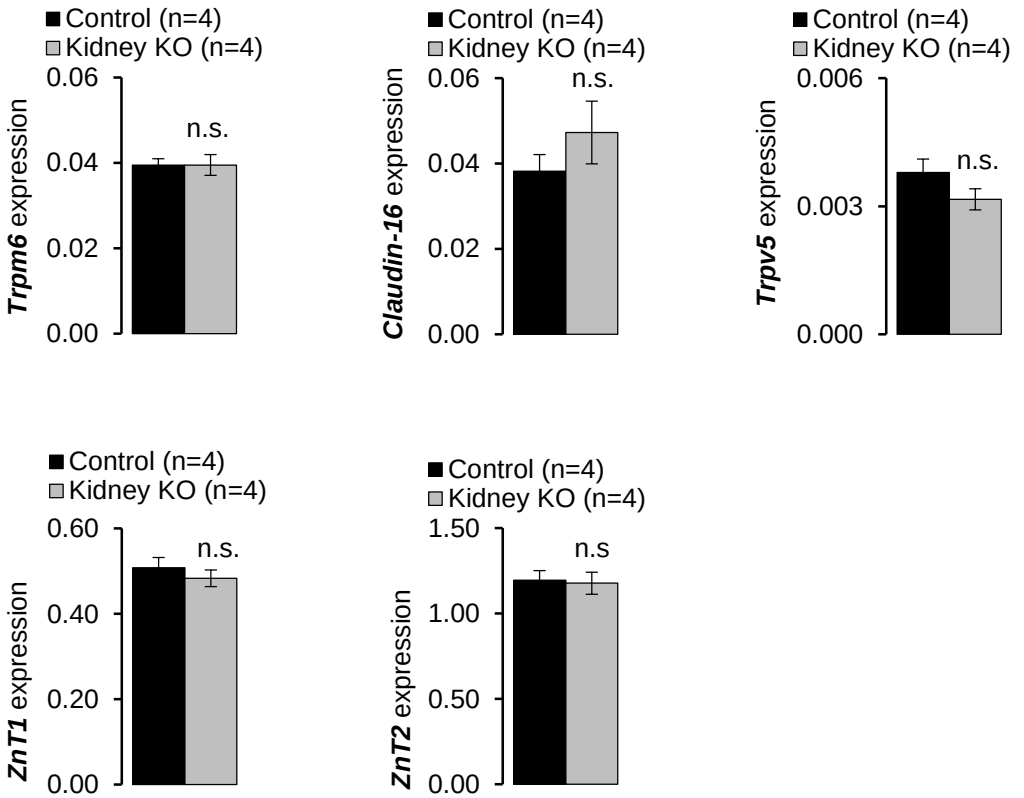

Figure 15: Expression of *Trpm6*, *Claudin-16*, *Trpv5*, *ZnT1* and *ZnT2* in the kidney of control and *Trpm7* $^{Kidney\ KO}$ mice. mRNA levels of *Trpm6*, *Claudin-16*, *Trpv5*, *ZnT1* and *ZnT2* in kidneys of control and *Trpm7* $^{Kidney\ KO}$ mice were measured using qRT-PCR and *Ywhaz* as the reference gene. Values are mean ± SEM; n.s. - not significantly different (Student's t-test); n - number of mice.

6.4 Examination of mice lacking TRPM7 in the intestine

6.4.1 Genetic and phenotypical assessment of *Trpm7* $^{Intestine\ KO}$ mice

To produce mice carrying an intestinal-specific inactivation of TRPM7, we crossed *Trpm7* $^{fl/fl}$ and *Villin1-Cre* transgenic mice. To verify genotypes of the offspring, we performed a set of PCRs specific for *Villin1-Cre* transgene, as well as for wt and floxed *Trpm7* alleles (Table 46) (Figure 16).

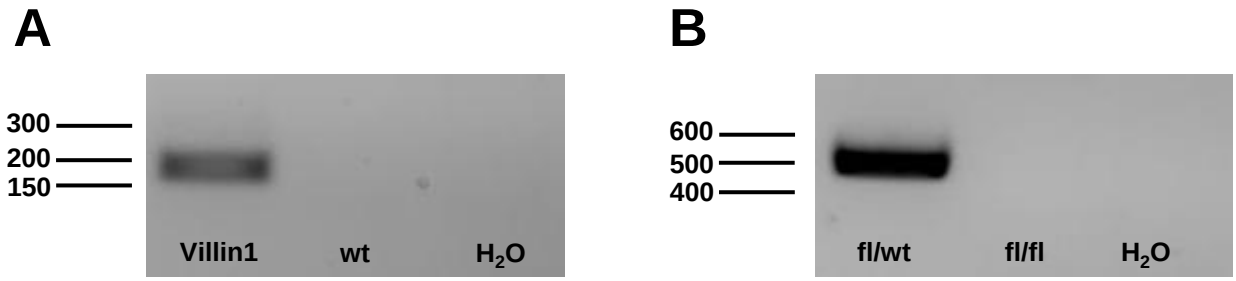

Figure 16: Genotyping of *Villin1-Cre*, *Trpm7* $^{fl/wt}$ and *Trpm7* $^{fl/fl}$ transgenic mice. (A, B) Genomic DNA obtained from tail fragments of *Villin1-Cre*, *Trpm7* $^{fl/wt}$ and *Trpm7* $^{fl/fl}$ transgenic mice was analyzed by PCR approach using primers specific for *Villin1-Cre* and *Trpm7* ^{wt} sequence. The PCR amplicons (195 bp for *Villin1-Cre* (A) and 530 bp for *Trpm7* ^{wt} (B)) were examined using agarose gel electrophoresis. H_2O and genomic DNA from wt and fl mice were used to verify the specificity of the PCR.

Trpm7 $^{Intestine\ KO}$ mice were born in the expected Mendelian ratio (Table 46). At the day of birth (postnatal day 1, P1), *Trpm7* $^{Intestine\ KO}$ mice displayed a normal body weight and overall physical appearance as compared to control littermates (Figure 17 A, C). At P3 and P5, the mutants were growth delayed (respectively, 12% and 45%) (Figure 17 B, C). Furthermore, P3–5 *Trpm7* $^{Intestine\ KO}$ mice showed a high mortality rate and all *Trpm7* $^{Intestine\ KO}$ individuals have died after P10 (Figure 17 D). Importantly, stomachs of P1–10 *Trpm7* $^{Intestine\ KO}$ mice were filled with milk, a sign for normal feeding behavior.

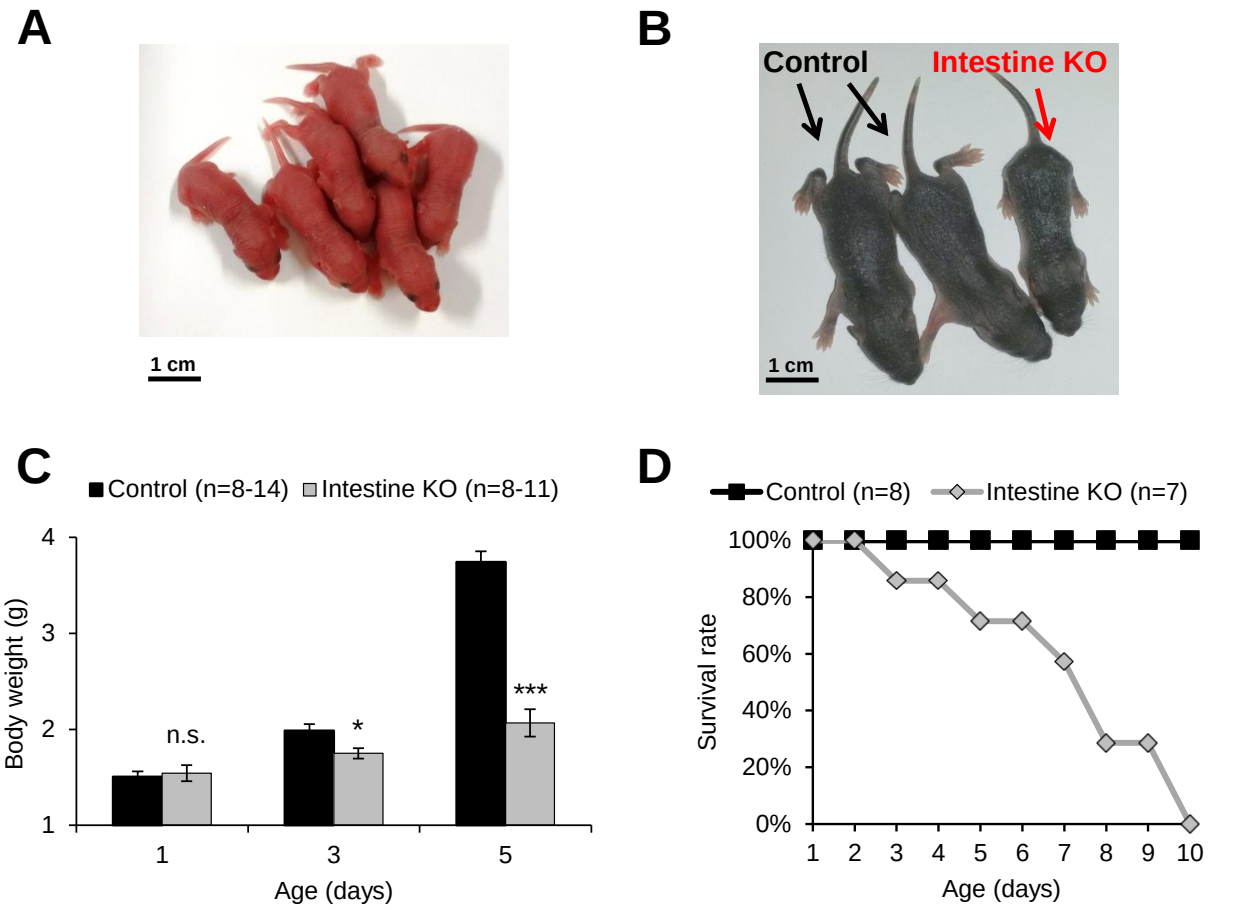

Figure 17: Physical appearance of control and *Trpm7* $^{Intestine\ KO}$ mice. *Trpm7* $^{Intestine\ KO}$ mice were not distinguishable from control littermates at postnatal day 1 (P1) **(A)**, whereas growth retardation was observed in the mutant pups at P5 **(B)**. Body weight (mean ± SEM) **(C)** and survival rate **(D)** of control and *Trpm7* $^{Intestine\ KO}$ mice. *** - P≤0.001, * - P≤0.05, n.s. - not significantly different (Student's t-test); n - number of mice.

It was shown that an early embryonic inactivation of *Trpm7* affects morphogenesis of several organs [59, 61, 62, 148]. Therefore, we asked whether villi of *Trpm7* $^{Intestine\ KO}$ mice were normally developed. We isolated villi from the whole intestine of P5 littermates and examined them using a microscope. Villi isolated from *Trpm7* $^{Intestine\ KO}$ mice showed no obvious morphological alterations (Figure 18). Next, we isolated villi RNA and examined the expression of *Villin1*, a marker of differentiated intestinal enterocytes [134]. We found no changes in relative expression levels of *Villin1* (Figure 19).

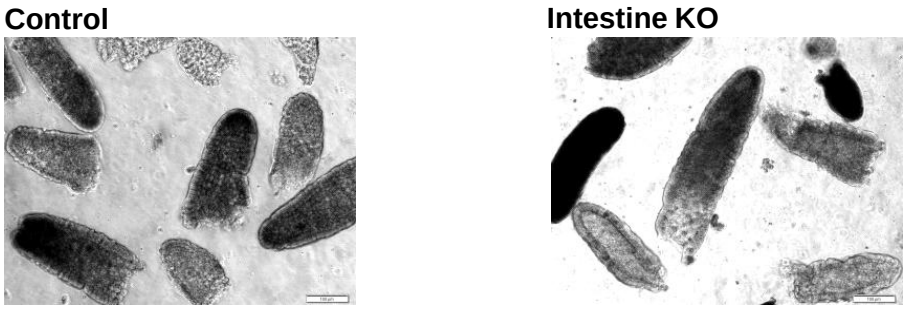

Figure 18: Representative images of purified villi isolated from control and *Trpm7* $^{Intestine\ KO}$ mice.

To verify the efficiency of recombination in the *Trpm7* ^{fl} allele, we assessed the villi RNA samples using qRT-PCR specific for WT *Trpm7* transcripts. WT *Trpm7* transcripts were nearly undetectable in the villi from *Trpm7* $^{Intestine\ KO}$ mice (Figure 19), suggesting that *Villin1-Cre* was highly efficient in mutagenesis of *Trpm7* ^{fl}.

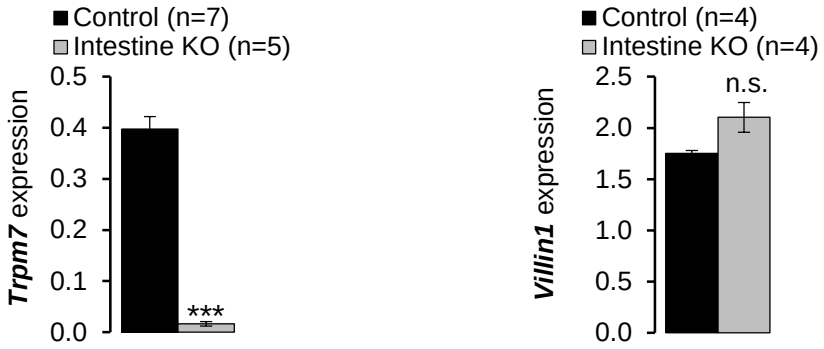

Figure 19: Relative expression levels of *Trpm7* and *Villin1* in the villi of control and *Trpm7* $^{Intestine\ KO}$ mice. mRNA expression of *Trpm7* (left) and *Villin1* (right) was analyzed using qRT-PCR and *Hprt* as a reference transcript. Values are shown as mean ± SEM; *** - P≤0.001, n.s. - not significantly different (Student's t-test); n - number of mice.

The deletion of TRPM7 in the intestinal enterocytes of *Trpm7* $^{Intestine\ KO}$ mice was further verified by immunofluorescence staining with TRPM7-specific antibody of duodenal sections (Figure 20). We observed a staining of the apical surface of villus cells in tissues isolated from 8 weeks old control mice. However, the signal was significantly reduced in tissues from P5 control mice, suggesting that expression levels of TRPM7 are lower in newborn mice as compared to adult animals (Figure 20). Importantly, in line with qRT-PCR data (Figure 19), villus epithelial cells in tissues from P5 *Trpm7* $^{Intestine\ KO}$ mice were not labeled (Figure 20), confirming the successful deletion of TRPM7 in the intestinal enterocytes of *Trpm7* $^{Intestine\ KO}$ mice.

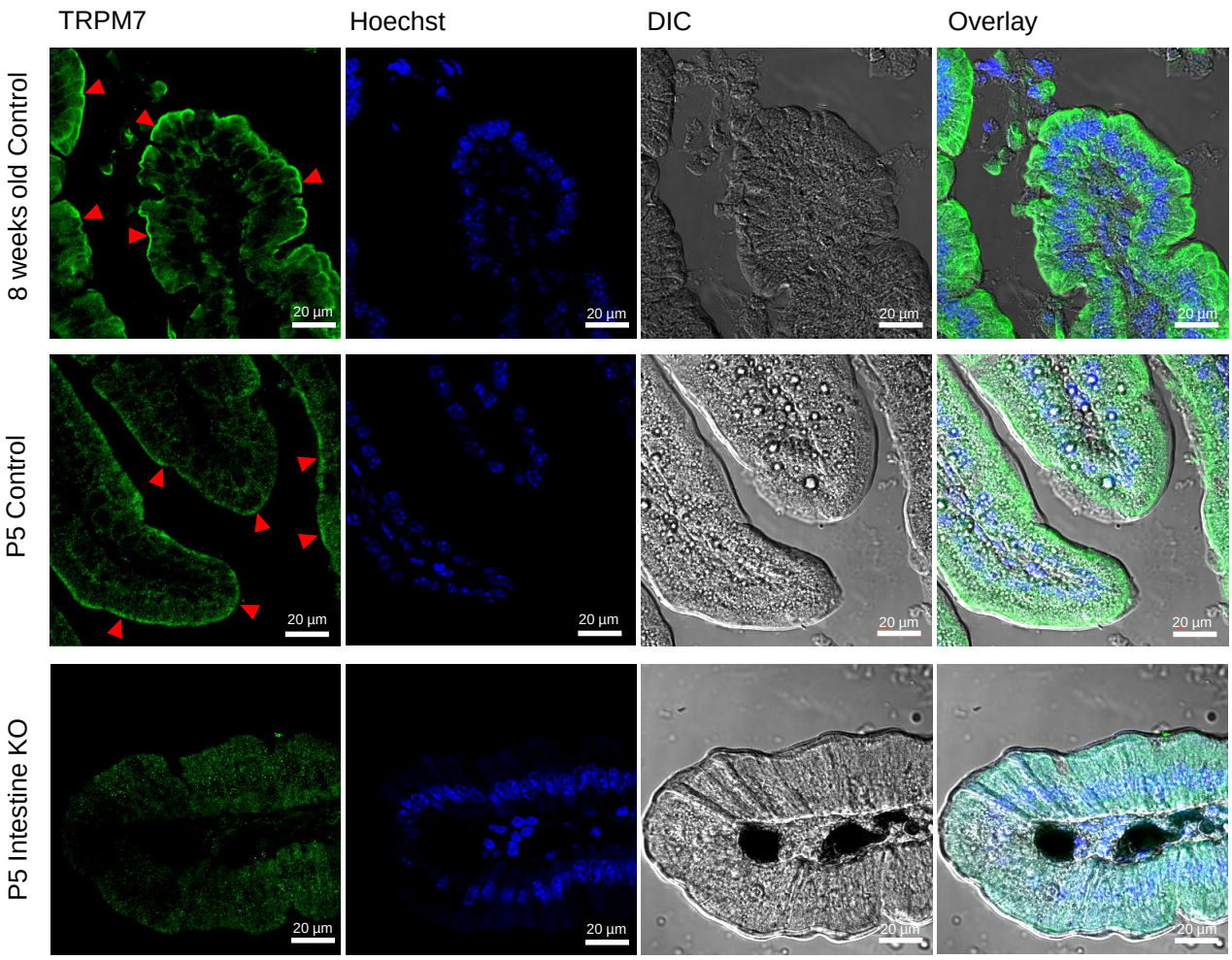

Figure 20: Staining of duodenum sections using a TRPM7-specific antibody. TRPM7 immunoreactivity (TRPM7), Hoechst staining (Hoechst) and differential interference contrast images (DIC) are shown. Tissue sections were obtained from duodenums of 8 weeks old or P5 control and P5 *Trpm7* $^{Intestine\ KO}$ mice. Triangles show labeling of the apical surface of enterocytes, which was observed in control tissues only. Representative images are shown (n = 2 tissues per genotype).

To get insights whether tissue homeostasis was affected in the intestine of *Trpm7* $^{Intestine\ KO}$ mice, we investigated the duodenum of P5 mutant and control littermates (duodenum is thought to be very active in nutritional intake of Ca^{2+} and Zn^{2+} [93, 119-121]). We extracted RNA from the whole duodenum and investigated relative expression levels of different markers. We found no changes in expression levels of *Villin1*, *Dclk1*, *Lgr5 and Muc2*, markers of enterocytes, tuft cells, intestinal stem cells and goblet cells (Figure 21). In contrast, expression of *Lyz1*, a marker for Paneth cells [149], was elevated 3.65 times (Figure 21).

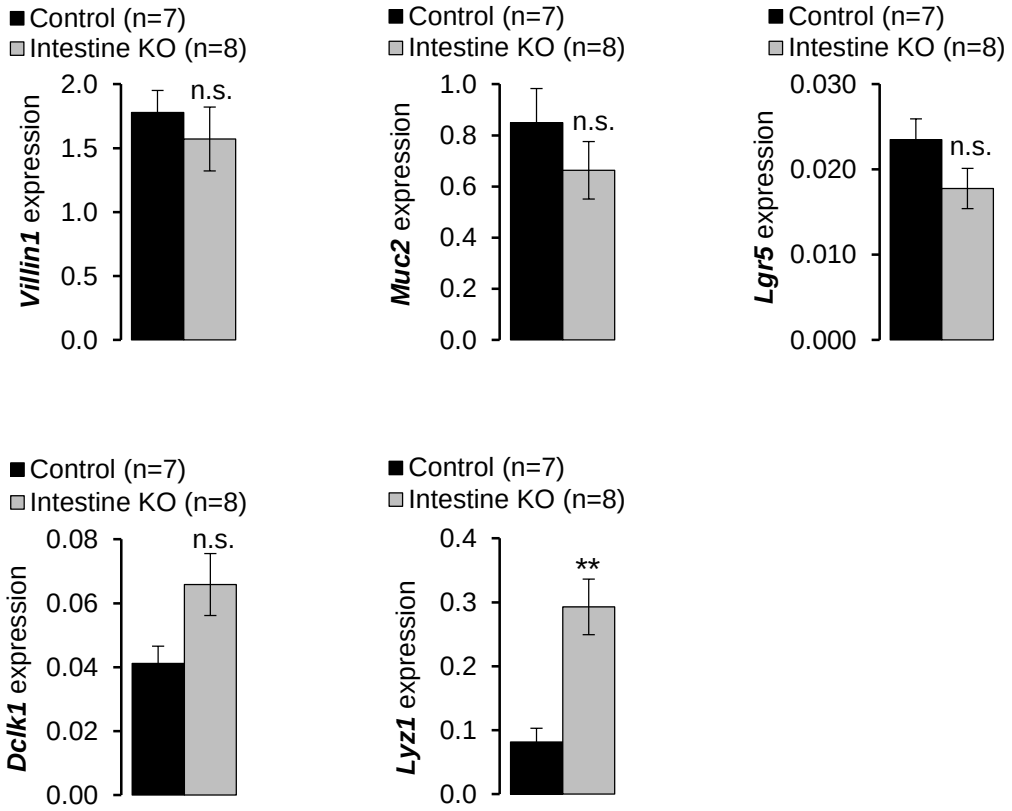

Figure 21: Relative expression levels of cell-type markers in the intestine of control and *Trpm7* $^{Intestine\ KO}$ mice. mRNA levels of *Villin1* (enterocytes), *Muc2* (goblet cells), *Lgr5* (intestinal stem cells), *Dclk1* (tuft cells) and *Lyz1* (Paneth cells) were analyzed in the duodenum of P5 animals using qRT-PCR and *Hprt* as a reference transcript. Values are shown as mean ± SEM; ** - P≤0.01, n.s. - not significantly different (Student's t-test); n - number of mice.

Finally, we performed a histological examination of the small and large intestine of *Trpm7* $^{Intestine\ KO}$ individuals at P1. Examination of hematoxylin and eosin (H&E) stained tissue sections did not reveal systemic abnormalities with regard to gross anatomy and overall mucosal architecture indicating unaffected intestinal organogenesis. However, we observed some duodenal erosions and vacuolization of epithelial crypt cells of the jejunum (Figure 22) resembling the phenotype of *Trpm7*-deficient vacuole-rich megakaryocytes [63]. In addition, vacuolization of cells was observed in the enterocytes of rodents maintained on a Zn^{2+}-deficient diet [150, 151]. Taken together, our results suggest that the conditional mutagenesis of *Trpm7* in intestinal enterocytes didn't affect the embryonic morphogenesis of the intestine.

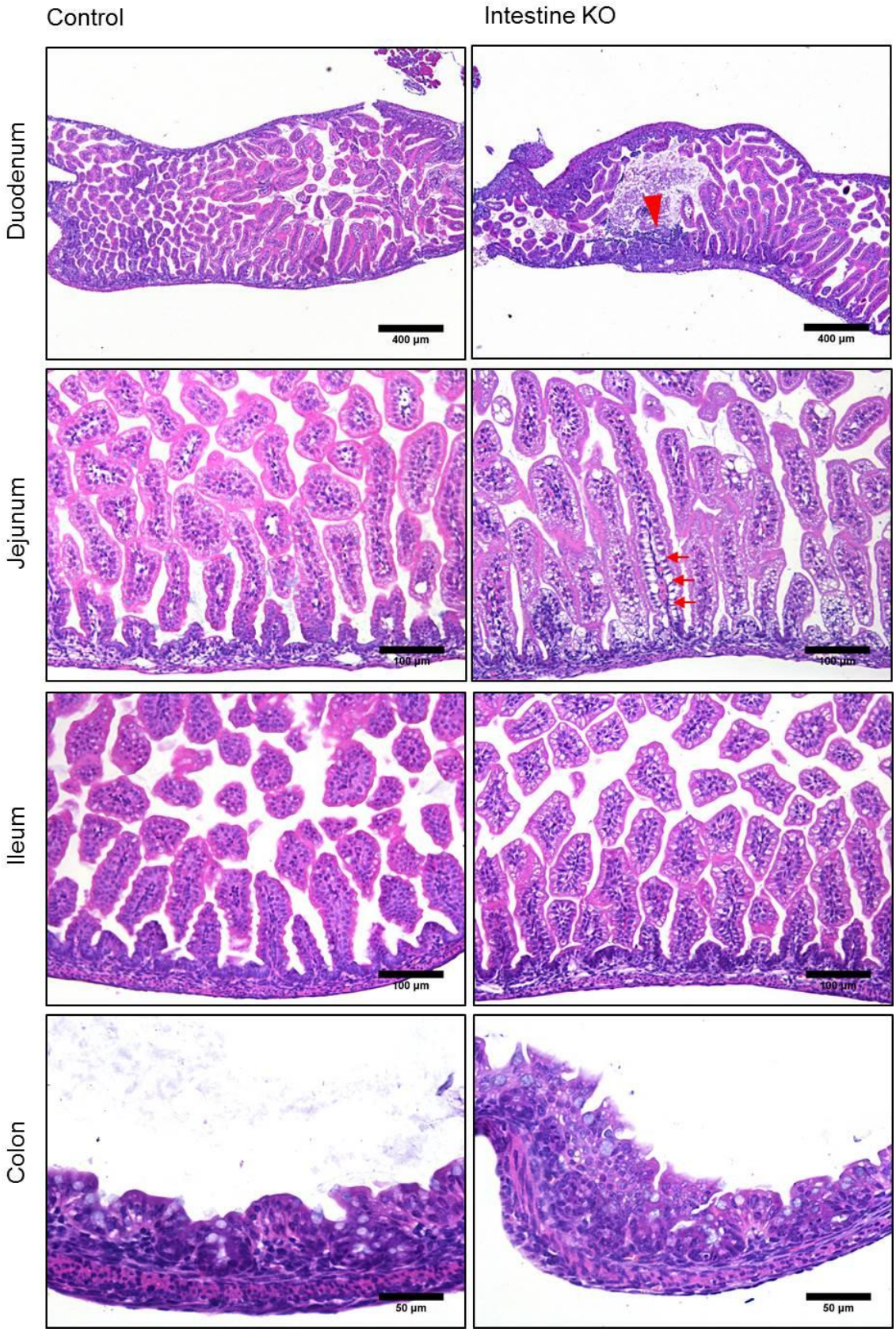

Figure 22: Histological examination of the intestine of control and *Trpm7* $^{Intestine\ KO}$ mice. Hematoxylin and eosin (H&E) staining of paraffin-embedded tissue sections (duodenum, jejunum, ileum and colon) of P1 control and *Trpm7* $^{Intestine\ KO}$ littermates. Representative images are shown (n=3 tissues per genotype). The triangle points at duodenal erosion observed in the duodenum of *Trpm7* $^{Intestine\ KO}$ mice. Arrows indicate vacuolization of cells in the jejunum of *Trpm7* $^{Intestine\ KO}$ mice.

6.4.2 Assessment of divalent cation homeostasis in mice lacking intestinal TRPM7

We asked whether the ablation of TRPM7 in *Trpm7* $^{Intestine\ KO}$ pups could trigger malabsorption of divalent cations. We used ICP-MS to analyze levels of main minerals in serum and bones (right tibia) of *Trpm7* $^{Intestine\ KO}$ pups prior to (P1) or at the onset (P3, P5) of macroscopic phenotypes (Figure 17). We found no changes in concentrations of Ca, Mg or Zn in P1 *Trpm7* $^{Intestine\ KO}$ mice (Figure 23). Interestingly, in the follow-up period, *Trpm7* $^{Intestine\ KO}$ mice developed deficiencies of divalent cations. At P3 we observed that Mg levels were not changed, but at P5 we found a statistically significant reduction of Mg content (22%) in serum as compared to control values (Figure 23 A). However, Mg levels of bones at P3 and P5 were normal, indicating that the *Trpm7* $^{Intestine\ KO}$ mice developed a rather moderate Mg^{2+} deficiency at P5 (Figure 23 B). In contrary, Ca homeostasis was stronger affected since a significant reduction of Ca concentration in the serum (14%) of *Trpm7* $^{Intestine\ KO}$ mice was observed already at P3, which was more pronounced at P5 (36%) (Figure 23 A). In line with these alterations, only P5 *Trpm7* $^{Intestine\ KO}$ mice displayed a significant depletion (19%) of Ca in bones (Figure 23 B). Notably, Zn homeostasis was most strongly affected in *Trpm7* $^{Intestine\ KO}$ pups. Serum Zn concentrations were 21% and 61% decreased in *Trpm7* $^{Intestine\ KO}$ pups at P3 and P5, respectively (Figure 23 A). In bones, Zn concentrations were not affected in P3 *Trpm7* $^{Intestine\ KO}$ mice, however, Zn content was lower (18%) in P5 mutants (Figure 23 B).

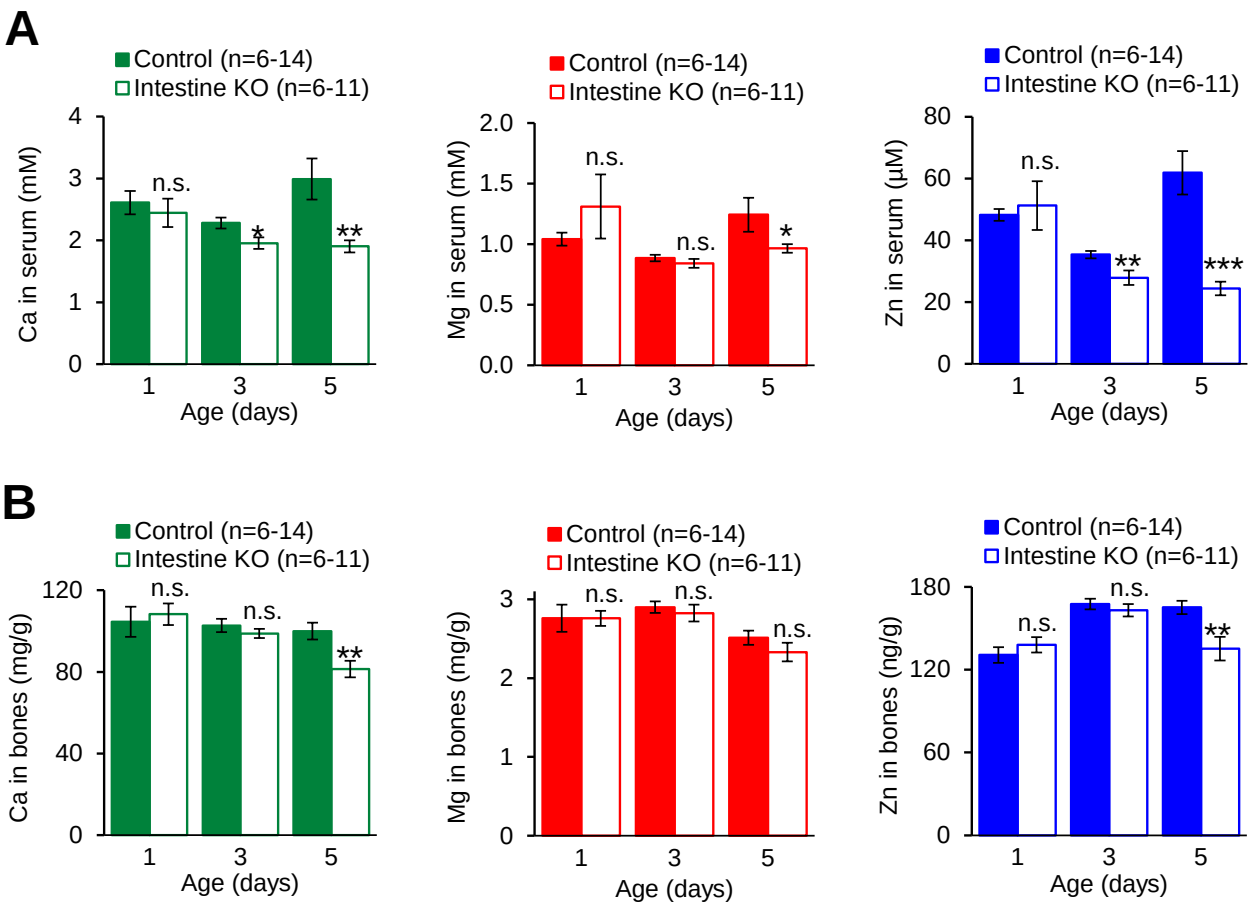

Figure 23: Assessment of elementary levels of divalent cations in control and *Trpm7* $^{Intestine\ KO}$ mice. ICP-MS analysis of elementary levels of Ca *(left panels)*, Mg *(middle panels)* and Zn *(right panels)* in serum **(A)** and bones (right tibia) **(B)** of P1, P3 and P5 control and *Trpm7* $^{Intestine\ KO}$ littermates. Results are shown as mean ± SEM; *** - P≤0.001, ** - P≤0.01, * - P≤0.05, n.s. - not significantly different (Student's t-test); n - number of mice.

Importantly, concentrations of monovalent cations such as sodium (Na) and potassium (K) were not altered, neither in bones nor in serum of P1–5 *Trpm7* $^{Intestine\ KO}$ pups (Figure 24), except a slight elevation (24%) of Na levels in bones of P5 mutants. These results indicate that the lack of TRPM7 in the intestine caused only a defect in the uptake of divalent cations.

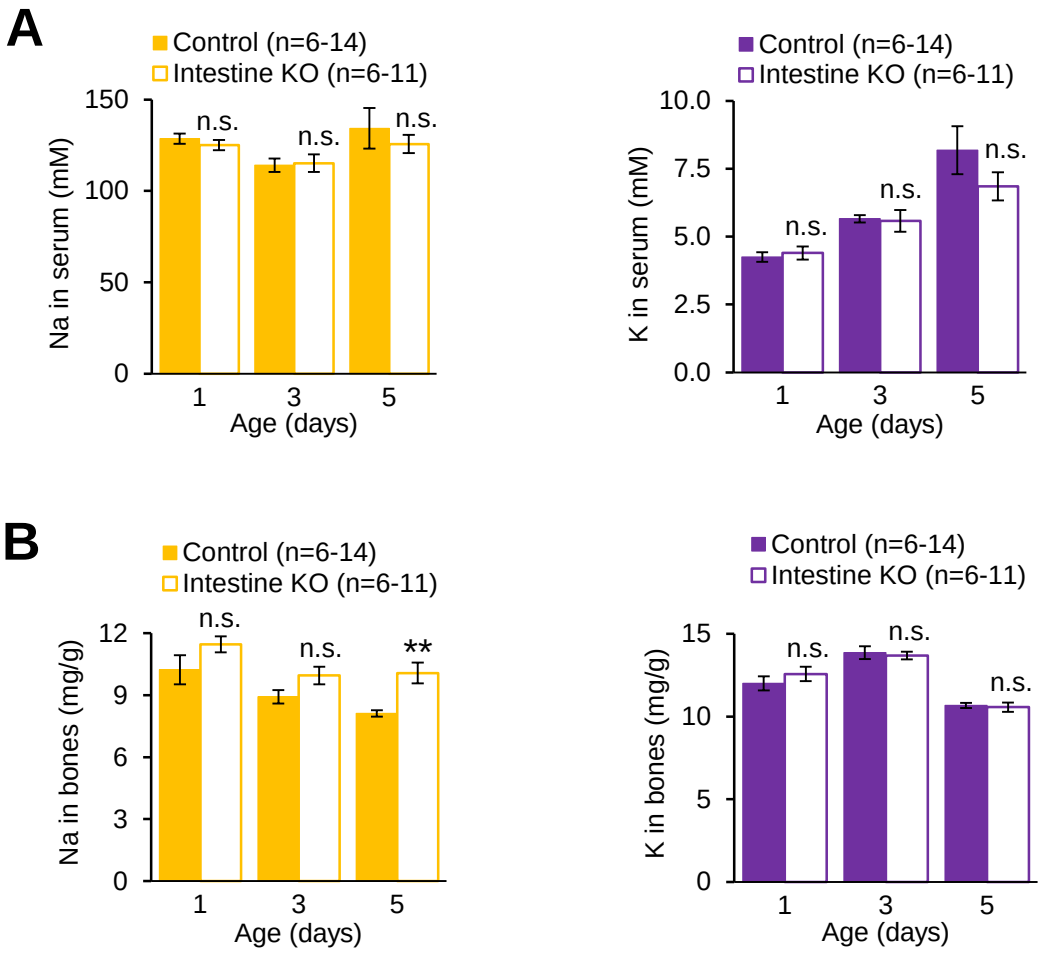

Figure 24: Elementary levels of monovalent cations in control and *Trpm7* $^{Intestine\ KO}$ mice. ICP-MS analysis of elementary levels of Na *(left panels)* and K *(right panels)* in serum **(A)** and bones (right tibia) **(B)** of P1, P3 and P5 control and *Trpm7* $^{Intestine\ KO}$ littermates. Values are mean ± SEM; ** - P≤0.01, n.s. - not significantly different (Student's t-test); n - number of mice.

6.4.3 Evaluation of organismal adaptive response of *Trpm7* $^{Intestine\ KO}$ mice

Since we have found reduced Ca levels in serum and bones of *Trpm7* $^{Intestine\ KO}$ mice, we asked whether this deficiency triggered an organismal adaptive response. Parathyroid hormone (PTH) and calcitriol (1,25-$(OH)_2D_3$) are two important regulators of Ca^{2+} homeostasis [152, 153]. It is well documented that a release of PTH and 1,25-$(OH)_2D_3$ is enhanced by low serum Ca^{2+} [152, 153]. To examine whether serum PTH and 1,25-$(OH)_2D_3$ levels were increased in *Trpm7* $^{Intestine\ KO}$ mice we used an ELISA. As expected, *Trpm7* $^{Intestine\ KO}$ mice displayed increased circulating levels of PTH (18.2-fold, Figure 25 A) and calcitriol (1,25-$(OH)_2D_3$) (9.4-fold, Figure 25 B).

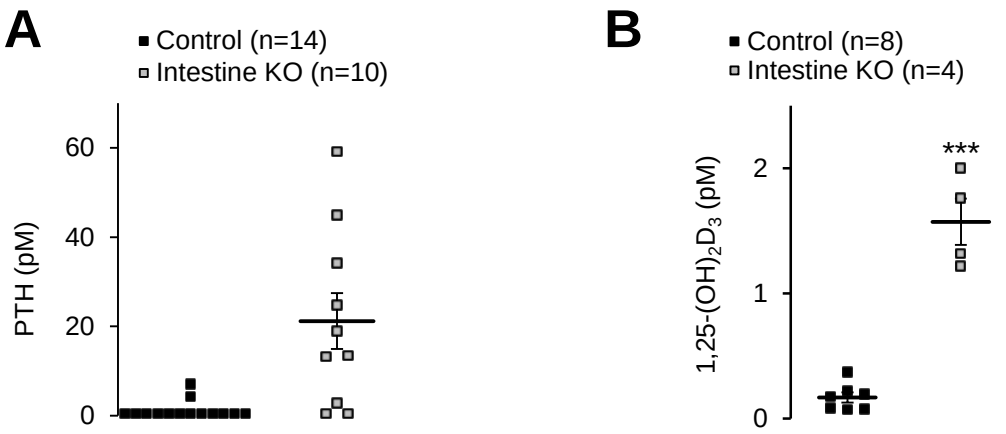

Figure 25: Parathyroid hormone (PTH) and calcitriol (1,25-$(OH)_2D_3$) levels in serum of control and *Trpm7* $^{Intestine\ KO}$ mice. The concentration of PTH **(A)** and calcitriol (1,25-$(OH)_2D_3$) **(B)** in serum of P5 control and *Trpm7* $^{Intestine\ KO}$ animals were measured using an ELISA. (A) Note: only two samples from *Trpm7* $^{Intestine\ KO}$ mice were above the assay sensitivity level of the PTH ELISA (0.425 pM) and statistical analysis could not be performed. (B) The results are shown as mean ± SEM; *** - P≤0.001 (Student's t-test); n - number of mice.

It is known that PTH increases the activity of cytochrome P450 27b1 (*Cyp27b1*), the enzyme of the kidney controlling hydroxylation of inactive calcifediol (inactive form of vitamin D) to calcitriol (active form of vitamin D). Therefore, we studied whether *Cyp27b1* expression in the kidney was changed in *Trpm7* $^{Intestine\ KO}$ mice. As expected, *Cyp27b1* mRNA was strongly upregulated (32.4-fold, Figure 26 A). It was suggested that calcitriol increases the uptake of Ca^{2+} by the gastrointestinal tract due to upregulation of the Ca^{2+} selective channel Trpv6 and Ca^{2+}-binding protein Calbindin-D9k. We found that expression levels of *Trpv6* and *Calbindin-D9k* were significantly upregulated in the duodenum of *Trpm7* $^{Intestine\ KO}$ mice, 7.4-fold and 4.1-fold respectively (Figure 26 B).

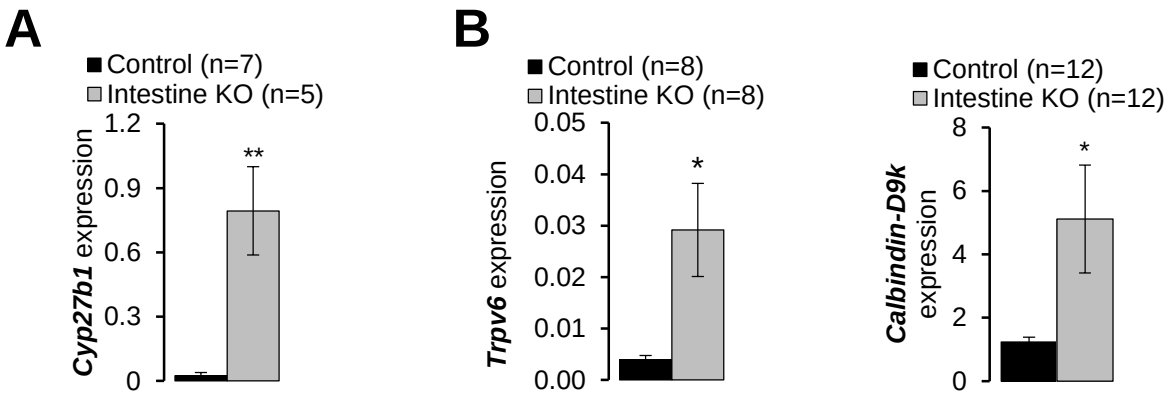

Figure 26: Evaluation of intestinal expression of Ca related genes in control and *Trpm7* $^{Intestine\ KO}$ mice. mRNA levels of *Cyp27b1* in the kidney **(A)** and *Trpv6* and *Calbindin-D9k* in the duodenum **(B)** of P5 animals were analyzed using qRT-PCR and *Hprt* as a reference transcript. Values are shown as mean ± SEM; ** - P≤0.01, * - P≤0.05 (Student's t-test); n - number of mice.

Thus, *Trpm7* $^{Intestine\ KO}$ mice displayed a remarkable adaptive response secondary to Ca^{2+} deficiency.

Organismal response to Mg^{2+} or Zn^{2+} deficiency remains poorly understood. A previous study has shown that *Trpm6* controls intestinal Mg^{2+} uptake [44]. Accordingly, *Trpm6 KO* mice develop systemic Mg^{2+} deficiency [44] accompanied by low circulating levels of insulin-like growth factor 1 (IGF1). Therefore, we assessed the expression of *Trpm6* in the duodenum of P5 *Trpm7* $^{Intestine\ KO}$ mice and found that *Trpm6* mRNA levels were 30.0-fold increased (Figure 27). Additionally, two putative intestinal Mg^{2+} transporters, *Slc41a1* and *Slc41a2,* were upregulated (113% and 94%, respectively) (Figure 27).

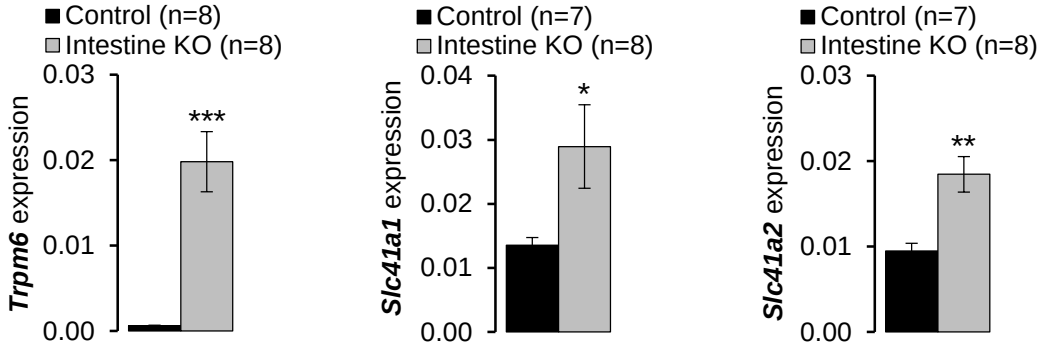

Figure 27: Intestinal expression of genes related to Mg homeostasis in control and *Trpm7* $^{Intestine\ KO}$ mice. mRNA levels of *Trpm6*, *Slc41a1* and *Slc41a2* were analyzed in the duodenum of P5 animals using qRT-PCR and *Hprt* as a reference transcript. Values are shown as mean ± SEM; *** - P≤0.001, ** - P≤0.01, * - P≤0.05 (Student's t-test); n - number of mice.

In addition, we found that serum IGF1 concentration was substantially lower (70%) in *Trpm7* $^{Intestine\ KO}$ mice at P5 using an ELISA (Figure 28 A). Thyroxine (T_4) was suggested to be linked to a thyroid gland response to low levels of Zn^{2+} in the body [154]. Therefore, we investigated serum T_4 levels in P5 littermates using ELISA and found that *Trpm7* $^{Intestine\ KO}$ pups developed hypothyroidism: T4 concentration was 55% reduced (Figure 28 B).

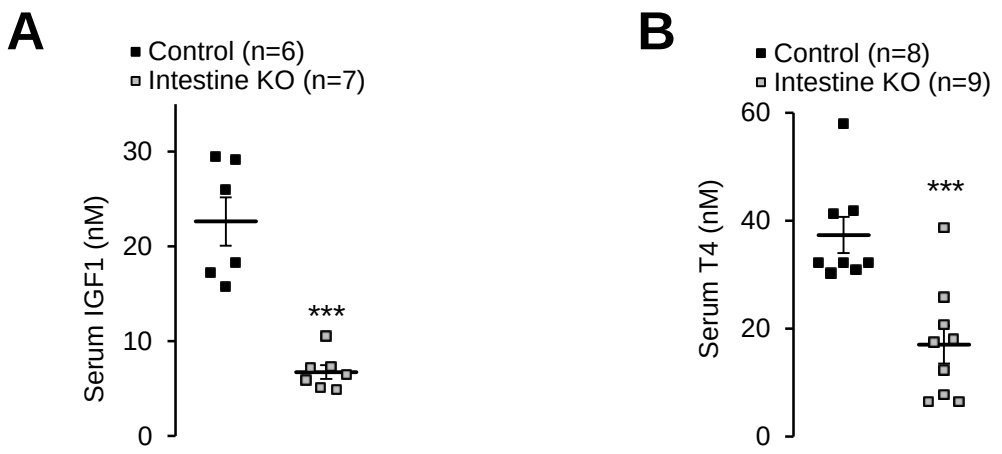

Figure 28: Insulin-like growth factor 1 (IGF1) and thyroxine (T_4) levels in serum of control and *Trpm7* $^{Intestine\ KO}$ mice. The concentration of insulin-like growth factor 1 (IGF1) **(A)** and Thyroxine (T_4) **(B)** in serum of P5 control and *Trpm7* $^{Intestine\ KO}$ animals was measured using an ELISA. The results are shown as mean ± SEM; *** - P≤0.001 (Student's t-test); n - number of mice.

Next, we asked whether mRNA levels of Zn^{2+}-inducible genes were changed. Since the duodenum is regarded as the main site for intestinal uptake of Zn^{2+} [119-121], we isolated RNA from the whole duodenum, and examined relative expression levels of known Zn^{2+} transporters from the *Slc30* and the *Slc39* gene families as well as metallothionein (*MT1*), the main intracellular scavenger of Zn^{2+} ions. mRNA levels of *ZnT1*, *ZnT2*, *Zip4* and *Zip5* were significantly downregulated, whereas *MT1* was upregulated and ZnT4 unchanged in *Trpm7* $^{Intestine\ KO}$ mice. Taken together, the epithelial transport of Zn^{2+}, Mg^{2+} and Ca^{2+} is profoundly dysregulated in *Trpm7* $^{Intestine\ KO}$ mice followed by induction of a strong organismal response.

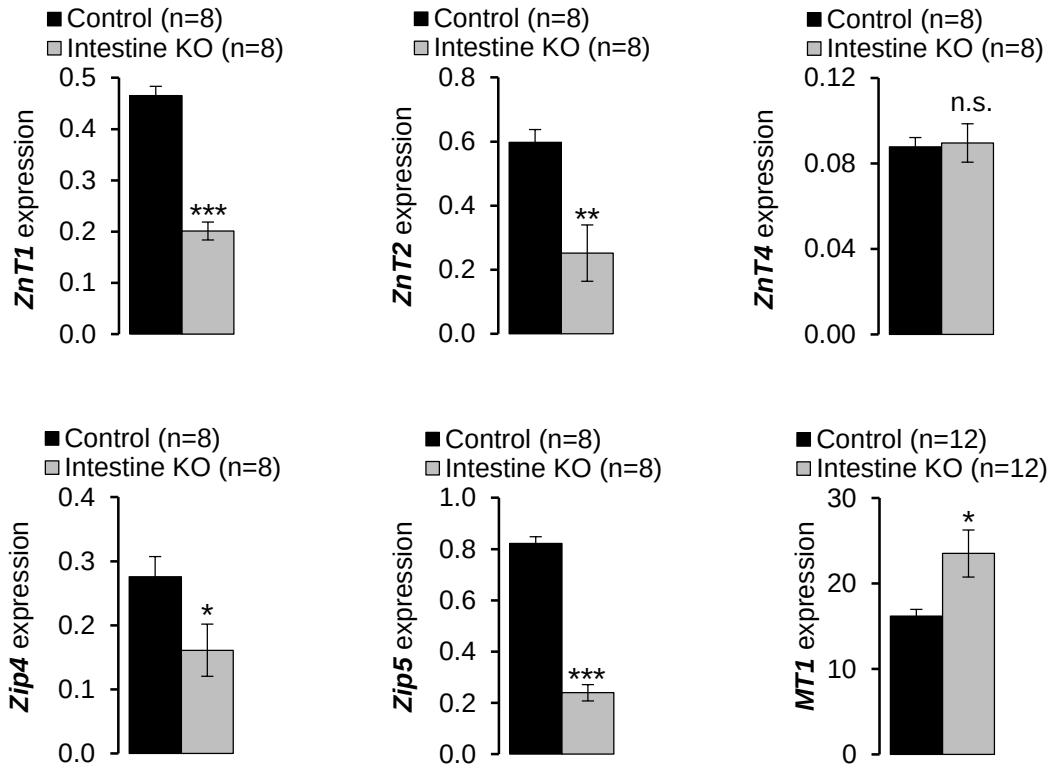

Figure 29: Relative expression levels of Zn transporters and MT1 in the intestine of control and *Trpm7* $^{Intestine\ KO}$ mice. mRNA levels of *ZnT1*, *ZnT2*, *ZnT4*, *Zip4*, *Zip5* and *MT1* in the duodenum were measured using qRT-PCR and *Hprt* as a reference transcript. The results are shown as mean ± SEM; *** - P≤0.001, ** - P≤0.01, * - P≤0.05, n.s. - not significantly different (Student's t-test); n - number of mice.

6.4.4. Supplementation of *Trpm7* $^{Intestine\ KO}$ mice with high doses of Mg^{2+}, Ca^{2+} and Zn^{2+}

Mg^{2+}- and Ca^{2+}-rich diets were found to be affective in counteracting the deficiency of Mg^{2+} and Ca^{2+} in adult mice [42, 44, 86, 115]. We investigated whether the high mortality of newborn *Trpm7* $^{Intestine\ KO}$ mice can be ameliorated by dietary supplementation of Ca^{2+}, Mg^{2+} or Zn^{2+}. Since newborn pups are breastfed for the first 3 weeks of postnatal life, the breeding females were treated with the different diets during pregnancy and breastfeeding of the offspring (Table 63).
Specifically, we used chows with 2% Ca^{2+} (1% in the normal diet) or with 0.75% Mg^{2+} (0.22% in the normal diet). For Zn^{2+} supplementation, we dissolved $ZnSO_4$ * 7 H_2O in deionized water (dH_2O) (0.1%), since this strategy was used before to rescue Zn^{2+} deficient animals [155]. The "high Zn diet" and the untreated KO group received the regular Ssniff M-Z as chow (Table 63).

Table 63: Dietary treatments used in survival experiments

Group	Chow	Drinking water
Control diet	Regular chow	dH_2O
High Mg diet	High Mg^{2+} chow	dH_2O
High Ca diet	High Ca^{2+} chow	dH_2O
High Zn diet	Regular chow	dH_2O + 0.1% Zn^{2+}
Triple diet (high Mg, Ca and Zn)	High Ca^{2+}/Mg^{2+} chow	dH_2O + 0.1% Zn^{2+}

We determined the survival rates of *Trpm7* $^{Intestine\ KO}$ mice in the untreated and supplemented groups. None of the *Trpm7* $^{Intestine\ KO}$ pups from the untreated group could survive after P14 (Figure 30). Although animals of the “high Ca diet” had a 3-day delay in the onset of mortality, the lifespan was not significantly increased (P=0.31) in this group (Figure 30 A). Interestingly, the survival curve of the “high Zn diet” group was rightward shifted (P < 0.0001). Remarkably, at P7 only 18% of mutant pups were dead in this group *vs* 69% in the untreated group. Two *Trpm7* $^{Intestine\ KO}$ mice of the “high Zn diet” survived to weaning (Figure 30 C) and had to be euthanized afterwards at P23 and P33, respectively. Weaned *Trpm7* $^{Intestine\ KO}$ mice were smaller in size compared to control littermates (Figure 30 D). Mg^{2+} supplementation was also beneficial for the survival rate of *Trpm7* $^{Intestine\ KO}$ offspring (P = 0.014) (Figure 30 B). The onset of mortality was significantly delayed. Furthermore, one Mg^{2+}-treated mutant was viable at weaning and died at P37.

Importantly, during ~5 years of production of *Trpm7* $^{Intestine\ KO}$ offspring on the regular diet, no single individual could survive till weaning, further reinforcing the positive outcome of dietary Zn^{2+} and Mg^{2+} treatments. Thus, nutritional supplementation by Zn^{2+} and to a less degree by Mg^{2+} extended the lifespan of *Trpm7* $^{Intestine\ KO}$ animals.

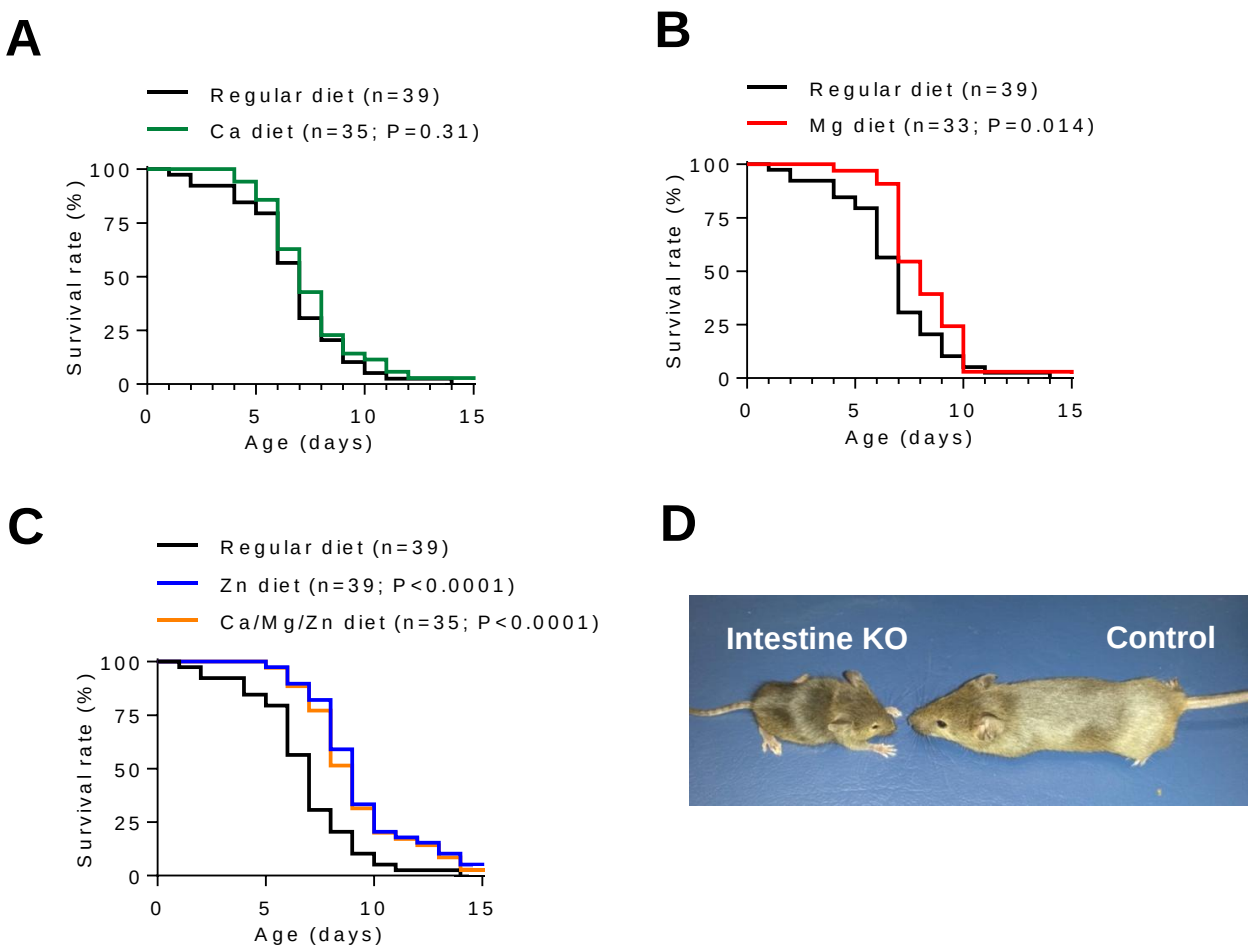

Figure 30: Survival rates of control and *Trpm7* $^{Intestine\ KO}$ animals fed with control *vs* high Ca^{2+}, Mg^{2+}, Zn^{2+} and triple diet. Breeding pairs (♀*Trpm7* $^{fl/fl}$ x ♂ *Trpm7* $^{fl/wt}$; *Villin1-Cre*) were maintained on either a control diet (A-C) or a high Ca^{2+} **(A)**, Mg^{2+} **(B)**, Zn^{2+} or triple **(C)** diet. For statistical analysis each experimental group was compared to the control group using log-rank test. **(D)** Representative image of surviving P33 *Trpm7* $^{Intestine\ KO}$ mouse and a corresponding control littermate maintained at high Zn^{2+} diet; n - number of mice.

Next, we asked whether a combined diet with high levels of Zn^{2+}, Ca^{2+} and Mg^{2+} can improve the survival rate of mutant mice (Table 63). However, the combined diet did not extend the lifespan of *Trpm7* $^{Intestine\ KO}$ animals beyond that one displayed by the Zn^{2+}-treated group (with 1 animal survived to weaning and died at P21). These findings suggest that Zn^{2+} deficiency underlies the mortality of *Trpm7* $^{Intestine\ KO}$ mice and that additional dietary Mg^{2+} and Ca^{2+} could not circumvent this outcome.

6.4.5 Analysis of transcriptional changes of *Trpm7* $^{Intestine\ KO}$ mice

To get an unbiased insight into cellular processes affected in the intestine of *Trpm7* $^{Intestine\ KO}$ mice, we isolated RNA from the villi of P5 *Trpm7* $^{Intestine\ KO}$ and control littermates and performed a genome-wide transcriptome profiling using gene microarray approach (NCBI Gene Expression Omnibus (GEO), GSE110613). Using a 2-fold change cut-off value with $P \leq 0.05$ for the false discovery rate (FDR), we found 455 genes up- or downregulated in the *Trpm7* $^{Intestine\ KO}$ mice (list of regulated genes can be found at https://www.pnas.org/content/early/2019/02/14/1810633116/tab-figures-data, Dataset S02). Using the Ingenuity Pathway Analysis (IPA), we figured out that gene networks controlled by nuclear factor erythroid-derived 2-like 2 (Nrf2) were strongly upregulated. Nrf2 is a transcriptional factor triggering oxidative stress response [156]. One of the most abundant Nrf2-dependent antioxidant metabolites is glutathione (GSH). GSH is required for the neutralization of reactive oxygen species (ROS) [157]. The glutathione-mediated detoxification pathway (Figure 31) was highly affected in the villi of *Trpm7* $^{Intestine\ KO}$ mice. Therefore, we aimed to verify transcriptional changes in genes of the glutathione-mediated detoxification pathway using qRT-PCR.

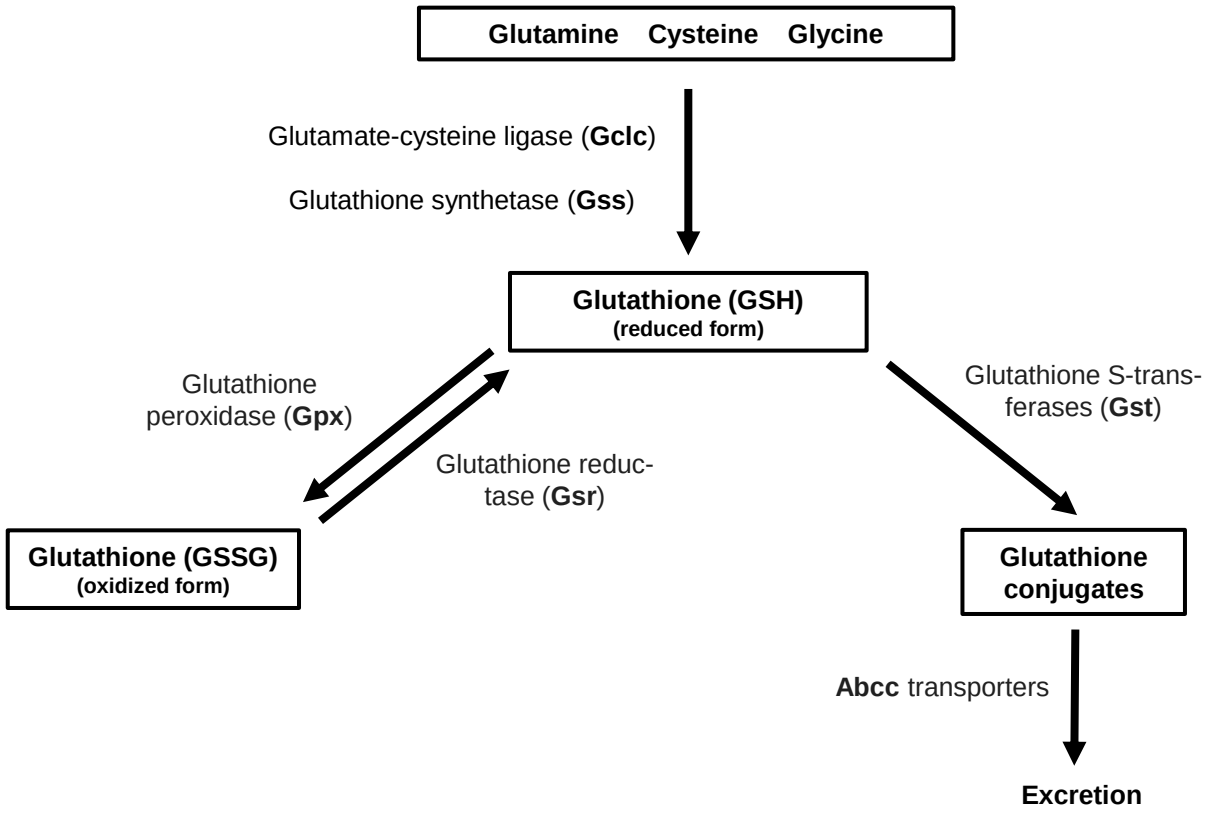

Figure 31: Summary of the glutathione-mediated detoxification pathway.

Nrf2 regulates the expression of glutamate-cysteine ligase (Gclc) and glutathione synthetase (Gss) (Figure 31), two enzymes controlling glutathione synthesis [158, 159]. Both enzymes were strongly upregulated in *Trpm7* $^{Intestine\ KO}$ mice (Figure 32 A). In addition, Nrf2 regulates expression of glutathione peroxidases (Gpx2) and glutathione reductase (Gsr) [160, 161]. Gpx2 reduces ROS via oxidation of GSH leading to the formation of GSH dimer (GSSG). Afterwards, Gsr regenerates GSH from GSSG. Expression of Gpx2 and Gsr was significantly increased in *Trpm7* $^{Intestine\ KO}$ mice (Figure 32 B).

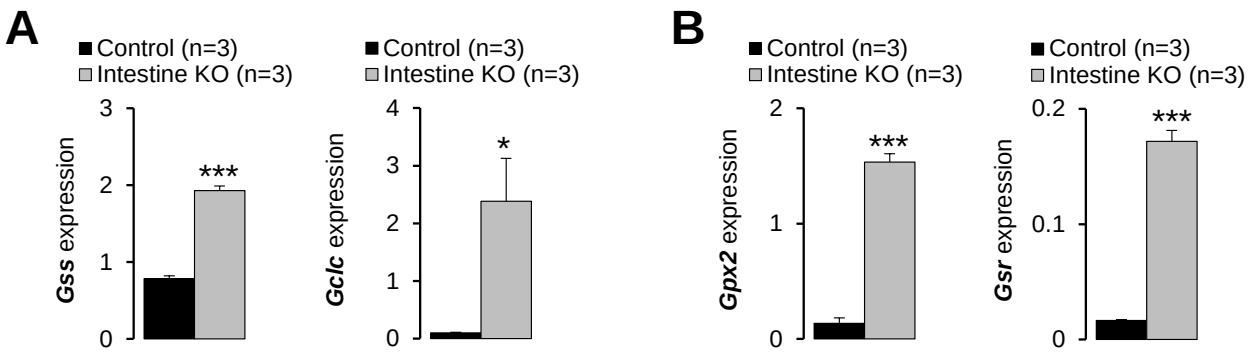

Figure 32: Relative expression levels of genes involved in synthesis and redox activity of glutathione in the villi of control and *Trpm7* $^{Intestine\ KO}$ mice. (A) mRNA levels of *Gss* and *Gclc* (involved in GSH synthesis) as well as **(B)** *Gpx2* and *Gsr* (involved in redox activity of GSH) were measured using qRT-PCR and *Hprt* as a reference transcript. Values are mean ± SEM; *** - P≤0.001, * - P≤0.05 (Student's t-test); n - number of mice.

In addition, Nrf2 controls the expression of many ROS-detoxifying enzymes such as glutathione S-transferases (Gst) catalyzing the conjunction of reactive oxidative species to glutathione [162]. Consistently, we found that expression of many Gsts was upregulated in *Trpm7* $^{Intestine\ KO}$ mice (Figure 33).

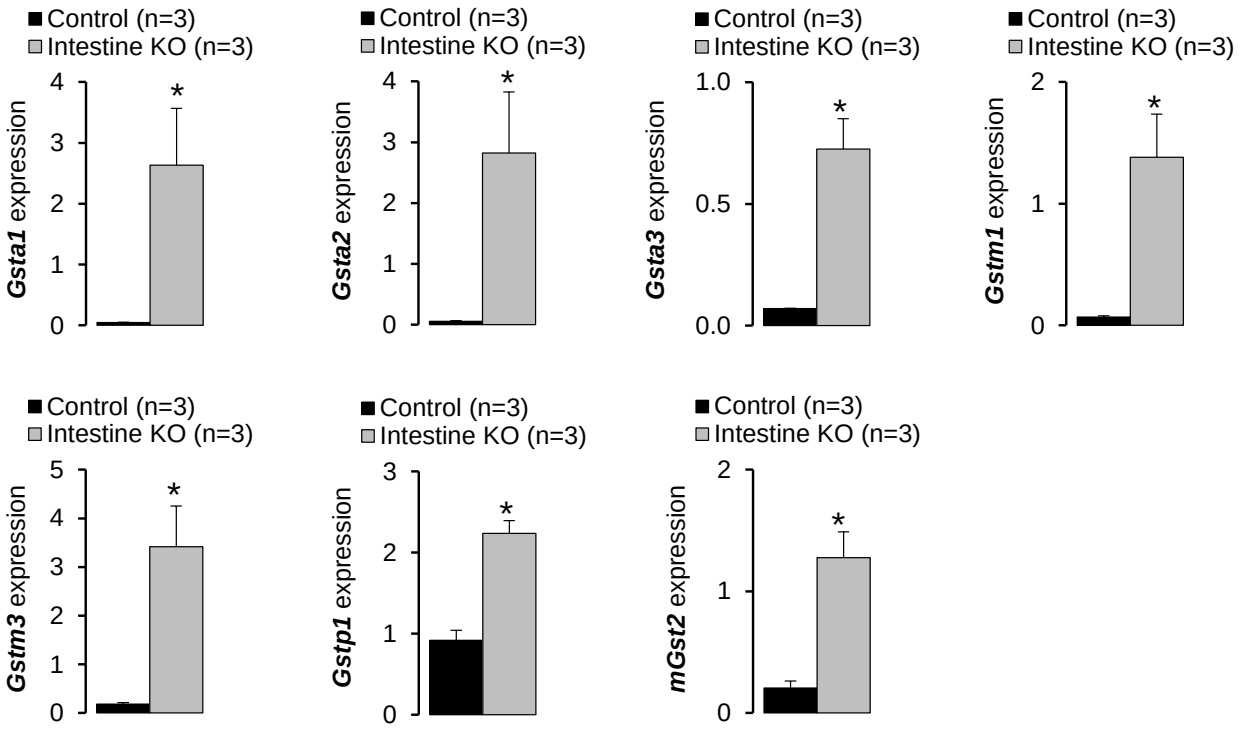

Figure 33: Expression analysis of glutathione S-transferases (Gst) in villi of control and *Trpm7* $^{Intestine\ KO}$ mice. mRNA levels of the glutathione S-transferases *(Gsta1, Gsta2, Gsta3, Gstm1, Gstm3, Gstp1 and mGst2)* were measured using qRT-PCR and *Hprt* as a reference transcript. Values are mean ± SEM; * - P≤0.05 (Student's t-test); n - number of mice.

Glutathione conjugates can be excreted from the cell by Abcc transporters (Figure 31) [163], which were also upregulated in mutant tissue (Figure 34). Hence, we concluded that Nrf2-mediated oxidative stress response was triggered in villi of *Trpm7* $^{Intestine\ KO}$ mice.

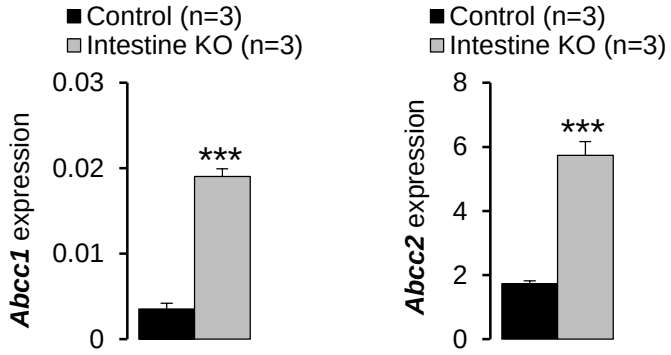

Figure 34: Expression of Abcc transporters in villi of control and *Trpm7* $^{Intestine\ KO}$ mice. mRNA levels of *Abcc1* and *Abcc2* were measured using qRT-PCR and *Hprt* as a reference transcript. Values are mean ± SEM; *** - P≤0.001 (Student's t-test); n - number of mice.

6.4.6 Assessment of the immunological status of *Trpm7* $^{Intestine\ KO}$ mice

It is well documented in the scientific literature that Zn^{2+} deficiency negatively impacts the immune system [115, 164]. Accordingly, we investigated whether serum levels of interleukin 6 (IL-6), the key pro-inflammatory factor, were changed in *Trpm7* $^{Intestine\ KO}$ mice. Using an ELISA, we determined that circulating levels of IL-6 were increased (11.1 times) indicating that the function of the immune system was indeed affected in *Trpm7* $^{Intestine\ KO}$ mice.

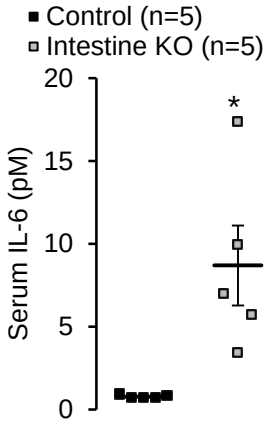

Figure 35: Circulating levels of interleukin 6 (IL-6) in control and *Trpm7* $^{Intestine\ KO}$ mice. The concentration of interleukin 6 in serum of P5 control and *Trpm7* $^{Intestine\ KO}$ animals was measured using an ELISA. The results are shown as mean ± SEM; * - P≤0.05 (Student's t-test); n - number of mice.

Previously, the autopsy of acrodermatitis enteropathica (AE) patients suffering from a strong Zn^{2+} deficiency revealed the lack of germinal centers in the spleen and the absence of thymus [165-167]. Moreover, these studies suggested that pneumonia or sepsis probably caused the death of the patients [165-167]. Further clinical studies and animal experiments could confirm that Zn^{2+} deficiency caused systemic immune deficiency [115, 164]. Consequently, we asked whether the morphology of immune organs was changed in *Trpm7* $^{Intestine\ KO}$ mice. We examined the histological and macroscopic appearance of the spleen (Figure 36) and the thymus (Figure 37) in P5 *Trpm7* $^{Intestine\ KO}$ and control mice. We noted that thymus of *Trpm7* $^{Intestine\ KO}$ mice was substantially smaller in the mutant mice (Figure 36 A, B). Interestingly, two mutant mice were completely athymic. Further histological analysis revealed that the medulla region was not visible in the thymus of *Trpm7* $^{Intestine\ KO}$ mice (Figure 36 C).

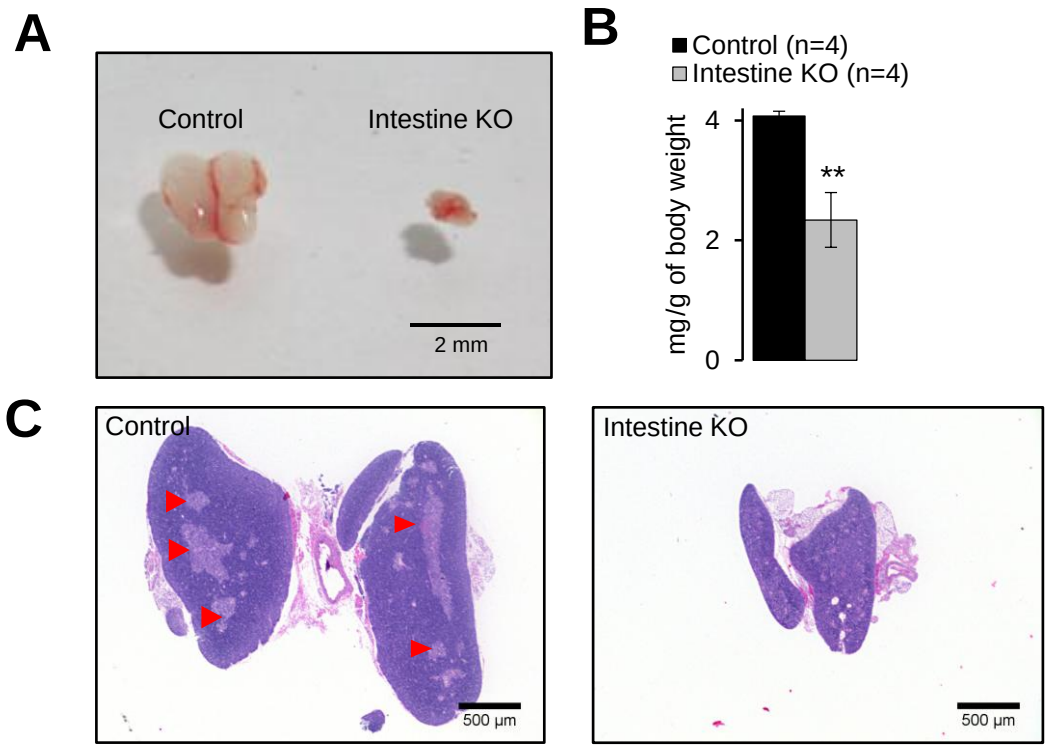

Figure 36: Morphology of thymus of P5 control and *Trpm7* $^{Intestine\ KO}$ mice. Overall appearance **(A)**, tissue weight normalized to body weight **(B)** and H&E staining of paraffin-embedded sections **(C)** of the thymus from P5 control and *Trpm7* $^{Intestine\ KO}$ littermates. The triangles indicate the medulla region present only in the thymus of control animals. Representative images are shown (n=5 tissues per genotype); ** - P≤0.01 (Student's t-test); n - number of mice.

Spleen was present in all P5 *Trpm7* $^{Intestine\ KO}$ mice. However, the size of the organ was significantly reduced (Figure 37 A, B). Interestingly, the white pulp microarchitecture was only detectable in the spleen of control animals. To conclude, we could show that *Trpm7* $^{Intestine\ KO}$ mice develop crucial abnormalities in morphology and development of lymphoid organs (Figure 36, Figure 37). These results support the idea that similar to AE patients impaired Zn^{2+} homeostasis in *Trpm7* $^{Intestine\ KO}$ mice leads to systemic immune deficiency and death of animals.

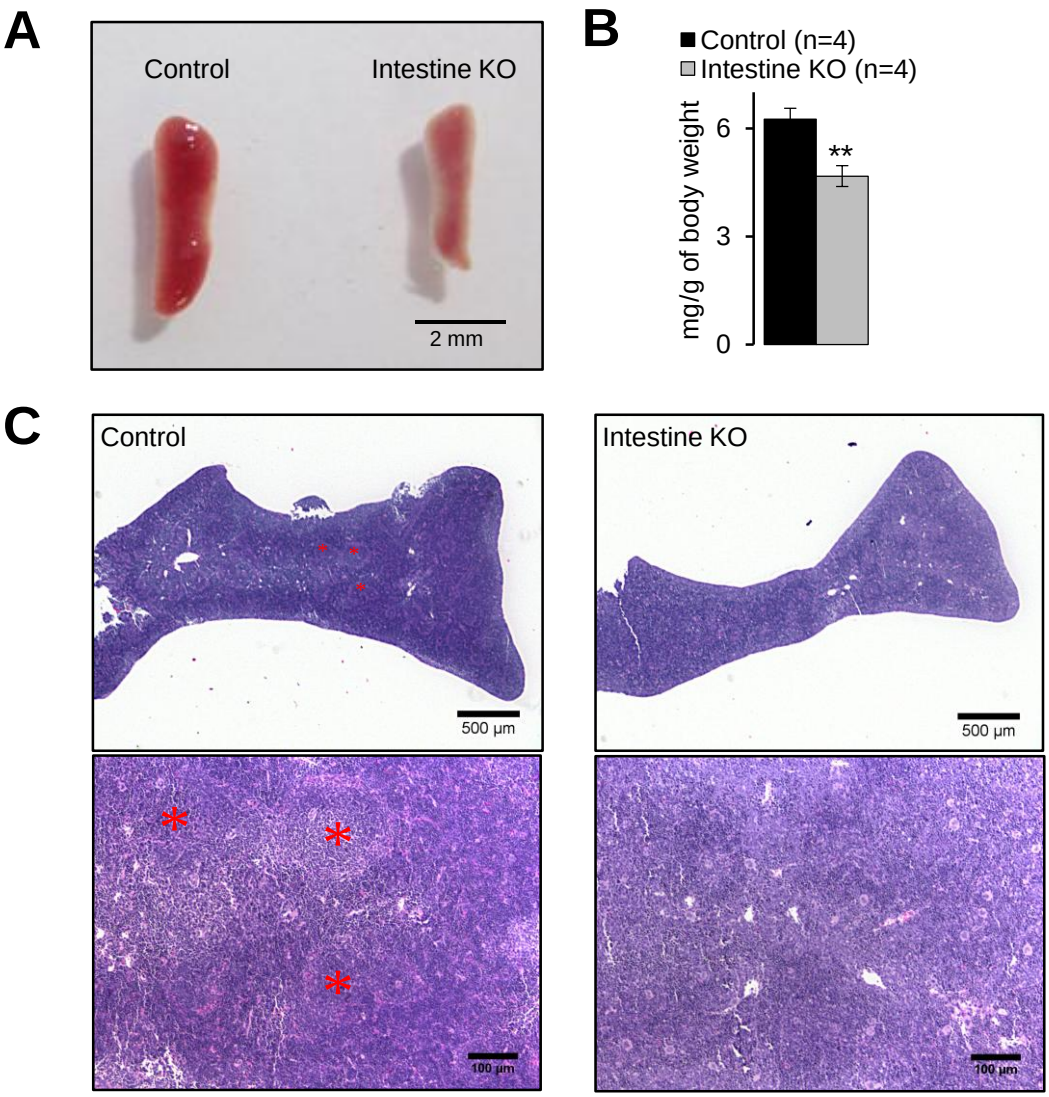

Figure 37: Morphology of spleen in P5 control and *Trpm7* $^{Intestine\ KO}$ mice. Overall appearance **(A)**, tissue weight normalized to body weight **(B)** and H&E staining of paraffin-embedded sections **(C)** of the spleen from P5 control and *Trpm7* $^{Intestine\ KO}$ littermates. The stars indicate the white pulp observed only in control organs. Representative images are shown (n=5 tissues per genotype); ** - P≤0.01 (Student's t-test); n - number of mice.

6.5 Assessment of TRPM7's kinase function on organismal mineral homeostasis

As TRPM7 comprises a channel and a protein kinase moiety, we asked whether the lack of kinase activity may play a role in the deficiency of divalent cations in *Trpm7* $^{Intestine\ KO}$ mice. We examined a kinase-dead mouse strain carrying a point mutation in its catalytic site (Figure 10, Table 46). This line was previously reported by Kaitsuka and colleagues [65]. In our study, we crossed females and males heterozygous for the kinase-dead mutation and used *Trpm7* $^{ki/ki}$ (KI) and *Trpm7* $^{wt/wt}$ (control) littermates for a follow-up phenotypic analysis. For genotyping of *Trpm7* $^{ki/ki}$, *Trpm7* $^{ki/wt}$ and *Trpm7* $^{wt/wt}$ offspring, we used PCR primers flanking the DNA sequence containing the point mutation. The corresponding PCR produces a 205 bp product for both wt and ki allele. However, the sequence of the wt allele contains a recognition sequence of the Tru1I restriction enzyme (**T**/TAA). Exchange of T by C (**C**/TAA) in K1646R TRPM7 variant destroys this sequence motif. Consequently, Tru1I was used to probe wt *vs* ki sequence in PCR amplicon as outlined in Figure 38.

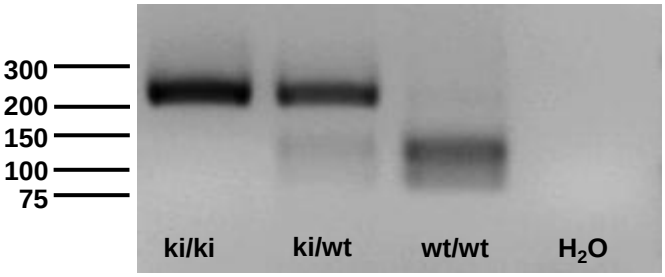

Figure 38: Genotyping of *Trpm7* $^{ki/ki}$, *Trpm7* $^{ki/wt}$ and *Trpm7* $^{wt/wt}$ mice. Genomic DNA obtained from tail fragments of *Trpm7* $^{ki/ki}$, *Trpm7* $^{ki/wt}$ and *Trpm7* $^{wt/wt}$ mice was analyzed by PCR approach using primers specific for the region carrying the point mutation. Amplicons were treated with the restriction enzyme Tru1I. The PCR amplicons (205 bp for *Trpm7* ^{ki}; 120 and 85 bp for *Trpm7* ^{wt}) were examined using agarose gel electrophoresis. H_2O was used to verify the specificity of PCR.

In line with previous reports [43, 64, 65], *Trpm7* $^{ki/ki}$ mice displayed a normal physical appearance, unchanged body weight (Figure 39 A) and no sign of early mortality (Figure 39 B). In addition, genotyping of offspring resulted in the expected Mendelian inheritance of the KI alleles (Table 46).

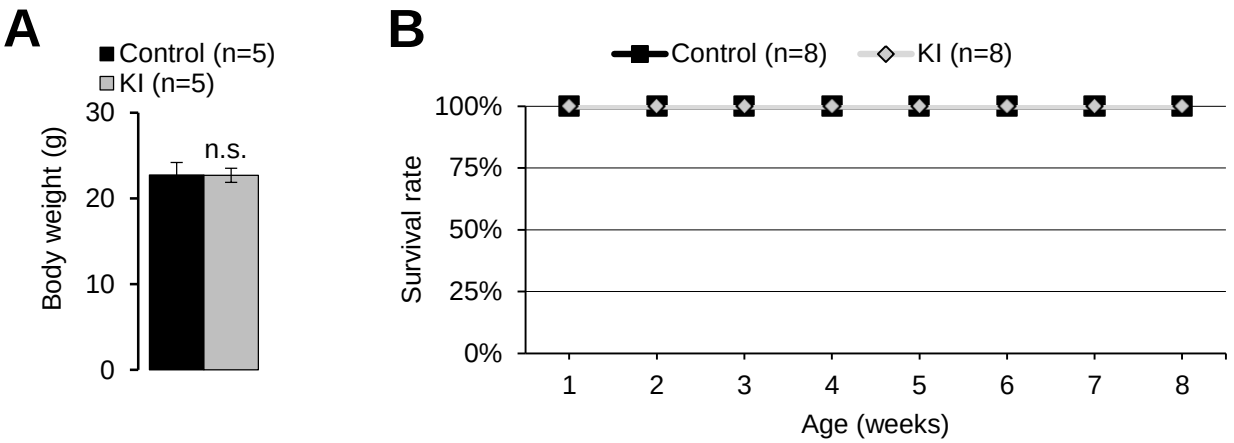

Figure 39: Body weight and survival rate of *Trpm7* $^{wt/wt}$ (control) and *Trpm7* $^{ki/ki}$ (KI) mice. (A) Body weight of 8 weeks old *Trpm7* $^{wt/wt}$ (control) and *Trpm7* $^{ki/ki}$ (KI) mice. **(B)** *Trpm7* $^{ki/ki}$ mutation did not induce mortality in the mutant mice during 8 weeks of the postnatal life. Values are mean ± SEM; n.s. - not significantly different (Student's t-test); n - number of mice.

Next, we investigated the mineral content in serum and bones of 8 weeks old *Trpm7* $^{wt/wt}$ and *Trpm7* $^{ki/ki}$ littermates using ICP-MS. Mg and Zn concentrations were not altered (Figure 40), whereas Ca levels were modestly elevated in serum but were normal in bones (Figure 40 A, B). These findings suggest that the lack of TRPM7 channel, but not kinase activity, triggers the phenotype of *Trpm7* $^{Intestine\ KO}$ mice.

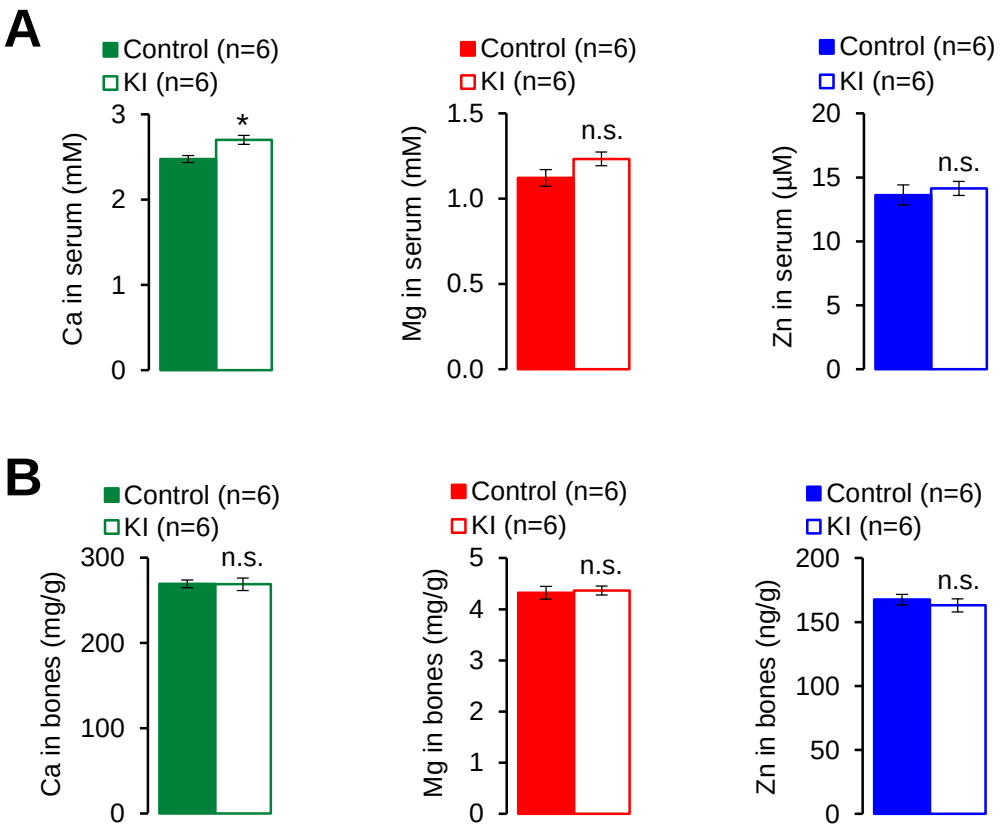

Figure 40: Assessment of divalent cation levels in serum and bones of *Trpm7* $^{wt/wt}$ (control) and *Trpm7* $^{ki/ki}$ (KI) mice. Levels of Ca *(left panel)*, Mg *(middle panel)* and Zn *(right panel)* were examined in serum **(A)** and bones (right tibia) **(B)** in 8 weeks old control and KI mice using ICP-MS. Values are mean ± SEM; * - P≤0.05 (Student's t-test), n.s. - not significantly different; n - number of mice.

7 Discussion

7.1 TRPM7 regulates the cellular contents of Zn^{2+} and Mg^{2+}

Independent studies have shown that the TRPM7 channel is a constitutively active channel, which is highly permeable to divalent cations with the permeability sequence $Zn^{2+} > Mg^{2+} \geq Ca^{2+}$ [6, 13, 14, 168-171]. However, these patch-clamp experiments were performed using TRPM7 transfected cells exposed to extracellular solutions with very high levels of individual cations (10-20 mM or 120 mM) and complete removal of intracellular divalent cations. Therefore, the particular cellular function of the native TRPM7 channel under physiological conditions remains incompletely understood [6, 17, 43, 44]. For instance, the role of TRPM7 in the cellular balance of Mg^{2+} *vs* Ca^{2+} is discussed controversially in the field [17, 59]. In addition, it is difficult to estimate whether endogenous TRPM7 is capable to regulate the influx of Zn^{2+} under a ~100-fold excess of Mg^{2+} and Ca^{2+}.

In order to clarify these issues, we explored a HAP1 cell line carrying a loss-of-function mutation in *TRPM7* introduced by the CRISPR/Cas9 approach [44]. We cultured HAP1 cells in a medium containing physiological levels of extracellular Zn^{2+}, Ca^{2+} and Mg^{2+} and analyzed elementary contents of divalent and monovalent cations using ICP-MS. We could show that the total level of Zn^{2+} was decreased in HAP1 cells and that Zn^{2+} deficiency can be compensated by the addition of exogenous Zn^{2+} to the cell culture medium. In follow-up experiments, we examined the ability of TRPM7 to regulate the uptake of the radioactive zinc isotope $^{65}Zn^{2+}$ in HAP1 cells exposed to saline containing physiological levels of extracellular Mg^{2+}, Ca^{2+} and Zn^{2+}. We demonstrated that *TRPM7*-deficient HAP1 cells displayed diminished $^{65}Zn^{2+}$ influx. Hence, the preference of the TRPM7 channel pore for Zn^{2+} correlates with the nonredundant role of TRPM7 in maintaining the cellular balance of Zn^{2+}.

In line with previous studies [6, 17, 43, 44], we observed that the lack of TRPM7 leads to decreased content of elementary Mg^{2+} in HAP1 cells. However, we found that total cellular concentrations of Ca^{2+} and monovalent cations were not affected in *TRPM7*-deficient HAP1 cells. Taken together, our experiments revealed that the TRPM7 channel is required for cellular uptake of Zn^{2+} and Mg^{2+} in the cell. Accordingly, we propose that a particular cellular response to the inactivation of TRPM7 will depend on (i) the actual metabolic demand of the cell for an individual cation and (ii) expression of other channels/transporters within the cell.

7.2 TRPM7 is redundant for renal handling of Ca^{2+}, Zn^{2+} and Mg^{2+}

Previously, it was reported that the expression level of *Trpm7* is high in the kidney compared to other organs [145], suggesting that TRPM7 may play a critical role in renal handling of Mg^{2+}, Ca^{2+} and Zn^{2+}. While a role of the kidney in reabsorption of Zn^{2+} remains unknown, the systemic homeostasis of Mg^{2+} and Ca^{2+} was thought to rely on a transcellular transport of these cations in the DCT nephron segment [76, 86, 141]. Using *in situ* hybridization (ISH), we could show that *Trpm7* is highly expressed in nephron segments resembling DCT. In line with these results, high expression levels of *Trpm7* were observed in two other recent studies [143]. Our examination of *Trpm7* $^{Kidney\ KO}$ mice confirmed an efficient deletion of *Trpm7* transcripts in the DCT. Surprisingly, we found no detectable changes in physical appearance or behavior of mutant mice as well as serum levels and urinary excretion rates of Ca^{2+}, Zn^{2+} or Mg^{2+}. These findings argue that TRPM7 is functionally redundant in the DCT.

7.3 Intestinal TRPM7 is essential for postnatal growth and survival of mice

To gain insight whether TRPM7 is necessary for intestinal uptake of divalent cations, we explored *Villin1-Cre* transgene enabling to induce inactivation of TRPM7 specifically in the enterocytes of the whole intestine in *Trpm7* $^{fl/fl}$ mice [59, 134]. On the contrary to the *Trpm7* $^{Kidney\ KO}$ mice, intestine-specific deletion of TRPM7 had a strong impact on the postnatal development of *Trpm7* $^{Intestine\ KO}$ mice. The mutants were born in the expected ratio and were indistinguishable from control littermates at P1. However, *Trpm7* $^{Intestine\ KO}$ mice nearly stopped to grow at P3–5. Furthermore, P3–P5 *Trpm7* $^{Intestine\ KO}$ pups displayed a very high mortality rate and all mutants died after P10.
Consequently, we asked whether the lack of intestinal TRPM7 could affect morphogenesis of the gut resulting in nutritional malabsorption of newborn mice. To this end, we performed an extensive assessment of P1–P5 littermates to establish whether intestinal deletion of TRPM7 induced negative effects on the macroscopic or histological appearance of the intestine, tissue homeostasis and overall transcriptional profile of the intestine. Specifically, we found that the stomach of *Trpm7* $^{Intestine\ KO}$ pups was filled with milk, suggesting that the feeding behavior of the mutants was normal. We noted that the length of the whole intestine was identical in *Trpm7* $^{Intestine\ KO}$ pups and control mice. Histological examination of the small and large intestine isolated from *Trpm7* $^{Intestine\ KO}$ individuals at P1 did not show remarkable abnormalities of mucosal or villi architecture indicating unaffected intestinal organogenesis. In addition, we extracted RNA from the whole duodenum of P5 control and mutant littermates and investigated the expression levels of transcriptional markers of tuft cells, enterocytes, intestinal stem cells, Paneth cells and goblet cells. We found that, except the Paneth cell marker, the expression levels of these transcripts were not altered suggesting that the deletion of TRPM7 did not impact the development of major types of intestinal epithelial cells.

Finally, we used an unbiased strategy to examine villus cell homeostasis in *Trpm7* $^{Intestine\ KO}$ mice: we extracted RNA from villi isolated from the whole intestine of P5 littermates and performed genome-wide transcriptome profiling. We found that inactivation of *Trpm7* affected primarily transcriptional networks controlling glutathione-mediated detoxification, Nrf2-mediated oxidative stress response, cholesterol biosynthesis and xenobiotic metabolism. It is well documented, that abnormal Zn^{2+} and Mg^{2+} balance can elicit oxidative stress [42, 172]. For instance, genetic inactivation of *Trpm6* in mice leads to systemic Mg^{2+} deficiency associated with an induction of gene networks controlling oxidative stress in the liver [44]. Interestingly, oxidative stress has also been linked to TRPM7 in cultured neurons and other cell types [48, 173].

Oxidative stress is a metabolic disturbance that is followed by the oxidation of biomolecules, resulting in oxidative damage of cells and tissues [172]. The transcriptional regulator Nrf2 controls the expression of enzymes involved in the glutathione (GSH) dependent neutralization of reactive oxygen species (ROS) [156, 174]. Accordingly, we conducted additional experiments to elucidate expression levels of 18 Nrf2-dependent transcripts involved in the metabolism of GSH and found that these transcripts are highly upregulated in the intestine of P5 mutants. Altogether, we concluded that the intestine specific deletion of *Trpm7* did not affect the morphogenesis and tissue homeostasis of the intestine, but rather engenders postnatal metabolic deficits associated with oxidative stress.

A systemic deficiency of Zn^{2+}, Mg^{2+} or Ca^{2+} is frequently accompanied by growth failure and even death of mice [44, 107, 131]. Therefore, we studied whether diminished uptake of divalent cations has underlain the striking phenotypes of *Trpm7* $^{Intestine\ KO}$ animals. In line with macroscopic appearance of P1 *Trpm7* $^{Intestine\ KO}$ mice, we found no significant changes in Zn^{2+}, Ca^{2+} or Mg^{2+} levels in serum and bones at P1, indicating that newborn *Trpm7* $^{Intestine\ KO}$ mice had normal nutritional intake of these minerals. At P3, circulating levels of Zn^{2+} and Ca^{2+} were decreased in bones. Most notably, P5 mutants displayed very low levels of Zn^{2+}, Ca^{2+} and Mg^{2+} in serum. In P5 bones we found a similar pattern: Zn^{2+} and Ca^{2+} concentrations were significantly reduced, while Mg^{2+} contents were normal. Importantly, levels of the monovalent cations (Na^{+} and K^{+}) were nearly identical in P1–5 *Trpm7* $^{Intestine\ KO}$ and control animals.

Accordingly, based on our findings we offer a new concept resolving a ‘paradox’ of TRPM7 functioning either as a Ca^{2+} *or* Mg^{2+} *or* Zn^{2+} permeable ion channel in epithelial cells. We propose that TRPM7 functions as a *common* gatekeeper regulating the bulk nutritional uptake of essential divalent metals, and not specific to only one.

7.3.1 Emerging role of the TRPM7 channel in Zn^{2+} homeostasis

A key finding of the present study is that the TRPM7 channel regulates cellular Zn^{2+} levels and that such function appears to correlate with the *in vivo* role of TRPM7 in intestinal uptake of this cation. It is well established that the small intestine controls whole-body Zn^{2+} balance by adjusting absorption and excretion rates of Zn^{2+}, whereas a role of the kidney in systemic Zn^{2+} homeostasis is considered as minor [117, 118].

Mechanistically, nutritional intake of Zn^{2+} remains poorly understood. Two large families of Zn^{2+} transporters are thought to be involved in such processes. 10 ZnT transporters (ZnT1-10, also known as Slc30a1-10) were suggested to regulate efflux of cytoplasmic Zn^{2+} to extracellular space or uptake of cytosolic Zn^{2+} in intracellular vesicles serving as Zn^{2+} stores [115]. In contrast, 14 Zip transporters (Zip1-14 or Slc39a1-14) increase cytoplasmic Zn^{2+} levels by facilitating extracellular and vesicular Zn^{2+} transport in the cytoplasm [115]. Many ZnT and Zip proteins were found to be expressed in the small intestine [115]. However, with a few exceptions (discussed below), genetic animal models failed to demonstrate a particular role of ZnT and Zip proteins in Zn^{2+} nutrition, possibly because of their functional redundancy.

Spontaneous mutations in the murine *ZnT4* gene, which is expressed in mammary glands and intestine [147, 175], result in the “lethal milk” phenotype [175]. The key characteristic of the “lethal milk” syndrome is a ~35% decreased concentration of Zn^{2+} in breast milk of mutant dams [176] causing 100% death of suckled offspring within 10 days of postnatal life [155]. When pups homozygous for *ZnT4* mutation are suckled by wt foster mothers, they develop normally [176]. Adult ZnT4-deficient mice develop a mild form of Zn^{2+} deficiency [177]. It was proposed that ZnT4 is located on the basolateral cell surface of epithelial cells to regulate Zn^{2+} efflux in the bloodstream or breast milk [177]. As serum Zn^{2+} concentrations in *Trpm7*-deficient mice were only 39% of control values at P5, it is to be expected that the early postnatal mortality of *Trpm7*-deficient mice is similar to the “lethal milk” genetic model.

Unlike to *ZnT4*, *Zip4* is primarily expressed in the small intestine and is located to the apical surface of enterocytes [122, 123, 178, 179]. Mutations in the human *ZIP4* gene result in the genetic syndrome “acrodermatitis enteropathica” (AE) caused by a disturbed intestinal Zn^{2+} absorption [122, 128, 129]. A mouse model with a deletion of *Zip4* specifically in the epithelial cells of the intestine *(Zip4 intestine KO)* was generated to verify this function [131]. Similar to human AE patients, *Zip4*-deficient animals develop normally until weaning because breast milk is particularly enriched in Zn^{2+}. However, adult mutants develop a fatal Zn^{2+} deficiency. *Zip4*-deficient animals are characterized by a rapid loss of weight. The mortality of *Zip4*-deficient animals is rescued by an excess of Zn^{2+} in the drinking water. Since *Zip4 intestine KO* mice develop symptoms only after weaning it was speculated that there is an additional route for intestinal Zn^{2+} uptake [133], likely by TRPM7. MT1 is the main intracellular scavenger of Zn^{2+}, which is transcriptionally regulated by Zn^{2+} availability [124, 125]. Interestingly, *Zip4 intestine KO* and *ZnT4 KO* mice show a strong

upregulation of intestinal MT1 [131, 177]. We observed a similar pattern: MT1 was significantly upregulated in *Trpm7* $^{Intestine\ KO}$ animals. Expression of metallothioneins can also be induced by oxidative stress [180]. We found that gene networks of oxidative stress were enhanced in the villi of *Trpm7* $^{Intestine\ KO}$ mice. Hence, the upregulation of MT1 in epithelial cells of *Trpm7* $^{Intestine\ KO}$ mice may be caused by oxidative stress and/or impaired Zn^{2+} balance. In addition, consistently with previous studies [131, 177], we found that mRNA levels of *ZnT1*, *ZnT2*, *Zip4* and *Zip5* were significantly downregulated in tissues of *Trpm7* $^{Intestine\ KO}$ animals.

A particular link between insufficient nutritional intake of Zn^{2+} and death has not yet been established for the deadly-milk *ZnT4*-deficient strain. Looking for such a link in *Trpm7* $^{Intestine\ KO}$ mice, we resorted to the pioneering autopsy of AE patients, which revealed the absence of thymus and the lack of germinal centers in the spleen. Pneumonia or sepsis was likely causing the death of these patients [165-167]. Follow-up clinical studies and experiments with animal models have fostered the commonly accepted view that organismal Zn^{2+} deficiency leads to a systemic decline of innate and adaptive immune response [115, 164]. Consequently, we examined the macroscopic and histological appearance of thymus and spleen in *Trpm7* $^{Intestine\ KO}$ mice. Notably, two mutant mice were athymic, while the remaining *Trpm7* $^{Intestine\ KO}$ mice had only rudimentary organs. Spleen was present in all mutant mice, but the size of the organ was substantially reduced. Histological analysis revealed that *Trpm7* $^{Intestine\ KO}$ mice develop grave abnormalities in the morphology of lymphoid organs. Thus, the medulla region was not visible in the thymus of mutant mice. In the spleen of *Trpm7* $^{Intestine\ KO}$ mice, the white pulp microarchitecture was not detectable. Based on these findings we propose that *Trpm7* $^{Intestine\ KO}$ mice develop immune deficiency incompatible with organismal survival. In line with this idea, we observed that *Trpm7* $^{Intestine\ KO}$ mice display remarkably high circulating levels of the pro-inflammatory cytokine IL-6.

Finally, we demonstrated that high Zn^{2+} diets of breeding dams significantly improved the survival of *Trpm7* $^{Intestine\ KO}$ mice (particularly at the onset of mortality, P3–5). Furthermore, in contrast to the situation with the untreated group of *Trpm7* $^{Intestine\ KO}$ mice, the Zn^{2+}-enriched diet allowed two mutants to survive until weaning. Furthermore, we examined the survival rate of mutant pups from females maintained on a combined diet enriched in Ca^{2+}, Mg^{2+} and Zn^{2+} and found that the survival distribution of this group closely resembles that of the group receiving a high Zn^{2+} diet, suggesting that Zn^{2+} deficiency in *Trpm7*-deficient mice plays the predominant role in early mortality. As discussed above, such an outcome is not unexpected, because new-born rodents are highly sensitive to insufficient intake of Zn^{2+}. It should also be noted that in contrast to a classical genetic approach when the mutant locus is complemented by a functional variant of the gene, the efficiency of nutritional Zn^{2+} fortification in our experimental setting is limited by (i) the ability of nursing females to increase Zn^{2+} in milk and (ii) the capability of other intestinal transporters to compensate for the lack of TRPM7. Therefore, a complete rescue of the mortality of *Trpm7*-deficient mice cannot be expected realistically. Taken together, these results are well consistent with the suggested role of TRPM7 as a gatekeeper of nutritional intake of Zn^{2+}.

7.3.2 Intestinal TRPM7 as a new player in organismal Ca^{2+} balance

Early studies revealed that body balance of Ca^{2+} is maintained by intestinal uptake and renal reabsorption of Ca^{2+} primarily via a transcellular route consisting of apical entry and basolateral extrusion of Ca^{2+}. Historically, Ca^{2+}-selective channels are thought to underlie the apical Ca^{2+} entry. Thus, the Ca^{2+}-selective TRPV6 channel was proposed to operate as a major player in intestinal Ca^{2+} uptake, and TRPV5 was proposed as a gatekeeper of renal reabsorption of Ca^{2+}. However, *Trpv5 and Trpv6* null mice did not display a significant reduction of serum Ca^{2+} levels. Furthermore, *Trpv6* null mice showed only modestly diminished [107] or even unchanged intestinal Ca^{2+} absorption [113, 114] suggesting that additional absorption pathways play a role.
In the present study, we show that mice with an intestinal deletion of TRPM7 display a severe Ca^{2+} deficiency at early postnatal stages. Specifically, mutant P5 pups displayed a strong decrease in Ca^{2+} concentrations in both serum and bones, increased serum concentrations of PTH (18.2-fold) and 1,25-$(OH)_2D_3$ (9.4-fold) as well as a strong upregulation of *Cyp27b1*, *Trpv6* and *Calbindin-D9k* transcripts. These findings suggest that TRPM7, rather than TRPV5 or TRPV6, represents the indispensable mechanism controlling the systemic intestinal Ca^{2+} balance.

7.3.3 A new role of TRPM7 in systemic Mg^{2+} homeostasis

Mg^{2+} is required for many biologic processes [42]. More than 20 membrane Mg^{2+} channels/transporters have been suggested. However, their precise function remains not well understood. The kinase-channel TRPM6 is the closest homologue of TRPM7. Recently, our group has demonstrated that mice with a global deletion of *Trpm6 (Trpm6 KO)* develop a severe organismal deficiency in Mg^{2+} [44]. Breastfed *Trpm6* null pups developed normally. In contrast, 8 weeks old *Trpm6 KO* animals displayed a strong depletion of Mg^{2+} in bones and significant reduction of serum Mg^{2+} levels due to a defective intestinal uptake of Mg^{2+} [44]. Soon after weaning, *Trpm6 KO* animals showed a high mortality rate. Moreover, intestine-restricted inactivation of *Trpm6* induced a more moderate Mg^{2+} deficiency suggesting that WT kidneys were not capable of compensating for the lack of intestinal TRPM6. These results supported the concept that intestinal TRPM6 is critically involved in Mg^{2+} homeostasis in adult mice.
TRPM7 has already been linked to intestinal Mg^{2+} uptake in studies with mice heterozygous for a global ***Δkinase*** mutation truncating TRPM7 prior to the kinase domain *(Trpm7* $^{\Delta kinase/wt}$ mice) [43]. *Trpm7* $^{\Delta kinase/wt}$ mice were asymptomatic if maintained on a standard animal chow. Fed by a low Mg^{2+} diet, the mutant mice showed decreased Mg^{2+} levels in plasma and bones, an elevated fecal Mg^{2+} content and an increased mortality rate as compared to control mice. The authors concluded that *Trpm7* $^{\Delta kinase/wt}$ mice develop a defect in intestinal Mg^{2+} absorption. However, the biological relevance of these findings is not clear since maintaining of animals using a low Mg^{2+} diet is a very

unphysiological challenge.

In the present work, we demonstrated that intestine-restricted ablation of TRPM7 is sufficient to induce systemic Mg^{2+} deficiency in new-born mice in conjunction with lowered serum levels of IGF1 (a suggested marker of Mg^{2+} deficiency [181]) and upregulated expression of intestinal *Trpm6* (~30-fold) as well as the putative Mg^{2+} transporters *Slc41a1* and *Slc41a2.* In line with these findings, we observed that dietary Mg^{2+} supplementation was beneficial for the survival of *Trpm7* $^{Intestine\ KO}$ mice. Overall, our results indicate that whole-body balance of Mg^{2+} depends on the intestinal TRPM7 channel.

7.4 The TRPM7 kinase activity is dispensable for the organismal balance of divalent cations

Our genetic strategy for conditional deletion of TRPM7 leads to the elimination of both the channel and kinase activities of TRPM7. Consequently, the severe phenotype of *Trpm7* $^{Intestine\ KO}$ mice can be, at least in part, caused by the lack of TRPM7 kinase activity. *In vitro* studies with recombinant TRPM7 produced controversial results regarding the role of TRPM7 kinase in regulation of the channel function. Several publications reported that the kinase activity modulates TRPM7 currents [14, 17, 182], while other studies suggested that TRPM7 kinase has a low impact on the TRPM7 channel [33].

To investigate the physiological role of TRPM7 kinase, two independent groups (Kaitsuka et al. and Ryazanova et al.) generated mice strains carrying a constitutive kinase-dead K1646R mutation in *Trpm7 (Trpm7* $^{ki/ki}$*)* [65, 66]. Kaitsuka et al. revealed that the mutant mice exhibited a normal development and unchanged Mg^{2+} and Ca^{2+} serum concentrations [65]. In another publication, Ryazanova et al. [66] also reported that kinase-dead mice developed normally. However, 6 months old mutants displayed reduced Mg^{2+} content in bones (15%) without remarkable changes of Mg^{2+} levels in serum. Thus, both studies suggested that TRPM7 kinase has a low (if any) impact on the systemic balance of divalent cations. As Kaitsuka et al. and Ryazanova et al. did not attempt to investigate Zn^{2+} homeostasis in kinase-dead TRPM7 mice, we re-examined 8-10 weeks old mutants in our experimental settings. Our experiments did not reveal significant alterations in body balance of divalent cations. We concluded that the phenotype of mice with an intestine-restricted null mutation of *Trpm7* was primarily triggered by the lack of the channel activity of TRPM7.

8 Conclusions

The present study aimed to define the physiological role of the channel-kinase TRPM7 by assessment of TRPM7-deficient cells and phenotyping of mouse strains with organ-restricted null mutations in *Trpm7*. Specifically, the obtained results support the following conclusions:

1. In resting cells, endogenous TRPM7 regulates the influx of Zn^{2+} and Mg^{2+}. Consequently, deletion of TRPM7 results in a reduced cellular content of Mg^{2+} and Zn^{2+}.

2. Conditional disruption of renal *Trpm7* has no effect on mineral homeostasis and postnatal development of mice.

3. Conditional mutagenesis of intestinal *Trpm7* in mice did not affect embryonic morphogenesis of the gut but triggers postnatal metabolic deficits associated with oxidative stress and immunodeficiency due to disrupted Zn^{2+}, Mg^{2+} and Ca^{2+} homeostasis, a scenario incompatible with early postnatal growth and survival. Dietary Zn^{2+} and Mg^{2+} fortifications significantly extended the survival of mutants.

4. Global ablation of TRPM7 kinase activity in mice did not affect organismal homeostasis of divalent cations, reinforcing the importance of the channel activity of TRPM7.

Taken together, these findings support the concept that the organismal balance of Zn^{2+}, Mg^{2+} and Ca^{2+} critically relies on one common gatekeeper, the TRPM7 channel.

9 References

1. Cosens, D.J. and A. Manning, *Abnormal electroretinogram from a Drosophila mutant.* Nature, 1969. **224**(5216): p. 285-7.
2. Minke, B., C. Wu, and W.L. Pak, *Induction of photoreceptor voltage noise in the dark in Drosophila mutant.* Nature, 1975. **258**(5530): p. 84-7.
3. Wu, L.J., T.B. Sweet, and D.E. Clapham, *International Union of Basic and Clinical Pharmacology. LXXVI. Current progress in the mammalian TRP ion channel family.* Pharmacol Rev, 2010. **62**(3): p. 381-404.
4. Nilius, B. and G. Owsianik, *The transient receptor potential family of ion channels.* Genome Biol, 2011. **12**(3): p. 218.
5. Ramsey, I.S., M. Delling, and D.E. Clapham, *An introduction to TRP channels.* Annu Rev Physiol, 2006. **68**: p. 619-47.
6. Nadler, M.J., et al., *LTRPC7 is a Mg.ATP-regulated divalent cation channel required for cell viability.* Nature, 2001. **411**(6837): p. 590-5.
7. Schlingmann, K.P., et al., *TRPM6 and TRPM7--Gatekeepers of human magnesium metabolism.* Biochim Biophys Acta, 2007. **1772**(8): p. 813-21.
8. Schlingmann, K.P., et al., *Hypomagnesemia with secondary hypocalcemia is caused by mutations in TRPM6, a new member of the TRPM gene family.* Nat Genet, 2002. **31**(2): p. 166-70.
9. Walder, R.Y., et al., *Mutation of TRPM6 causes familial hypomagnesemia with secondary hypocalcemia.* Nat Genet, 2002. **31**(2): p. 171-4.
10. Chubanov, V., et al., *Disruption of TRPM6/TRPM7 complex formation by a mutation in the TRPM6 gene causes hypomagnesemia with secondary hypocalcemia.* Proc Natl Acad Sci U S A, 2004. **101**(9): p. 2894-9.
11. Ryazanov, A.G., *Elongation factor-2 kinase and its newly discovered relatives.* FEBS Lett, 2002. **514**(1): p. 26-9.
12. Chubanov, V. and T. Gudermann, *Trpm6.* Handb Exp Pharmacol, 2014. **222**: p. 503-20.
13. Monteilh-Zoller, M.K., et al., *TRPM7 provides an ion channel mechanism for cellular entry of trace metal ions.* J Gen Physiol, 2003. **121**(1): p. 49-60.
14. Runnels, L.W., L. Yue, and D.E. Clapham, *TRP-PLIK, a bifunctional protein with kinase and ion channel activities.* Science, 2001. **291**(5506): p. 1043-7.
15. Runnels, L.W., *TRPM6 and TRPM7: A Mul-TRP-PLIK-cation of channel functions.* Curr Pharm Biotechnol, 2011. **12**(1): p. 42-53.
16. Penner, R. and A. Fleig, *The Mg2+ and Mg(2+)-nucleotide-regulated channel-kinase TRPM7.* Handb Exp Pharmacol, 2007(179): p. 313-28.
17. Schmitz, C., et al., *Regulation of vertebrate cellular Mg2+ homeostasis by TRPM7.* Cell, 2003. **114**(2): p. 191-200.
18. Brauchi, S., et al., *TRPM7 facilitates cholinergic vesicle fusion with the plasma membrane.* Proc Natl Acad Sci U S A, 2008. **105**(24): p. 8304-8.
19. Bernhardt, M.L., et al., *Store-operated Ca2+ entry is not required for fertilization-induced Ca2+ signaling in mouse eggs.* Cell Calcium, 2017. **65**: p. 63-72.
20. Carvacho, I., et al., *TRPM7-like channels are functionally expressed in oocytes and modulate post-fertilization embryo development in mouse.* Sci Rep, 2016. **6**: p. 34236.
21. Fonfria, E., et al., *Tissue distribution profiles of the human TRPM cation channel family.* J Recept Signal Transduct Res, 2006. **26**(3): p. 159-78.
22. Kunert-Keil, C., et al., *Tissue-specific expression of TRP channel genes in the mouse and its variation in three different mouse strains.* BMC Genomics, 2006. **7**: p. 159.

23. Duan, J., et al., *Structure of the mammalian TRPM7, a magnesium channel required during embryonic development.* Proc Natl Acad Sci U S A, 2018. **115**(35): p. E8201-E8210.
24. Yin, Y., et al., *Structure of the cold- and menthol-sensing ion channel TRPM8.* Science, 2018. **359**(6372): p. 237-241.
25. Zhang, Z., et al., *Structure of a TRPM2 channel in complex with Ca(2+) explains unique gating regulation.* Elife, 2018. **7**.
26. Autzen, H.E., et al., *Structure of the human TRPM4 ion channel in a lipid nanodisc.* Science, 2018. **359**(6372): p. 228-232.
27. Duan, J., et al., *Structure of full-length human TRPM4.* Proc Natl Acad Sci U S A, 2018. **115**(10): p. 2377-2382.
28. Hofmann, T., et al., *Activation of TRPM7 channels by small molecules under physiological conditions.* Pflugers Arch, 2014.
29. Xie, J., et al., *Phosphatidylinositol 4,5-bisphosphate (PIP(2)) controls magnesium gatekeeper TRPM6 activity.* Sci Rep, 2011. **1**: p. 146.
30. Fujiwara, Y. and D.L. Minor, Jr., *X-ray crystal structure of a TRPM assembly domain reveals an antiparallel four-stranded coiled-coil.* J Mol Biol, 2008. **383**(4): p. 854-70.
31. Jansen, C., et al., *The coiled-coil domain of zebrafish TRPM7 regulates Mg.nucleotide sensitivity.* Sci Rep, 2016. **6**: p. 33459.
32. Cai, N., et al., *Mass Spectrometric Analysis of TRPM6 and TRPM7 Phosphorylation Reveals Regulatory Mechanisms of the Channel-Kinases.* Sci Rep, 2017. **7**: p. 42739.
33. Matsushita, M., et al., *Channel function is dissociated from the intrinsic kinase activity and autophosphorylation of TRPM7/ChaK1.* J Biol Chem, 2005. **280**(21): p. 20793-803.
34. Clark, K., et al., *Massive autophosphorylation of the Ser/Thr-rich domain controls protein kinase activity of TRPM6 and TRPM7.* PLoS One, 2008. **3**(3): p. e1876.
35. Jiang, J., M. Li, and L. Yue, *Potentiation of TRPM7 inward currents by protons.* J Gen Physiol, 2005. **126**(2): p. 137-50.
36. Demeuse, P., R. Penner, and A. Fleig, *TRPM7 channel is regulated by magnesium nucleotides via its kinase domain.* J Gen Physiol, 2006. **127**(4): p. 421-34.
37. Schmitz, C., F. Deason, and A.L. Perraud, *Molecular components of vertebrate Mg2+-homeostasis regulation.* Magnes Res, 2007. **20**(1): p. 6-18.
38. Runnels, L.W., L. Yue, and D.E. Clapham, *The TRPM7 channel is inactivated by PIP(2) hydrolysis.* Nat Cell Biol, 2002. **4**(5): p. 329-36.
39. Middelbeek, J., et al., *The alpha-kinase family: an exceptional branch on the protein kinase tree.* Cell Mol Life Sci, 2010. **67**(6): p. 875-90.
40. Ryazanov, A.G., K.S. Pavur, and M.V. Dorovkov, *Alpha-kinases: a new class of protein kinases with a novel catalytic domain.* Curr Biol, 1999. **9**(2): p. R43-5.
41. Yamaguchi, H., et al., *Crystal structure of the atypical protein kinase domain of a TRP channel with phosphotransferase activity.* Mol Cell, 2001. **7**(5): p. 1047-57.
42. de Baaij, J.H., J.G. Hoenderop, and R.J. Bindels, *Magnesium in man: implications for health and disease.* Physiol Rev, 2015. **95**(1): p. 1-46.
43. Ryazanova, L.V., et al., *TRPM7 is essential for Mg(2+) homeostasis in mammals.* Nat Commun, 2010. **1**: p. 109.
44. Chubanov, V., et al., *Epithelial magnesium transport by TRPM6 is essential for prenatal development and adult survival.* Elife, 2016. **5**.
45. Faouzi, M., et al., *The TRPM7 channel kinase regulates store-operated calcium entry.* J Physiol, 2017. **595**(10): p. 3165-3180.
46. Zierler, S., et al., *Waixenicin A inhibits cell proliferation through magnesium-dependent block of transient receptor potential melastatin 7 (TRPM7) channels.* J Biol Chem, 2011. **286**(45): p. 39328-35.
47. Wei, C., et al., *Calcium flickers steer cell migration.* Nature, 2009. **457**(7231): p. 901-5.

48. Abiria, S.A., et al., *TRPM7 senses oxidative stress to release Zn2+ from unique intracellular vesicles.* Proc Natl Acad Sci U S A, 2017. **114**(30): p. E6079-E6088.
49. Krapivinsky, G., et al., *The TRPM7 chanzyme is cleaved to release a chromatin-modifying kinase.* Cell, 2014. **157**(5): p. 1061-72.
50. Kim, Y., et al., *Stress hormone potentiates Zn(2+)-induced neurotoxicity via TRPM7 channel in dopaminergic neuron.* Biochem Biophys Res Commun, 2016. **470**(2): p. 362-7.
51. Ryazanova, L.V., et al., *Characterization of the protein kinase activity of TRPM7/ChaK1, a protein kinase fused to the transient receptor potential ion channel.* J Biol Chem, 2004. **279**(5): p. 3708-16.
52. Dorovkov, M.V. and A.G. Ryazanov, *Phosphorylation of annexin I by TRPM7 channel-kinase.* J Biol Chem, 2004. **279**(49): p. 50643-6.
53. Dorovkov, M.V., A.S. Kostyukova, and A.G. Ryazanov, *Phosphorylation of annexin A1 by TRPM7 kinase: a switch regulating the induction of an alpha-helix.* Biochemistry, 2011. **50**(12): p. 2187-93.
54. Clark, K., et al., *The alpha-kinases TRPM6 and TRPM7, but not eEF-2 kinase, phosphorylate the assembly domain of myosin IIA, IIB and IIC.* FEBS Lett, 2008. **582**(20): p. 2993-7.
55. Clark, K., et al., *TRPM7 regulates myosin IIA filament stability and protein localization by heavy chain phosphorylation.* J Mol Biol, 2008. **378**(4): p. 790-803.
56. Clark, K., et al., *TRPM7, a novel regulator of actomyosin contractility and cell adhesion.* EMBO J, 2006. **25**(2): p. 290-301.
57. Deason-Towne, F., A.L. Perraud, and C. Schmitz, *Identification of Ser/Thr phosphorylation sites in the C2-domain of phospholipase C gamma2 (PLCgamma2) using TRPM7-kinase.* Cell Signal, 2012. **24**(11): p. 2070-5.
58. Perraud, A.L., et al., *The channel-kinase TRPM7 regulates phosphorylation of the translational factor eEF2 via eEF2-k.* Cell Signal, 2011. **23**(3): p. 586-93.
59. Jin, J., et al., *Deletion of Trpm7 disrupts embryonic development and thymopoiesis without altering Mg2+ homeostasis.* Science, 2008. **322**(5902): p. 756-60.
60. Jin, J., et al., *The channel kinase, TRPM7, is required for early embryonic development.* Proceedings of the National Academy of Sciences of the United States of America, 2012. **109**(5): p. E225-33.
61. Sah, R., et al., *Timing of myocardial trpm7 deletion during cardiogenesis variably disrupts adult ventricular function, conduction, and repolarization.* Circulation, 2013. **128**(2): p. 101-14.
62. Sah, R., et al., *Ion channel-kinase TRPM7 is required for maintaining cardiac automaticity.* Proc Natl Acad Sci U S A, 2013. **110**(32): p. E3037-46.
63. Stritt, S., et al., *Defects in TRPM7 channel function deregulate thrombopoiesis through altered cellular Mg(2+) homeostasis and cytoskeletal architecture.* Nat Commun, 2016. **7**: p. 11097.
64. Romagnani, A., et al., *TRPM7 kinase activity is essential for T cell colonization and alloreactivity in the gut.* Nat Commun, 2017. **8**(1): p. 1917.
65. Kaitsuka, T., et al., *Inactivation of TRPM7 kinase activity does not impair its channel function in mice.* Sci Rep, 2014. **4**: p. 5718.
66. Ryazanova, L.V., et al., *Elucidating the role of the TRPM7 alpha-kinase: TRPM7 kinase inactivation leads to magnesium deprivation resistance phenotype in mice.* Sci Rep, 2014. **4**: p. 7599.
67. Krishnamoorthy, M., et al., *The ion channel TRPM7 is required for B cell lymphopoiesis.* Sci Signal, 2018. **11**(533).
68. Wolf, F.I., et al., *Cell physiology of magnesium.* Mol Aspects Med, 2003. **24**(1-3): p. 11-26.

69. Wolf, F.I. and A. Cittadini, *Chemistry and biochemistry of magnesium.* Mol Aspects Med, 2003. **24**(1-3): p. 3-9.
70. Romani, A. and A. Scarpa, *Regulation of cell magnesium.* Arch Biochem Biophys, 1992. **298**(1): p. 1-12.
71. Pontes, M.H., A. Sevostyanova, and E.A. Groisman, *When Too Much ATP Is Bad for Protein Synthesis.* J Mol Biol, 2015. **427**(16): p. 2586-2594.
72. Patel, A., et al., *ATP as a biological hydrotrope.* Science, 2017. **356**(6339): p. 753-756.
73. Rubin, H., *The logic of the Membrane, Magnesium, Mitosis (MMM) model for the regulation of animal cell proliferation.* Arch Biochem Biophys, 2007. **458**(1): p. 16-23.
74. Lowenstein, F.W. and M.F. Stanton, *Serum magnesium levels in the United States, 1971-1974.* J Am Coll Nutr, 1986. **5**(4): p. 399-414.
75. Quamme, G.A., *Renal magnesium handling: new insights in understanding old problems.* Kidney Int, 1997. **52**(5): p. 1180-95.
76. Dai, L.J., et al., *Magnesium transport in the renal distal convoluted tubule.* Physiol Rev, 2001. **81**(1): p. 51-84.
77. Quamme, G.A., *Recent developments in intestinal magnesium absorption.* Curr Opin Gastroenterol, 2008. **24**(2): p. 230-5.
78. Gunzel, D. and A.S. Yu, *Function and regulation of claudins in the thick ascending limb of Henle.* Pflugers Arch, 2009. **458**(1): p. 77-88.
79. Morita, K., et al., *Claudin multigene family encoding four-transmembrane domain protein components of tight junction strands.* Proc Natl Acad Sci U S A, 1999. **96**(2): p. 511-6.
80. Simon, D.B., et al., *Paracellin-1, a renal tight junction protein required for paracellular Mg2+ resorption.* Science, 1999. **285**(5424): p. 103-6.
81. Weber, S., et al., *Primary gene structure and expression studies of rodent paracellin-1.* J Am Soc Nephrol, 2001. **12**(12): p. 2664-72.
82. Konrad, M., et al., *Mutations in the tight-junction gene claudin 19 (CLDN19) are associated with renal magnesium wasting, renal failure, and severe ocular involvement.* Am J Hum Genet, 2006. **79**(5): p. 949-57.
83. Naeem, M., S. Hussain, and N. Akhtar, *Mutation in the tight-junction gene claudin 19 (CLDN19) and familial hypomagnesemia, hypercalciuria, nephrocalcinosis (FHHNC) and severe ocular disease.* Am J Nephrol, 2011. **34**(3): p. 241-8.
84. Voets, T., et al., *TRPM6 forms the Mg2+ influx channel involved in intestinal and renal Mg2+ absorption.* J Biol Chem, 2004. **279**(1): p. 19-25.
85. Lee, C.T., et al., *The role of calbindin-D28k on renal calcium and magnesium handling during treatment with loop and thiazide diuretics.* Am J Physiol Renal Physiol, 2016. **310**(3): p. F230-6.
86. Hoenderop, J.G. and R.J. Bindels, *Epithelial Ca2+ and Mg2+ channels in health and disease.* J Am Soc Nephrol, 2005. **16**(1): p. 15-26.
87. de Baaij, J.H., et al., *Identification of SLC41A3 as a novel player in magnesium homeostasis.* Sci Rep, 2016. **6**: p. 28565.
88. Lameris, A.L., et al., *Segmental transport of Ca(2)(+) and Mg(2)(+) along the gastrointestinal tract.* Am J Physiol Gastrointest Liver Physiol, 2015. **308**(3): p. G206-16.
89. Sahni, J. and A.M. Scharenberg, *The SLC41 family of MgtE-like magnesium transporters.* Mol Aspects Med, 2013. **34**(2-3): p. 620-8.
90. Fagan, T.E. and A. Romani, *alpha(1)-Adrenoceptor-induced Mg2+ extrusion from rat hepatocytes occurs via Na(+)-dependent transport mechanism.* Am J Physiol Gastrointest Liver Physiol, 2001. **280**(6): p. G1145-56.
91. Schweigel, M., et al., *Characterization of the Na+-dependent Mg2+ transport in sheep ruminal epithelial cells.* Am J Physiol Gastrointest Liver Physiol, 2006. **290**(1): p. G56-65.

92. Yoshimura, M., et al., *Effect of the transmembrane gradient of magnesium and sodium on the regulation of cytosolic free magnesium concentration in human platelets.* Clin Sci (Lond), 1995. **89**(3): p. 293-8.
93. Bronner, F., D. Pansu, and W.D. Stein, *An analysis of intestinal calcium transport across the rat intestine.* Am J Physiol, 1986. **250**(5 Pt 1): p. G561-9.
94. Yamazaki, D., et al., *Basolateral Mg2+ extrusion via CNNM4 mediates transcellular Mg2+ transport across epithelia: a mouse model.* PLoS Genet, 2013. **9**(12): p. e1003983.
95. Campbell, A.K., *Intracellular calcium: friend or foe?* Clin Sci (Lond), 1987. **72**(1): p. 1-10.
96. van Os, C.H., *Transcellular calcium transport in intestinal and renal epithelial cells.* Biochim Biophys Acta, 1987. **906**(2): p. 195-222.
97. Peacock, M., *Calcium metabolism in health and disease.* Clin J Am Soc Nephrol, 2010. **5 Suppl 1**: p. S23-30.
98. Bronner, F., *Mechanisms and functional aspects of intestinal calcium absorption.* J Exp Zool A Comp Exp Biol, 2003. **300**(1): p. 47-52.
99. Armbrecht, H.J., M.A. Boltz, and T.L. Hodam, *PTH increases renal 25(OH)D3-1alpha -hydroxylase (CYP1alpha) mRNA but not renal 1,25(OH)2D3 production in adult rats.* Am J Physiol Renal Physiol, 2003. **284**(5): p. F1032-6.
100. Bomsztyk, K., J.P. George, and F.S. Wright, *Effects of luminal fluid anions on calcium transport by proximal tubule.* Am J Physiol, 1984. **246**(5 Pt 2): p. F600-8.
101. Ng, R.C., D. Rouse, and W.N. Suki, *Calcium transport in the rabbit superficial proximal convoluted tubule.* J Clin Invest, 1984. **74**(3): p. 834-42.
102. Hoenderop, J.G., et al., *Renal Ca2+ wasting, hyperabsorption, and reduced bone thickness in mice lacking TRPV5.* J Clin Invest, 2003. **112**(12): p. 1906-14.
103. Lytton, J., et al., *The kidney sodium-calcium exchanger.* Ann N Y Acad Sci, 1996. **779**: p. 58-72.
104. Magyar, C.E., et al., *Plasma membrane Ca2+-ATPase and NCX1 Na+/Ca2+ exchanger expression in distal convoluted tubule cells.* Am J Physiol Renal Physiol, 2002. **283**(1): p. F29-40.
105. White, K.E., F.A. Gesek, and P.A. Friedman, *Structural and functional analysis of Na+/Ca2+ exchange in distal convoluted tubule cells.* Am J Physiol, 1996. **271**(3 Pt 2): p. F560-70.
106. van der Hagen, E.A., et al., *Coordinated regulation of TRPV5-mediated Ca(2)(+) transport in primary distal convolution cultures.* Pflugers Arch, 2014. **466**(11): p. 2077-87.
107. Bianco, S.D., et al., *Marked disturbance of calcium homeostasis in mice with targeted disruption of the Trpv6 calcium channel gene.* J Bone Miner Res, 2007. **22**(2): p. 274-85.
108. Peng, J.B., et al., *Molecular cloning and characterization of a channel-like transporter mediating intestinal calcium absorption.* J Biol Chem, 1999. **274**(32): p. 22739-46.
109. Van Cromphaut, S.J., et al., *Duodenal calcium absorption in vitamin D receptor-knockout mice: functional and molecular aspects.* Proc Natl Acad Sci U S A, 2001. **98**(23): p. 13324-9.
110. Song, Y., et al., *Calcium transporter 1 and epithelial calcium channel messenger ribonucleic acid are differentially regulated by 1,25 dihydroxyvitamin D3 in the intestine and kidney of mice.* Endocrinology, 2003. **144**(9): p. 3885-94.
111. Meyer, M.B., et al., *Characterizing early events associated with the activation of target genes by 1,25-dihydroxyvitamin D3 in mouse kidney and intestine in vivo.* J Biol Chem, 2007. **282**(31): p. 22344-52.
112. Bronner, F. and M. Buckley, *The molecular nature of 1,25-(OH)2-D3-induced calcium-binding protein biosynthesis in the rat.* Adv Exp Med Biol, 1982. **151**: p. 355-60.
113. Benn, B.S., et al., *Active intestinal calcium transport in the absence of transient receptor potential vanilloid type 6 and calbindin-D9k.* Endocrinology, 2008. **149**(6): p. 3196-205.

114. Kutuzova, G.D., et al., *TRPV6 is not required for 1alpha,25-dihydroxyvitamin D3-induced intestinal calcium absorption in vivo.* Proc Natl Acad Sci U S A, 2008. **105**(50): p. 19655-9.
115. Kambe, T., et al., *The Physiological, Biochemical, and Molecular Roles of Zinc Transporters in Zinc Homeostasis and Metabolism.* Physiol Rev, 2015. **95**(3): p. 749-84.
116. Hambidge, M., *Human zinc deficiency.* J Nutr, 2000. **130**(5S Suppl): p. 1344S-9S.
117. Weigand, E. and M. Kirchgessner, *Homeostatic adjustments in zinc digestion to widely varying dietary zinc intake.* Nutr Metab, 1978. **22**(2): p. 101-12.
118. Evans, G.W., E.C. Johnson, and P.E. Johnson, *Zinc absorption in the rat determined by radioisotope dilution.* J Nutr, 1979. **109**(7): p. 1258-64.
119. Methfessel, A.H. and H. Spencer, *Zinc metabolism in the rat. I. Intestinal absorption of zinc.* J Appl Physiol, 1973. **34**(1): p. 58-62.
120. Davies, N.T., *Studies on the absorption of zinc by rat intestine.* Br J Nutr, 1980. **43**(1): p. 189-203.
121. Ghishan, F.K. and G. Sobo, *Intestinal maturation: in vivo zinc transport.* Pediatr Res, 1983. **17**(2): p. 148-51.
122. Wang, K., et al., *A novel member of a zinc transporter family is defective in acrodermatitis enteropathica.* Am J Hum Genet, 2002. **71**(1): p. 66-73.
123. Dufner-Beattie, J., et al., *The adaptive response to dietary zinc in mice involves the differential cellular localization and zinc regulation of the zinc transporters ZIP4 and ZIP5.* J Biol Chem, 2004. **279**(47): p. 49082-90.
124. Davis, S.R. and R.J. Cousins, *Metallothionein expression in animals: a physiological perspective on function.* J Nutr, 2000. **130**(5): p. 1085-8.
125. Coyle, P., et al., *Metallothionein: the multipurpose protein.* Cell Mol Life Sci, 2002. **59**(4): p. 627-47.
126. Palmiter, R.D. and S.D. Findley, *Cloning and functional characterization of a mammalian zinc transporter that confers resistance to zinc.* EMBO J, 1995. **14**(4): p. 639-49.
127. Palmiter, R.D., *Protection against zinc toxicity by metallothionein and zinc transporter 1.* Proc Natl Acad Sci U S A, 2004. **101**(14): p. 4918-23.
128. Atherton, D.J., et al., *A defect in zinc uptake by jejunal biopsies in acrodermatitis enteropathica.* Clin Sci (Lond), 1979. **56**(5): p. 505-7.
129. Kury, S., et al., *Identification of SLC39A4, a gene involved in acrodermatitis enteropathica.* Nat Genet, 2002. **31**(3): p. 239-40.
130. Neldner, K.H. and K.M. Hambidge, *Zinc therapy of acrodermatitis enteropathica.* N Engl J Med, 1975. **292**(17): p. 879-82.
131. Geiser, J., et al., *A mouse model of acrodermatitis enteropathica: loss of intestine zinc transporter ZIP4 (Slc39a4) disrupts the stem cell niche and intestine integrity.* PLoS Genet, 2012. **8**(6): p. e1002766.
132. Arnaud, J. and A. Favier, *Determination of ultrafiltrable zinc in human milk by electrothermal atomic absorption spectrometry.* Analyst, 1992. **117**(10): p. 1593-8.
133. Eide, D.J., *Zinc transporters and the cellular trafficking of zinc.* Biochim Biophys Acta, 2006. **1763**(7): p. 711-22.
134. Madison, B.B., et al., *Cis elements of the villin gene control expression in restricted domains of the vertical (crypt) and horizontal (duodenum, cecum) axes of the intestine.* J Biol Chem, 2002. **277**(36): p. 33275-83.
135. Shao, X., S. Somlo, and P. Igarashi, *Epithelial-specific Cre/lox recombination in the developing kidney and genitourinary tract.* J Am Soc Nephrol, 2002. **13**(7): p. 1837-46.
136. Rodushkin, I. and F. Odman, *Application of inductively coupled plasma sector field mass spectrometry for elemental analysis of urine.* J Trace Elem Med Biol, 2001. **14**(4): p. 241-7.
137. Rodushkin, I., et al., *Determination of low-abundance elements at ultra-trace levels in urine and serum by inductively coupled plasma-sector field mass spectrometry.* Anal Bioanal

Chem, 2004. **380**(2): p. 247-57.
138. Kotecki, M., P.S. Reddy, and B.H. Cochran, *Isolation and characterization of a near-haploid human cell line.* Exp Cell Res, 1999. **252**(2): p. 273-80.
139. Wang, T., et al., *Identification and characterization of essential genes in the human genome.* Science, 2015. **350**(6264): p. 1096-101.
140. Bronner, F., *Extracellular and intracellular regulation of calcium homeostasis.* ScientificWorldJournal, 2001. **1**: p. 919-25.
141. Reilly, R.F. and D.H. Ellison, *Mammalian distal tubule: physiology, pathophysiology, and molecular anatomy.* Physiol Rev, 2000. **80**(1): p. 277-313.
142. Park, J., et al., *Single-cell transcriptomics of the mouse kidney reveals potential cellular targets of kidney disease.* Science, 2018.
143. Ogata, K., et al., *The crucial role of the TRPM7 kinase domain in the early stage of amelogenesis.* Sci Rep, 2017. **7**(1): p. 18099.
144. Efrati, E., et al., *Transcriptional regulation of the claudin-16 gene by Mg2+ availability.* Cell Physiol Biochem, 2010. **25**(6): p. 705-14.
145. Groenestege, W.M., et al., *The epithelial Mg2+ channel transient receptor potential melastatin 6 is regulated by dietary Mg2+ content and estrogens.* J Am Soc Nephrol, 2006. **17**(4): p. 1035-43.
146. Ko, S.H., et al., *Dietary calcium and 1,25-dihydroxyvitamin D3 regulate transcription of calcium transporter genes in calbindin-D9k knockout mice.* J Reprod Dev, 2009. **55**(2): p. 137-42.
147. Liuzzi, J.P., R.K. Blanchard, and R.J. Cousins, *Differential regulation of zinc transporter 1, 2, and 4 mRNA expression by dietary zinc in rats.* J Nutr, 2001. **131**(1): p. 46-52.
148. Jin, J., et al., *The channel kinase, TRPM7, is required for early embryonic development.* Proc Natl Acad Sci U S A, 2012. **109**(5): p. E225-33.
149. Farin, H.F., et al., *Paneth cell extrusion and release of antimicrobial products is directly controlled by immune cell-derived IFN-gamma.* J Exp Med, 2014. **211**(7): p. 1393-405.
150. Koo, S.I., et al., *Effect of marginal zinc deficiency on the morphological characteristics of intestinal nascent chylomicrons and distribution of soluble apoproteins of lymph chylomicrons.* Am J Clin Nutr, 1985. **42**(4): p. 671-80.
151. Koo, S.I. and D.E. Turk, *Effect of zinc deficiency on intestinal transport triglyceride in the rat.* J Nutr, 1977. **107**(5): p. 909-19.
152. Khanal, R.C. and I. Nemere, *Regulation of intestinal calcium transport.* Annu Rev Nutr, 2008. **28**: p. 179-96.
153. Fleet, J.C. and R.D. Schoch, *Molecular mechanisms for regulation of intestinal calcium absorption by vitamin D and other factors.* Crit Rev Clin Lab Sci, 2010. **47**(4): p. 181-95.
154. Ertek, S., et al., *Relationship between serum zinc levels, thyroid hormones and thyroid volume following successful iodine supplementation.* Hormones (Athens), 2010. **9**(3): p. 263-8.
155. Erway, L.C. and A. Grider, Jr., *Zinc metabolism in lethal-milk mice. Otolith, lactation, and aging effects.* J Hered, 1984. **75**(6): p. 480-4.
156. Sporn, M.B. and K.T. Liby, *NRF2 and cancer: the good, the bad and the importance of context.* Nat Rev Cancer, 2012. **12**(8): p. 564-71.
157. Meister, A., *Glutathione deficiency produced by inhibition of its synthesis, and its reversal; applications in research and therapy.* Pharmacol Ther, 1991. **51**(2): p. 155-94.
158. Taguchi, K., H. Motohashi, and M. Yamamoto, *Molecular mechanisms of the Keap1-Nrf2 pathway in stress response and cancer evolution.* Genes Cells, 2011. **16**(2): p. 123-40.
159. Meister, A., *Selective modification of glutathione metabolism.* Science, 1983. **220**(4596): p. 472-7.
160. McGrath-Morrow, S., et al., *Nrf2 increases survival and attenuates alveolar growth inhibition*

in neonatal mice exposed to hyperoxia. Am J Physiol Lung Cell Mol Physiol, 2009. **296**(4): p. L565-73.
161. Harvey, C.J., et al., *Nrf2-regulated glutathione recycling independent of biosynthesis is critical for cell survival during oxidative stress.* Free Radic Biol Med, 2009. **46**(4): p. 443-53.
162. Thimmulappa, R.K., et al., *Identification of Nrf2-regulated genes induced by the chemopreventive agent sulforaphane by oligonucleotide microarray.* Cancer Res, 2002. **62**(18): p. 5196-203.
163. Adachi, T., et al., *Nrf2-dependent and -independent induction of ABC transporters ABCC1, ABCC2, and ABCG2 in HepG2 cells under oxidative stress.* J Exp Ther Oncol, 2007. **6**(4): p. 335-48.
164. Wessels, I., M. Maywald, and L. Rink, *Zinc as a Gatekeeper of Immune Function.* Nutrients, 2017. **9**(12).
165. Van Wouwe, J.P., *Clinical and laboratory diagnosis of acrodermatitis enteropathica.* Eur J Pediatr, 1989. **149**(1): p. 2-8.
166. Julius, R., et al., *Acrodermatitis enteropathica with immune deficiency.* J Pediatr, 1973. **83**(6): p. 1007-11.
167. Rodin, A.E. and A.S. Goldman, *Autopsy findings in acrodermatitis enteropathica.* Am J Clin Pathol, 1969. **51**(3): p. 315-22.
168. Mederos y Schnitzler, M., et al., *Gq-coupled receptors as mechanosensors mediating myogenic vasoconstriction.* EMBO J, 2008. **27**(23): p. 3092-103.
169. Ferioli, S., et al., *TRPM6 and TRPM7 differentially contribute to the relief of heteromeric TRPM6/7 channels from inhibition by cytosolic Mg2+ and Mg.ATP.* Sci Rep, 2017. **7**(1): p. 8806.
170. Kozak, J.A., H.H. Kerschbaum, and M.D. Cahalan, *Distinct properties of CRAC and MIC channels in RBL cells.* J Gen Physiol, 2002. **120**(2): p. 221-35.
171. Li, M., et al., *Molecular determinants of Mg2+ and Ca2+ permeability and pH sensitivity in TRPM6 and TRPM7.* J Biol Chem, 2007. **282**(35): p. 25817-30.
172. Marreiro, D.D., et al., *Zinc and Oxidative Stress: Current Mechanisms.* Antioxidants (Basel), 2017. **6**(2).
173. Aarts, M., et al., *A key role for TRPM7 channels in anoxic neuronal death.* Cell, 2003. **115**(7): p. 863-77.
174. Gorrini, C., I.S. Harris, and T.W. Mak, *Modulation of oxidative stress as an anticancer strategy.* Nat Rev Drug Discov, 2013. **12**(12): p. 931-47.
175. Huang, L. and J. Gitschier, *A novel gene involved in zinc transport is deficient in the lethal milk mouse.* Nat Genet, 1997. **17**(3): p. 292-7.
176. Piletz, J.E. and R.E. Ganschow, *Zinc deficiency in murine milk underlies expression of the lethal milk (lm) mutation.* Science, 1978. **199**(4325): p. 181-3.
177. Murgia, C., et al., *The Znt4 mutation inlethal milk mice affects intestinal zinc homeostasis through the expression of other Zn transporters.* Genes Nutr, 2006. **1**(1): p. 61-70.
178. Wang, F., et al., *The mammalian Zip5 protein is a zinc transporter that localizes to the basolateral surface of polarized cells.* J Biol Chem, 2004. **279**(49): p. 51433-41.
179. Geiser, J., R.C. De Lisle, and G.K. Andrews, *The zinc transporter Zip5 (Slc39a5) regulates intestinal zinc excretion and protects the pancreas against zinc toxicity.* PLoS One, 2013. **8**(11): p. e82149.
180. Ruttkay-Nedecky, B., et al., *The role of metallothionein in oxidative stress.* Int J Mol Sci, 2013. **14**(3): p. 6044-66.
181. Dorup, I., et al., *Role of insulin-like growth factor-1 and growth hormone in growth inhibition induced by magnesium and zinc deficiencies.* Br J Nutr, 1991. **66**(3): p. 505-21.
182. Zhang, Z., et al., *The TRPM6 kinase domain determines the Mg.ATP sensitivity of TRPM7/M6 heteromeric ion channels.* J Biol Chem, 2014. **289**(8): p. 5217-27.

I Abbreviations

Abcc1	ATP-binding cassette C1
Abcc2	ATP-binding cassette C2
ATP	adenosine triphosphate
bp	base pair
BSA	bovine serum albumin
Ca	calcium
Cas	*CRISPR-associated*
CRISPR	clustered regularly interspaced short palindromic repeats
Cyp27b1	cytochrome p450 27b1
d	day
Dclk1	doublecortin like kinase 1
DCT	distal convoluted tubule
DIG	digoxigenin
DNA	deoxyribonucleic acid
dNTP	deoxynucleoside triphosphate
dpm	disintegrations per minute
DTT	dithiothreitol
ELISA	enzyme-linked immunosorbent assay
EtOH	ethanol
FBS	fetal bovine serum
fl	floxed
g	gram
Gclc	glutamate cysteine ligase catalytic subunit
Gpx2	glutathione peroxidase 2
Gsr	glutathione reductase
Gss	glutathione synthetase
Gsta1	glutathione S-transferase alpha 1
Gsta2	glutathione S-transferase alpha 2
Gsta3	glutathione S-transferase alpha 3
Gstp1	glutathione S-transferase P1

h	hour
H&E	hematoxylin and eosin
HAP1	human haploid leukemia
Hprt	hypoxanthine-guanine phosphoribosyl transferase
ICP-MS	inductively coupled plasma mass spectrometry
IGF1	insulin-like growth factor 1
IL-6	interleukin 6
IMDM	Iscove's Modified Dulbecco's Medium
K	thymine
ki	knock in
KO	knock out
l	liter
Lgr5	leucine-rich repeat-containing G-protein coupled receptor 5
Lyz1	lysozyme 1
m	milli
M	molar
Mg	magnesium
Mgst2	microsomal glutathione S-transferase 2
min	minute
MT1	metallothionein 1
Muc2	mucin 2
P	phosphorus
P1	postnatal day 1
P3	postnatal day 3
P5	postnatal day 5
P21	postnatal day 21
P23	postnatal day 23
P33	postnatal day 33
P37	postnatal day 37
PBS	phosphate-buffered saline
PCR	polymerase chain reaction
PFA	paraformaldehyde
PTH	parathyroid hormone
qRT-PCR	quantitative real-time PCR

R	cytosine
RNA	ribonucleic acid
rpm	revolutions per minute
s	second
S	sulfur
SEM	standard error of the mean
Slc41a1	solute carrier family 41 member 1
Slc41a2	solute carrier family 41 member 2
T4	thyroxine
tRNA	transfer RNA
Trpm6	transient receptor potential cation channel, subfamily M, member 6
Trpm7	transient receptor potential cation channel, subfamily M, member 7
Trpv5	transient receptor potential cation channel, subfamily V, member 5
Trpv6	transient receptor potential cation channel, subfamily V, member 6
U	unit
V	volume
wt	wildtype
Ywhaz	tyrosine 3/5 monooxygenase
Zip4	solute carrier family 39 member 4
Zip5	solute carrier family 39 member 5
Zn	zinc
ZnT1	solute carrier family 30 member 1
ZnT2	solute carrier family 30 member 2
ZnT4	solute carrier family 30 member 4

II Index of figures

III Index of tables

IV Publications

Parts of the results of this thesis are published in the following scientific peer-reviewed journal:

1. TRPM7 is the central gatekeeper of intestinal mineral absorption essential for postnatal survival

Mittermeier L, Demirkhanyan L, Stadlbauer B, Breit A, Recordati C, Matsushita M, Braun A, Simmons D, Zakharian E, Gudermann T, Chubanov V.

Proc. Natl. Acad. Sci. USA, 2019 Feb 15.

Results of other projects I worked on are published in the following peer-reviewed journals:

2. Epithelial magnesium transport by TRPM6 is essential for prenatal development and adult survival

Chubanov V, Ferioli S, Wisnowsky A, Simmons DG, Leitzinger C, Einer C, Jonas W, Shymkiv Y, Bartsch H, Braun A, Akdogan B, Mittermeier L, Sytik L, Torben F, Jurinovic V, van der Vorst EP, Weber C, Yildirim ÖA, Sotlar K, Schürmann A, Zierler S, Zischka H, Ryazanov AG, Gudermann T.

eLife, 2016;5:e20914 doi: 10.7554/eLife.20914.

3. TRPM7 is a molecular substrate of ATP-evoked P2X7-like currents in tumor cells

Nörenberg W, Plötz T, Sobottka H, Chubanov V, Mittermeier L, Kalwa H, Aigner A, Schaefer M.

Journal of General Physiology, 2016 Jun; 147(6):467-483.

4. Defects in TRPM7 channel function deregulate thrombopoiesis through altered cellular Mg(2+) homeostasis and cytoskeletal architecture

Stritt S, Nurden P, Favier R, Favier M, Ferioli S, Gotru SK, van Eeuwijk JM, Schulze H, Nurden AT, Lambert MP, Turro E, Burger-Stritt S, Matsushita M, Mittermeier L, Ballerini P, Zierler S, Laffan MA, Chubanov V, Gudermann T, Nieswandt B, Braun A.

Nature Communications, 2016 Mar 29;7:11097.

The following reviews are published:

5. TRPM7 reflected in Cryo-EMirror

Chubanov V, Mittermeier L, Gudermann T.

Cell Calcium, 2018 Dec;76:129-131. doi: 10.1016/j.ceca.2018.11.004.

6. Role of kinase-coupled TRP channels in mineral homeostasis

Chubanov V, Mittermeier L, Gudermann T.

Pharmacol Ther. 2018 Apr; 184:159-176. doi: 10.1016/j.pharmthera.2017.11.003.

Posters:

Parts of the results were presented at poster sessions at the following congresses:

1. Assessment of the TRPM7 function in adult mice

Ion Channel & Immunity Symposium, New York City, USA; December 2018

2. Role of kinase-coupled TRPM7 channel in whole body mineral homeostasis

Regulation of cell functions by transient receptor potential channels, Herrsching, Germany; September 2016

V Acknowledgements

First of all, I would like to thank Dr. Vladimir Chubanov for giving me the opportunity to perform my PhD thesis in his laboratory. Many thanks for being a great scientific mentor, for your enthusiasm and for all the inspiring discussions.

I am very thankful to Prof. Dr. Thomas Gudermann for being my doctor father and for his extensive support and scientific advice.

I also want to thank PD Dr. Dietmar Martin for being my external representative at the faculty of chemistry and pharmacy. Additionally, I am thankful to Prof. Dr. Alexander Dietrich, Prof. Dr. Julian Stingele, Prof. Dr. Klaus Förstemann and Prof. Dr. Nina Henriette Uhlenhaut for their willingness to be a member of my examination board.

I would like to thank Dr. Andreas Breit for his extensive assistance with ^{65}Zn experiments and PD Dr. Anne Hilgendorff for her support with animal experiments.

Moreover, I also want to thank our cooperation partners Dr. David Simmons for helping us with *in situ* hybridization, Dr. Camilla Recordati for her support and consultation regarding histology experiments and Dr. Ilia Rodushkin for his support in ICP-MS analysis.

Furthermore, I am thankful to the team of our animal facility, especially Petra Eigner and Clarinda Hofer.

Particularly, I would like to thank all the previous and present members of my group: Banu Akdogan, Silvia Ferioli, Eva Schmidt and Miyuki Egawa for the friendly atmosphere in the lab and for their support. Especially I am thankful to Joanna Zaißerer for her general assistance and help with preparation of *in vitro* experiments, Anna Erbacher for her support with immunohistology and Benjamin Stadlbauer for his help with *in situ* hybridization.

I am also very grateful to my parents and my sister for their everlasting support and encouragement throughout the whole time of my life. Thank you for always being there for me!

Last but not least, I would like to thank my wife Constanze for proofreading this thesis and the scientific advice. I am so grateful for your endless support and your love. I am deeply thankful for having you in my life.